Ultrasound-Driven Fabrication of Nanosized High-Entropy Materials for Heterogeneous Catalysis

A Dissertation Presented for the

Doctor of Philosophy

Degree

The University of Tennessee, Knoxville

Francis U. Okejiri

December 2021

Copyright © 2021 by Francis Okejiri.

All rights reserved.

DEDICATION

To the loving memory of my late parents; continue to rest in peace.

ACKNOWLEDGEMENTS

The completion of an undertaking of this magnitude would not have been possible without the help and support of many individuals who have contributed immensely toward its success.

First and foremost, I would like to thank my research advisor, Dr. Sheng Dai for his mentorship and guidance over the past four and half years; it is through him and the support system that he created that I have become the chemist that I am today.

I also would like to thank my committee members, Dr. Bhavya Sharma, Dr. Ampofo Darko, and Dr. Bin Hu for their commitment of time and energy; for reviewing my dissertation, and for providing valuable suggestions and feedback.

I express my heartfelt thanks and gratitude to the following past and present members of Dr. Dai research group: Dr. Zhenzhen Yang, Dr. Zihao Zhang, Dr. Hao Chen, Dr. Tao Wang, Dr. Chi-Linh Do-Thanh, Dr. Shize Yang, and Dr. Jixing Liu for helpful discussion of research work, making life in the lab easier and interesting, and for their prompt notification of the location of free foods.

And to all my colleagues, family, and friends whose names are not mentioned here and have rendered help in one way or the other, I express my sincere gratitude.

ABSTRACT

High-entropy materials (HEMs) have emerged as a new class of multi-principal-element materials with great technological prospects. As a unique class of concentrated solid-solution materials, HEMs, formed on the premise of incorporating five or more principal elements into a single crystalline phase, provide an excellent opportunity to access superior catalytic materials ‘hiding’ in the unexplored central regions of a multicomponent phase space of higher orders.

However, the fabrication of HEMs is energy-intensive, typically requiring extreme temperatures and/or pressures under which agglomeration of particles occurs with a commensurate decrease in surface area. For most catalytic applications, non-agglomerated particles with high surface areas are preferred. Accessing nanostructured HEMs with an increased surface area has motivated efforts to explore unconventional synthesis strategies.

On the other hand, ultrasound can be used to drive high-energy chemical reactions via the physical process of acoustic cavitation that provides a unique high-energy environment at such magnitude and time scale that is unattainable with conventional energy sources. Our overarching goal is to exploit this unique high-energy environment toward the synthesis of nanostructured HEM as an emerging new class of catalytic materials. Taking advantage of the acoustic cavitation phenomenon, nanostructured particles of various subclasses of HEMs, including high-entropy fluorite oxides (HEFOs), high-entropy perovskite oxides (HEPOs), and high-entropy alloys (HEAs) were fabricated at seemingly room temperature conditions in the present study. Several characterization techniques

were used to understand the crystalline structure, chemical composition, surface chemistry, and textural features of the fabricated nanocatalysts. Their catalytic performances were assessed towards carbon monoxide (CO) oxidation and/or selective phenol hydrogenation. Such a technologically feasible, facile, and scalable synthetic strategy holds great promise towards the synthesis of nanocrystalline materials for different applications.

TABLE OF CONTENTS

LIST OF TABLES

LIST OF FIGURES

CHAPTER 1: GENERAL INFORMATION AND INTRODUCTION TO CATALYSIS

1.1 Importance of catalysis

Catalysis is fundamental to many chemical processes that are essential to daily living and a sustainable future. As one of the oldest application fields of modern civilization, catalysis is at the heart of many successfully operated chemical processes with far-reaching applications in the energy, chemical, pharmaceutical, electronics, and automobile industries.[1,2] Catalysis is involved at some stage in the processing of approximately 90% of all manufactured goods,[3] and accounts for more than 25% of the world's gross domestic products.[2]

One of the most useful applications of catalysis in modern civilization is the upgrading of crude petroleum feedstock via catalytic cracking to lower molecular weight hydrocarbons that are ultimately used for a large portion of the world's supply of fuels.[4] Catalysis is also applied in areas of environmental protection. A classic example is the design and development of catalytic converters – a critical component of the exhaust system of modern automobiles that converts toxic pollutants such as nitrogen oxides (NO_x), carbon monoxide (CO), and hydrocarbons (C_xH_y) emitted from the internal combustion engine into less-toxic pollutants like nitrogen (N_2), carbon dioxide (CO_2), and water (H_2O).[5] Modern catalytic converters are made of precious metals finely dispersed onto high-surface support specifically formulated into a tubular, honeycomb structure to enhance the

exposure of the catalytically active metals to the target gaseous species.[5] Immobilization of catalytically active components onto a high surface area support is an important concept in heterogeneous catalysis and will be discussed further in more detail.

As the demands for environmentally friendly, sustainable, and carbon-neutral processes continue to rise across chemical industries, catalysis will, without doubt, be one of the most highly sought-after technologies to navigate these industrial and socio-economic constraints. With the increasing world population and depleting earth's resources, the demands towards sustainable processes of low energy input, improved atom efficiency, increased selectivity, pollution prevention, and simplified purification procedures could not be more pressing. Catalysis-related research is regarded as a multidisciplinary task that requires the concerted efforts of chemists, materials scientists, physicists, and engineers and has remained at the very central position in contemporary science, constituting both fundamental and conceptual challenges. Indeed, recent catalytic science is characterized by both technical and conceptual challenges, that is, identification of the catalytic active sites, and improvement of efficiency of the existing catalysts, which, without a doubt, is the core area in which catalysis currently operates.

1.2 Introduction to catalysis

The term 'catalysis' was first introduced by Berzelius in the year 1836 to rationalize a wide range of observed phenomena by many researchers.[6] Berzelius

observed that a number of reactions only occurred when certain substances, known today as catalysts were present to initiate the process.

A catalyst is defined as a substance that speeds up the rate of a chemical reaction without being consumed in the process.[7] The increase in reaction rate is a result of a decrease in the activation energy of the reaction. A catalyst decreases activation energy by providing stability to reactive intermediates that are otherwise too unstable or energetic to provide alternative mechanistic pathways for reactant transformation to the desired products.[7] A catalyst, therefore, is a substance that provides alternative routes to the final products with the least activation energy, effectively lowering the required energy input to complete the desired reaction or increasing the reaction rate at a given energy input. A schematic representation of a typical activation energy plot for catalyzed versus non-catalyzed reactions is depicted in figure 1.1.

Catalysis can be divided into two broad categories – homogeneous and heterogeneous – based on the phase of reactants relative to the catalysts.[7]

Homogeneous catalysis involves a one-phase system, in which the catalysts and reactants exist in the same phase as one another, typically in the liquid phase. Traditional homogeneous catalysts are very active and highly selective at relatively mild reaction conditions. Homogeneous catalysts are readily soluble in reaction mixtures which makes them amenable to analysis by a host of solution-based spectroscopic techniques that can provide direct information on the catalysts for precise and accurate characterization of the active site.

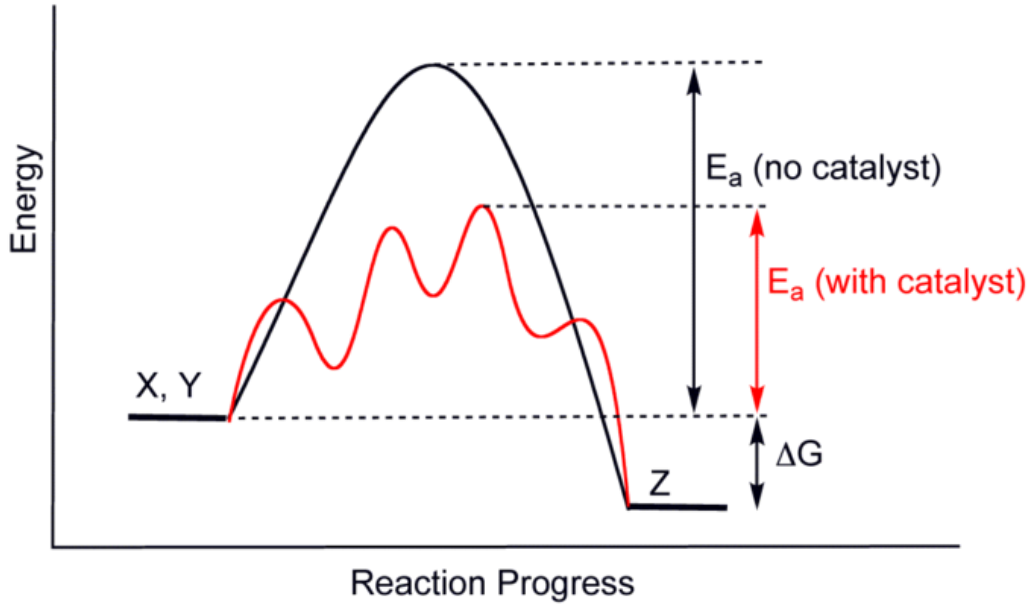

Figure 1.1. Reaction coordinate diagram of a generic exothermic reaction of a catalyzed (red) versus non-catalyzed (black) reaction. Figure reprinted from reference eight.[8]

Heterogeneous catalysis, on the other hand, involves a system in which the catalysts are of different phases from the reactants: usually, the catalyst is in a solid state and interacts with reactants in gaseous or liquid phases. Due to their poor solubility, acquiring structural information is a formidable task that often requires multiple characterization techniques. Heterogeneous catalysts account for approximately 90% of all catalysts used in the industries.[9] Heterogeneous catalysts are preferred over their homogeneous counterparts in industrial catalytic applications because of their robustness, lower operational cost, and ease of recovery from products which facilitates the streamlining of the chemical processes.[7]

The surface structures of heterogeneous catalysts consist of various interacting components which make it difficult to elucidate the complete reaction mechanisms. With the exception of a few simple and extensively studied reactions, the complete reaction mechanisms of most heterogeneous catalysts are usually not well-understood. Nevertheless, the overall analysis of the actions of heterogeneous catalysts on reactant molecules can be summarized in three mechanistic steps as shown in figure 1.2: (a) the adsorption of the reactant molecules on the catalyst's surface (b) reaction at the catalytic active site (c) desorption of the product from the catalysts surface.

The catalytically active components – typically metal or metal oxide nanoparticles – of heterogeneous catalysts can be dispersed onto large-surface-area supports such as silica, alumina, titania, or carbon for physical form, texture,

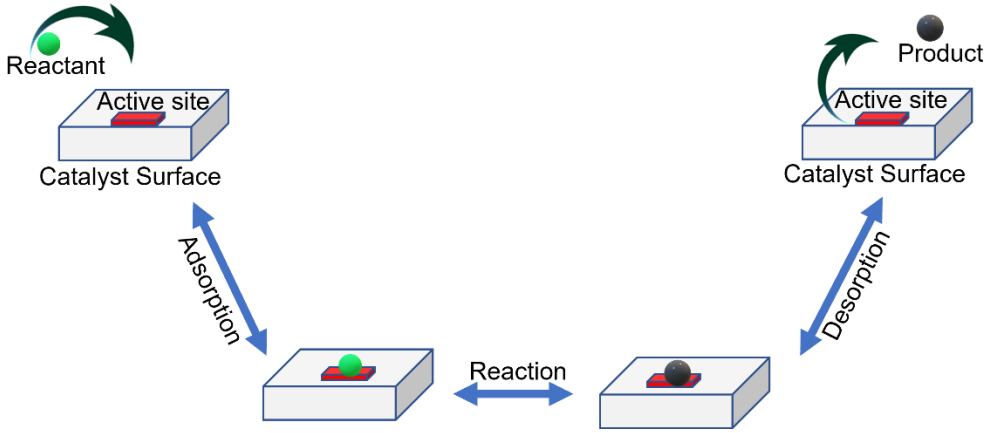

Figure 1.2. Schematic illustration of the chemical reactions that occur at the surface of a heterogeneous catalyst.

and mechanical resistance. This is especially important when costly noble metals such as palladium, gold, ruthenium, or platinum are employed as the active components. The support system may be inactive or possess the ability to interact with the catalytically active components, altering its surface structure and influencing the catalytic performance. In some cases, the support may have the ability to adsorb the reactant molecules and contribute to the reaction process.[10] Also, the active components may be used as highly active free particles in the bulk form without any support (Unsupported catalysts). At catalytic reaction conditions, unsupported free particles tend to aggregate into larger particles (because of their intrinsic high surface energy), diminishing the active surface area with a commensurate decrease in reactivity or even a complete loss of catalytic activity.

Meanwhile, a unique class of multielement materials has shown great prospects in heterogeneous catalysis. Section 1.3 introduces this emerging new class of concentrated solid-solution materials.

1.3 High-entropy materials (HEMs)

Since time immemorial, the materials research community has constantly sought ways to develop materials with improved and tailorable properties to meet contemporary technology needs and sustain application relevance for a considerable timeframe.[11,12] A common methodology in which materials are experimentally developed relies on the modification of already well-understood systems to add or improve upon any desired properties, as is the case with alloying.[11,12] Generally, the basic alloying strategy involves introducing relatively

small concentrations of secondary elements to the base element. Such one principal-element-based approach, however, significantly limits the total number of possible element combinations and therefore, new alloys that can be formed.[12,13] Thus, an alternative strategy is needed if the compositional space of alloys is to be extended to the central regions of a multicomponent phase diagram of higher-order since the conventional alloying strategy tend to concentrate only around the corners (figure 1.3) where the total number of potential element combinations is limited.[12,13]

At the turn of the new millennium, an alternative approach to material design was proposed that sought to investigate this unexplored central region of higher-order. This new alloying strategy, which is in sharp contrast to the conventional method, was based on the premise of integrating five or more principal elements at a near-equimolar concentration into a single-phase crystal structure.[13, 14] The ensuing burgeoning interest in this research area is mainly because of the fact that a significant number of the near-equiatomic multi-component component alloys appear to have formed a remarkably fewer number of phases or even single-phase alloys compared to what is predicted by Gibb's phase rule. This behavior is contrary to what intuition would lead one to believe since the conventional view dictates that the probability of the formation of new compounds increases with an increasing number of elements in concentrated alloys. But Yeh et al. argued that the presence of five or more elements at near-equiatomic concentrations increases the configurational entropy of mixing by an amount sufficient to overcome the enthalpic contribution to the total free energy, favoring the formation of solid

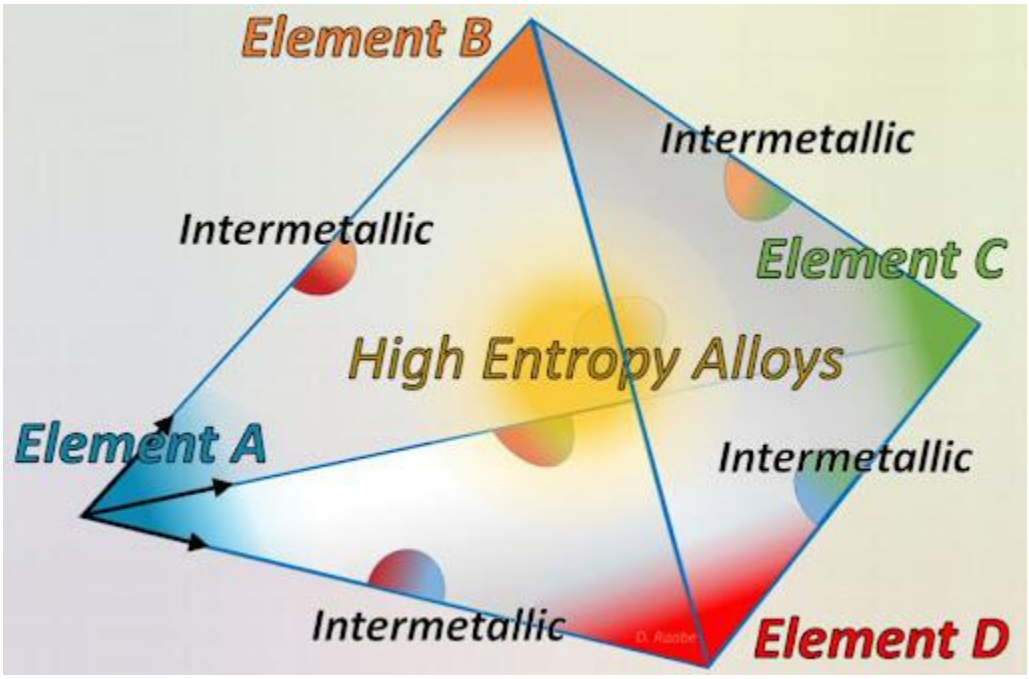

Figure 1.3 Schematic phase diagram showing regions of well-known materials near the corners and poorly-known or unknown materials in the center region. Figure reprinted from reference fifteen.[15]

solutions, from which they coined the catchy phrase - High-entropy alloys (HEAs).[14,16] Other alternative names, including multi-principal-element alloys, compositionally complex alloys, multi-component alloys, etc., have been used to describe this unique class of materials containing principal elements at relatively high amounts (5–35 at.%).[12,17-19] However, considering its popularity in the literature, the name high-entropy alloys has endeared in the hearts of many despite entropy not being the only factor responsible for their structure and properties.

Over the past few years, the 'high-entropy concept has extended beyond metal alloys to include high-entropy oxides,[11] high-entropy nitrides,[20] high-entropy borides,[21] high-entropy silicides,[22] etc., referred collectively to as high-entropy materials (HEMs).[22-24]

HEMs with their great tunability and inherent surface complexity offer an excellent opportunity to access superior catalysts and resolve issues that are hitherto considered difficult in traditional, simple systems.[23] The presence of multiple element species in the same crystalline lattice significantly widens the tunning range of the catalytic active sites. The interaction between the various incorporated elements brings about unprecedented material properties and allows a unique property tailoring. Some unique yet superior catalytic traits have been reported, owing to the strong interactions between the constituent elements.[25,26] HEMs are generally located at the central position of multiphase space (figure 1.3) which is usually the least explored region of material composition and is therefore expected to have unpredicted characteristics.

Thermodynamically speaking, the Gibbs free energy equation below can be used to estimate the phase stability of a multi-component system:[14]

$$\Delta G_{mix} = \Delta H_{mix} - T\Delta S_{mix} \qquad eqn\ (1.1)$$

where ΔG_{mix} is the change in total Gibbs free energy, T is the thermodynamic temperature, and ΔH_{mix}, and ΔS_{mix} represent changes in enthalpy and mixing entropy respectively. It can be deduced from equation 1.1 that ΔG_{mix} depends on the relative values of $-T\Delta S_{mix}$ and ΔH_{mix}. It follows that a multicomponent system of $\Delta G_{mix} < 0$ favors the formation of a single-phase state with a random distribution of the constituent. A positive ΔG_{mix} on the other hand suggests thermodynamically-driven phase segregation.

The change in entropy of mixing in an ideal solid solution can be written as:

$$\Delta S_{mix} = -R\Sigma x_i ln x_i \qquad eqn\ (1.2)$$

where $-R$ is the ideal gas constant and x_i represents the mole fraction of *i*th component. Based on $eqn\ (1.2)$, ΔS_{mix} is at its maximum value at equal molar fractions of the constituent elements. This value can be calculated for an equimolar ternary, quaternary and, quinary alloys to be 1.10*R*, 1.39*R,* and 1.61*R* respectively. Contrastingly, the ΔH_{mix} value differs in ordered intermetallic and phase-segregated systems which is why the entropic contribution to total free energy ($T\Delta S_{mix}$) subdues the enthalpic contribution (ΔH_{mix}) at different critical temperatures.[23]

$Equations\ (1.1)\ and\ (1.2)$ are fundamental to understanding the formation and properties of HEMs as they qualitatively describe the enthalpy-entropy

relationship in multicomponent systems at various temperatures. The two major deductions that can be drawn from these are as follow: 1) At sufficiently high temperatures, configurational entropy emerges as the main stabilizing term in multicomponent systems (2) increase in the number of constituent elements at a near-equimolar ratio significantly boosts the entropic contributions, resulting in a decrease in the overall free energy of the system.[23]

1.4 Preparation of heterogeneous catalysts

Heterogeneous catalysts can be prepared by means of several synthetic methods, including precipitation, co-precipitation, sol-gel, incipient wetness impregnation, hydrothermal synthesis, templating, deposition-precipitation, etc. The choice of the preparation is dependent on several factors such as the desired physicochemical properties of the final composition, availability of the base materials, and the intended application of the final catalysts.[27-29]

1.5 Precipitation method

Precipitation is one of the simplest and most commonly used synthetic methods to fabricate bulk catalysts and support materials such as TiO_2 Al_2O_3, ZrO_2, SiO_2, etc.[28,29] It involves the combination of two solutions; one consisting of the precipitating agent and the other containing the solubilized catalysts precursor, usually a high-valent metal cation. Several key processes occur during precipitation which includes mixing/supersaturation of the solubilized metal precursors, spontaneous creation of the solid seed crystal in the mother liquor (nucleation), growth of the nuclei to form the primary product, and aggregation of

the primary particles.[29] Precipitation is significantly affected by the initial mixing of the components in the solution. Homogenized products result from sufficient mixing and are especially important in coprecipitation. Nucleation and aggregation processes are primarily affected by the rate of stirring.[29] The size of the aggregate can be tuned by altering the manner of mixing and stirring rate. The stirring rate has no significant influence on the growth rate of the nuclei.[29] Nucleation can be homogeneous or heterogeneous and occurs only if the solution is supersaturated with respect to the solubilized solid which is to be precipitated.[29] For homogeneous nucleation, the particles (seeds) are produced from spontaneous self-assembly of solubilized precursors which causes an irreversible crystallization through the formation of agglomerates under the conditions of supersaturation.[29] Precipitation continues until simple saturation conditions are reached. Heterogeneous nucleation is more common and the seeds are initiated through contact with structural features, such as impurities, pre-existing seed particles, surface inhomogeneities and defects or by scratching the walls of the container.[29] The second step of the precipitation process is the growth of the nuclei. This is a heterogeneous process that occurs at the solid-solution interface at a rate depending on the speed of migration of the precursor to the particle surface as well as the rate of reaction at the surface.[29] In the nucleation and growth process, the dissolved precursors are repeatedly consumed, and the growth process is terminated once the remaining precursor is insufficient. It should be mentioned that the size of the particles is dependent on the ratio of the rate of nucleation to that

of the crystal growth; the bigger the ratio, the smaller the particle size and vice versa.[29]

Co-precipitation, for the case of mixed oxides, involves the simultaneous precipitation of the solubilized metal precursors from the same. Co-precipitation does not always proceed quantitatively especially if the precipitation pH of the metal precursors differs significantly from one another. It is generally recommended to continuously add the precursors' solution to the precipitant, as opposed to the opposite. [29] Continuous mixing of the precipitate in the mother liquor (precipitation solution) can remarkably alter the properties of the final product. This process is called aging.[29] Figure 1.4 summarizes the main factors that influence the properties of the final product.

1.6 Sol-gel method

The sol-gel method is another widely used synthetic method in the preparation of solid catalysts. The technique allows for the preparation of metal and ceramic oxide materials with tunable pore sizes from relatively cheap precursors under mild conditions. A sol is described as a suspension of colloidal particles with sizes between 1 nm to 1 μm in a continuous liquid medium, which upon coagulation forms a gel - a diphasic material in which solid encapsulates liquids.[28-30] The preparation strategy in the sol-gel process employs monometallic alkoxides $M(OR)_n$ as the precursor which upon hydrolysis form polymeric oxide gels. Step one involves the hydrolysis of the metal alkoxide to produce the corresponding metal hydroxide and alcohol according to the following equation:[29]

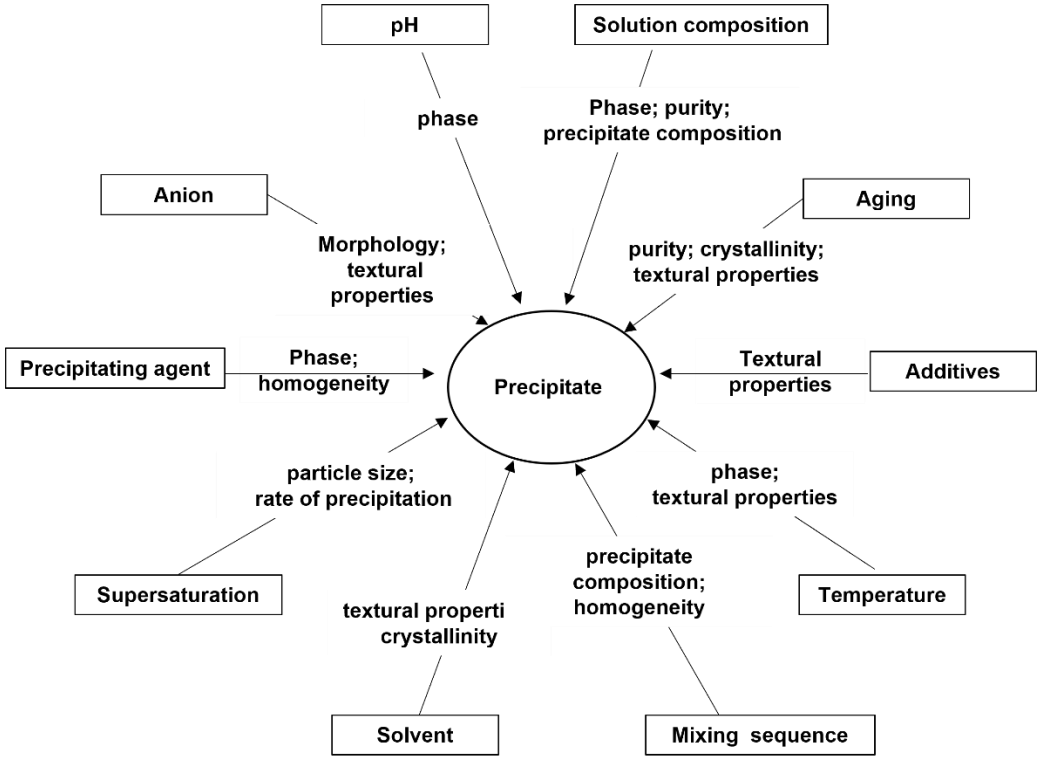

Figure 1.4. Parameters that affect the properties of a final precipitate in a precipitation process. Figure reprinted from reference thirteen.[29]

$$M(OR)_n + xH_2O \rightarrow M(OH)_x + xROH$$

Step two features the condensation of the metal hydroxide to create M-O-M bonds and form sol by dehydration or de-alcoholation per to the following equations:

$$M\text{-}OH + HO\text{-}M \rightarrow M\text{-}O\text{-}M + H_2O$$

or

$$M\text{-}OH + RO\text{-}M \rightarrow M\text{-}O\text{-}M + ROH$$

The final step is the formation of gel which occurs during the aging/drying process via cross-linking.

The sol viscosity increases gradually as the polymerization and cross-linking processes progress till the sol-gel transition point is attained, at which point the viscosity increases abruptly and results in gel formation.[30] The cross-linking process can be facilitated by drying or other dehydration strategies. Notably, the highest density is attained by heating the isolated gel beyond its glass transition temperature.[29] This process is referred to as densification. The composition and morphology of the gel significantly influence the densification rate and transition temperature.[29] The sol-to-gel transition process can be distinguished into three phases: (a) the aging/polymerization process that occurs in the liquid phase, (b) the emergence of macroscopic lattice resulting in an amorphous network, and (c) shrinkage of the gel volume following the evaporation of the solvents leading to a rigid structure.[29] Also, gels with lower cross-linking content can be prepared at low pH with a lower molecular weight alkyl group. Other parameters, including the size

and oxidation state of the cation, the nature and number of the alkyl group, the time in solution (aging), the pH, and temperature, equally play significant roles in the sol-gel process.[29]

1.7 Hydrothermal method

Hydrothermal syntheses are accomplished at elevated temperatures and pressures, taking advantage of the fact that the solubilizing ability and dielectric constant of solvents vary with temperature.[29] While hydrothermal synthesis can be used to fabricate a wide range of materials, it is, however, limited by long reaction times, typically in several hours or days. Also, the requirement of steel autoclaves precludes the real-time monitoring of the reaction progress which constitutes a big disadvantage. Hydrothermal synthesis is widely applied towards the synthesis of zeolites - an important class of porous crystalline materials known for their adsorptive properties and application as industrial catalysts, particularly in the upgrading of crude petroleum feedstock via catalytic cracking to potentially more useful lower molecular weight hydrocarbons that are ultimately used for a large portion of the world's supply of fuels.[31,32]

1.8 Templating method

In a templating method, precipitation of solubilized metal precursors is accomplished in the presence of a template that serves as a structure-directing agent - determines the porosity, shape, morphology, and size of the final solid material. Various kinds of structural materials, including hollow spheres, nanorods,

nanotubes, and nanocubes, have been formulated using the templating method.[33] Templating can be accomplished by means of physical adsorption of species onto the surface of the template or via a chemical process where species are grafted onto the surface of the template through functionalized moieties such as thiols, alcohols, or vinyl groups.[33] Usually, the templates are used as sacrificial entities and are therefore removed by either calcination or chemical etching post-reaction, provided that the material can withstand the removal process. Templates can be classified as either soft or hard.[33] Soft templates include micelles, emulsions, polymers, or surfactants that can be removed easily post-reaction via heat treatment.[33] Hard templates, on the other hand, include 'three-dimensional' colloidal particles like silica or alumina whose surfaces are physically or chemically modified by the precursor of interest or nanostructural 'two-dimensional' surfaces onto which the precursor substrates can be cast.[33]

1.9 Incipient wetness impregnation method

This is by far the most widely used synthetic method to fabricate supported catalysts. In general, pre-formed support with the desired pore features and mechanical toughness is wetted with a solution that contains the precursor of the active species and then dried afterward. If the volume of the solution introduced is less than the pore volume of the support, is referred to as 'dry' impregnation; on the other hand, if the volume of the precursor solution is greater than the pore volume of the support, is called 'wet' impregnation.[34] Impregnation is performed under ambient conditions. The technique relies on capillary force within the pore

to draw the solution throughout the internal volume of the support where they can interact with the pore walls via ion exchange with acidic surface protons or physical adsorption leading to high dispersion of the active phase.[34] The solvents are then evaporated from the pores leading to the precipitation of the active species onto the surface of the support. The evaporated product is subsequently treated via activation treatments like calcination and/or reduction to obtain the desired supported catalysts. The final amount of the precipitated active species can be precisely tuned by varying the amounts of the solubilized precursor. The crystallite size of the active component is influenced by the pore size of the support.[29] Generally, larger pores that can accommodate large volumes of the precursor solution will mainly precipitate large crystals than smaller pores, which can result in an uneven distribution of solid precipitate. It is important therefore to optimize the synthesis parameters since the efficiency of the catalysts is affected by the size of the active component, and their accessibility and distribution over the support.[29] Rapid evaporation of the solvent may result in uneven distribution of the crystallite towards the pore opening, leading to pore blockages. Notably, the use of chloride-based precursors could leave behind some residual chloride atoms that will facilitate sintering and result in increased particle size.[29]

1.10 Deposition-precipitation method

Deposition-precipitation (DP) method is another commonly synthetic strategy for depositing active components as small particles onto solid supports by inducing their precipitation from solubilized metal precursors. Here, a solution of

the metal precursor is added to a suspension of the pre-synthesized solid support which also acts as a nucleation site for exclusive precipitation of the dissolved metal components. The precipitates are thermodynamically stabilized by the presence of support.[29] Notably, the DP method generally produces catalysts that are thermally stable and contain relatively high loading of the active components at a narrow particle size distribution.[29]

1.11 Summary of the synthetic methods and the project goal

While heterogeneous catalysts can be synthesized by means of other synthetic methods, the synthetic strategies presented above are by far the most commonly used. Unfortunately, the majority of these well-established strategies, at some point, require the exposure of the intermediate product to high-temperature heat treatment for an extended period, under which agglomeration of particles occurs with a commensurate decrease in surface area. For most catalytic applications, non-agglomerated particles with high surface areas are preferred. Therefore, accessing nanostructured HEMs with an increased surface area has motivated efforts to explore unconventional synthesis strategies. On the other hand, ultrasound can be used to drive high-energy chemical reactions via the physical process of acoustic cavitation that provides a unique high-energy environment at such magnitude and time scale that is unattainable with conventional energy sources. The overarching goal of this research is to exploit this unique high-energy environment toward the synthesis of nanostructured HEM as an emerging new class of catalytic materials.

1.12 Sound, ultrasound, and acoustic cavitation

Sound is simply waves of compression and expansion traveling through a solid, liquid, or gaseous medium. Sound waves are detectable by human ears when the frequency is between 20 Hz to 20 kHz.[35] Ultrasounds, by definition, are sound waves with frequencies beyond the upper audible limit of human hearing and are generally produced when a high-frequency alternating current is applied to materials with piezoelectric effects.[36] Ultrasound is widely utilized in many different fields: in medicine for sonography, non-surgical removal of kidney stones, treatment of cartilage-related injuries, acoustic targeted drug delivery, and cleaning teeth in dental hygiene;[36] industrially for large-scale mixing and cleaning, cutting of alloys, plastic welding, detection of invisible flaws, non-destructive testing of products and structures, emulsification of foods and cosmetics, ultrasound testing, welding plastics, object detection, and distance measuring;[37,38] in homes for cleaning of pieces of jewelry, burglar alarm systems, vaporizers, dog whistles, etc.[36,37] Animals such as bats and dolphins use ultrasound waves to navigate, prey, identify other species, and avoid running into obstacles.[39-41] However, none of these applications exploits the effect of ultrasound on chemical reactivity, a process called sonochemistry.

1.13 History of sonochemistry

The history of sonochemistry and cavitation effects can be dated back to the late 1800s.[42] The first report on cavitation was published by Sir John I. Thornycroft and Sydney W. Baraby following the field tests of the first British high-

speed torpedo in 1894.[42] Thornycroft and Baraby observed acute vibrations from, and rapid erosion of the submarine's propeller and posited that the large bubbles (or cavities) formed by the rotating propeller and imploded by water pressure, were the source of the vibrations.[42,43] They increased the size of the propeller while reducing its rotation speed to minimize the vibrations from what came to be known as cavitation.[42,43] With the emergence of ships with faster repulsion systems, the phenomenon became an increasingly significant concern, and the Royal navy in 1917 authorized Lord Rayleigh to investigate the issue. Rayleigh reaffirmed that the effects were indeed a consequence of the enormous turbulence, heat, and pressure generated during the catastrophic collapse of the cavitation bubbles on the propeller's surface.[43] While cavitation had continued to pose a serious problem to marine engineers, it has afforded chemists with an extra-ordinary environment to perform high-energy reactions.

Besides turbulent flows in liquids, the phenomenon of cavitation also occurs under high-intensity ultrasonic irradiation. Rather than applying mechanical pressure, cavitation is induced by generating intense sound waves in liquids.[42-45]

The first chemical effect of ultrasound was reported by Alfred L. Loomis in the year 1927.[42,46] For nearly six decades later, the field of sonochemistry laid fallow before being rejuvenated in the 1980s following the development of reliable and affordable laboratory generators of high-intensity ultrasound.

Whereas lights interact with matters at high energies on a short time scale, heats interact at lower energies on prolonged time scales; sound interacts with

matter via the process of cavitation to provide energies on a time scale that are unavailable from other sources.[42]

1.14 Acoustic cavitation phenomenon

Acoustic cavitation is an instantaneous process involving the formation, growth, and implosive collapse of microscopic-sized bubbles during ultrasound irradiation of liquids.[42] When a liquid is irradiated with ultrasound, the expansion cycles exert negative pressure on the liquid, pulling the molecules away from each other. If the ultrasound is adequately intense, the negative pressure wave will overpower the attractive force holding the liquid molecules together, and as a result, gas-filled microscopic-sized bubbles will be formed. These bubbles will absorb energy from ultrasound waves and grow. The growth is determined by the intensity of the ultrasound. At sufficiently high intensity, the bubble will rapidly increase in size via inertial effect leaving no time for the recompression phase of the acoustic cycle.[42] At lower acoustic intensity, bubbles growth will occur by a slower process of rectified diffusion (figure 1.5). During this process, the bubbles will oscillate in size over several expansion-compressions cycles along with a gas inflow, where the average bubble size for each negative pressure phase is large than the compression phase. The bubbles eventually reach a critical size where they can adequately accumulate ultrasound energy within their small volume. Once this critical size is attained, typically tens of micrometers, the bubbles become highly unstable and then experience a rapid inertial overgrowth by coupling to the acoustic field.[42,46] At this point, the bubbles are no longer able to

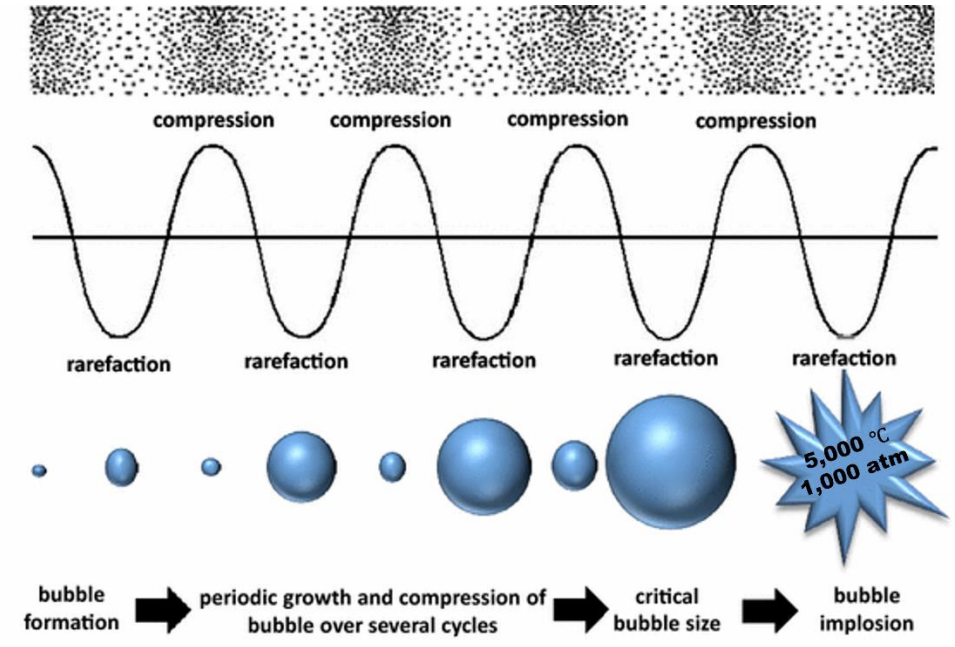

Figure 1.5. Schematic illustration of the acoustic cavitation phenomenon. Figure reprinted from reference forty-seven.[47]

accumulate energy as efficiently and therefore cannot sustain themselves. The nearby liquid dashes in, leading to a catastrophic collapse of the bubbles and the eventual release of concentrated energy confined within the small volume of the heated bubbles. This momentarily raises the temperature of liquids in the immediate environment since the surrounding liquid is still cold and so dissipated the heat almost instantaneously. In other words, one generates a short-lived, localized hotspot in an otherwise cold liquid.[42] The temperature of the generated hotspot is estimated to be above 5000 °C, with pressure exceeding 1000 atm, lifetime significantly less than a microsecond, and heating and cooling rates higher than 10 billion °C s^{-1}.[42,46] Thus, cavitation act as a means of concentrating the diffuse energy of sound into a chemically useful form. [42,46] Our goal is to exploit this unique high-energy environment toward the synthesis of nanostructured HEMs. Notably, the intensity of the implosive bubble can be controlled by such factors as the choice of the liquid, acoustic intensity, acoustic frequency, static pressure, ambient temperature, and choice of ambient gas.[42, 48]

1.15 Assessment of the performance of a catalyst

Generally, catalysts are evaluated based on their activity, yield, selectivity, stability, and overall cost.

The activity of a catalyst is defined as the extent to which the rate of a chemical reaction is enhanced via the action of a catalyst. Catalytic activity can be expressed in turnover frequency (TOF), which is defined as the number of reacting molecules per active site per unit time (equation 1.3).[49]

$$TOF = \frac{1}{N}\frac{dC_A}{dt} \qquad eqn\ (1.3)$$

where N is the number of active sites, C_A is the number of moles of reactant A converted.

Unlike homogeneous catalysts, the complication with heterogeneous catalysts resides in the precise determination of the number of active sites, especially when the reaction occurred predominantly at the interface between active components and the support material or just on a certain structure of the active component.

For carbon monoxide oxidation (CO) oxidation, the light-off curve, that is, the conversion-temperature plot can be used to evaluate catalytic performance. In cases where continuous flow reactors (such as plug reactors used for gas-phase study in heterogeneous catalysis) is employed in the reaction study, the conversion, $\%\ Conv$, can be estimated using the following equation:

$$\%\ Conv = \frac{[R]_{inlet} - [R]_{outlet}}{[R]_{inlet}} \qquad eqn\ (1.4)$$

where $[R]_{inlet}$ and $[R]_{outlet}$ are the concentrations of the reactant measured at the inlet and outlet, respectively.

The light-off curves are excellent plots to evaluate catalytic performance over a wide range of temperatures; they can also be employed in the study of the effect of any pre-treatment process on the overall performance of the catalysts.

However, they cannot be used readily to extract kinetic information. A potentially important piece of kinetic information that can be derived from the light-off curves is the apparent activation energy of the reaction, E_{app}.

The temperature dependence of a reaction constant of a given reaction is expressed in the Arrhenius equation:

$$K = Ae^{-E_a/RT} \qquad eqn\ (1.5)$$

where T is the kelvin temperature, R is the universal gas constant, E_a is the activation energy, *A* is the pre-exponential factor and *K* is the reaction constant. The Arrhenius equation can be written in a non-exponential form that is often more convenient to use and interpret graphically as:

$$\ln(K) = \ln(A) - \frac{E_a}{R}\left(\frac{1}{T}\right) \qquad eqn\ (1.6)$$

The E_a can be determined by plotting the graph of $\ln(K)$ against the reciprocal of temperature, $(1/T)$. It should be mentioned that this approach works only in the so-called kinetic region (0% - 10% conversion), where the concentration of the reactant is still very large that the reaction rate is not affected by the presence of the product. Provided that the reaction is performed at a steady-state where the concentrations of the reactant are constants, we can write that:

$$r = K[CO]^n[O_2]^m = KC_R \qquad eqn\ (1.7)$$

where C_R is a constant and r represents the reaction rate. By substituting the measured rate for K in the Arrhenius equation and plotting the graph of $\ln(r)$ versus $1/T$, the apparent activation energy, E_{app} can be calculated.

Although E_{app} is technically not the true activation energy, variations in E_{app} between similar catalysts imply a difference in intrinsic reactivity or adsorption properties, which can be very useful when comparing catalysts with varying surfaces areas with different or modified compositions.

The yields and selectivity are used to measure the efficiency of a catalyst in the conversion of a given feedstock or substrate to the products of interest and are measures of mass conversion.

The yield of a reaction is the ratio of the desired product formed (in moles) to the total amount that could have been made if the conversion of limiting reactant was 100% and no side reactions occurred.

The selectivity of the desired product is defined as its mole fraction relative to the total number of moles of all products formed

$$Selectivity = \frac{\text{moles of product A formed}}{Sum\ of\ moles\ of\ all\ products\ formed} \qquad eqn\ (1.8)$$

A catalyst with poor selectivity with respect to the desired product generates large amounts of wastes and increases the overall process costs. Because of ununiform distributions of active sites on solid catalysts, the attainment of high selectivity in heterogeneous catalysis is often a formidable task. In addition, the

requirement of high-temperature conditions in many heterogeneously catalyzed processes can introduce several mechanistic pathways towards the production of unwanted products.

1.16 Dissertation overview

This dissertation details both published and unpublished research completed in Dr. Sheng Dai's group over the past four and half years. It is aimed at investigating the feasibility of using ultrasound-derived energy to fabricate HEM nanocatalysts without the use of traditional energy sources.

Chapter 2 summarizes the various characterization techniques used to understand both the physical and chemical properties of the synthesized materials.

Chapter 3 presents a paper published in *ChemSusChem* describing the synthesis and characterization of high-entropy perovskite oxide nanocatalysts via an ultrasound-mediated coprecipitation strategy. Carbon monoxide (CO) oxidation to CO_2 was used as a model reaction to evaluate the catalytic efficiency of the synthesized materials. The published article was slightly revised to accommodate the dissertation format.

Chapter 4 presents another paper published in *Nano Research* describing the design, synthesis, and use of alcoholic ionic liquid in the fabrication of high-entropy alloy nanocatalysts via an ultrasound-driven wet chemistry strategy. The catalytic activity of the as-obtained nanocrystals was evaluated towards selective

hydrogenation of phenol to cyclohexanone. The published article was slightly revised to accommodate the dissertation format.

Chapter 5 presents a paper recently submitted to a scientific journal describing the synthesis and characterization of fluorite-structured high-entropy oxide nanocrystals via an ultrasound-mediated coprecipitation strategy. CO oxidation to CO_2 was used as a model reaction to evaluate the catalytic efficiency of the synthesized materials. The submitted manuscript was slightly revised to accommodate the dissertation format.

Chapter 6 presents a general summary and conclusion as well as some suggestions for future work.

REFERENCES

[1] Catlow, C. R.; Davidson, M.; Hardacre, C.; Hutchings, G. J., Catalysis making the world a better place. *Philosophical Transactions of the Royal Society A: Mathematical, Physical and Engineering Sciences* **2016,** *374* (2061), 20150089.

[2] Schmidt, F., The Importance of Catalysis in the Chemical and Non-Chemical Industries. Springer Berlin Heidelberg: **2004**; pp 3-16.

[3] Védrine, J., Heterogeneous Catalysis on Metal Oxides. *Catalysts* **2017,** *7* (11), 341.

[4] Speight, J. G., 6 - Catalytic cracking. In *The Refinery of the Future (Second Edition)*, Speight, J. G., Ed. Gulf Professional Publishing: **2020**; pp 197-226.

[5] Oh, S. H.; Bissett, E. J., Automotive applications of chemical reaction engineering and future research needs. In *Stud. Surf. Sci. Catal.*, Rhee, H.-K.; Nam, I.-S.; Park, J. M., Eds. Elsevier: **2006**; Vol. 159, pp 17-26.

[6] Wisniak, J., The History of Catalysis. From the Beginning to Nobel Prizes. *Educación Química* **2010,** *21* (1), 60-69.

[7] Murzin, D.; Salmi, T., Chapter 2 - Catalysis. In *Catalytic Kinetics*, Murzin, D.; Salmi, T., Eds. Elsevier Science: Amsterdam, **2005**; pp 27-72.

[8] Catalysis. https://en.wikipedia.org/wiki/Catalysis (accessed 10/22/2021).

[9] Baerns, M.; Holena, M., *Combinatorial Development Of Solid Catalytic Materials: Design Of High-throughput Experiments, Data Analysis, Data Mining*. World Scientific Publishing Company: **2009**.

[10] Mandapaka, R. K.; Madras, G., Microkinetic Modeling of CO Oxidation on

Ionic Palladium-Substituted Ceria. *Ind. Eng. Chem. Res.* **2016,** *55* (8), 2309-2318.

[11] Rost, C. M.; Sachet, E.; Borman, T.; Moballegh, A.; Dickey, E. C.; Hou, D.; Jones, J. L.; Curtarolo, S.; Maria, J.-P., Entropy-stabilized oxides. *Nature Communications* **2015,** *6*, 8485.

[12] George, E. P.; Raabe, D.; Ritchie, R. O., High-entropy alloys. *Nature Reviews Materials* **2019,** *4* (8), 515-534.

[13] Cantor, B.; Chang, I.; Knight, P.; Vincent, A. J. B., *Microstructural development in equiatomic multicomponent alloys*. **2004**; Vol. 375-377, p 213-218.

[14] Yeh, J.-W.; Lin, S.-J.; Chin, T.-S.; Gan, J.-Y.; Chen, S.-K.; Shun, T.-T.; Tsau, C.-H.; Chou, S.-Y., Formation of simple crystal structures in Cu-Co-Ni-Cr-Al-Fe-Ti-V alloys with multiprincipal metallic elements. *Metallurgical and Materials Transactions A* **2004,** *35* (8), 2533-2536.

[15] What are High Entropy Alloys and why are they interesting? http://www.dierk-raabe.com/high-entropy-alloys-overview/ (accessed 10/23/2021).

[16] Yeh, J. W.; Chen, S. K.; Lin, S. J.; Gan, J. Y.; Chin, T. S.; Shun, T. T.; Tsau, C. H.; Chang, S. Y., Nanostructured High-Entropy Alloys with Multiple Principal Elements: Novel Alloy Design Concepts and Outcomes. *Adv. Eng. Mater.* **2004,** *6* (5), 299-303.

[17] Cantor, B., Multicomponent high-entropy Cantor alloys. *Prog. Mater Sci.* **2021,** *120*, 100754.

[18] Qiu, Y.; Liu, R.; Gengenbach, T.; Gharbi, O.; Choudhary, S.; Thomas, S.; Fraser, H. L.; Birbilis, N., Real-time dissolution of a compositionally complex

alloy using inline ICP and correlation with XPS. *npj Materials Degradation* **2020,** *4* (1).

[19] Senkov, O. N.; Miller, J. D.; Miracle, D. B.; Woodward, C., Accelerated exploration of multi-principal element alloys with solid solution phases. *Nature Communications* **2015,** *6* (1), 6529.

[20] Tsai, C.-W.; Lai, S.-W.; Cheng, K.-H.; Tsai, M.-H.; Davison, A.; Tsau, C.-H.; Yeh, J.-W., Strong amorphization of high-entropy AlBCrSiTi nitride film. *Thin Solid Films* **2012,** *520* (7), 2613-2618.

[21] Gild, J.; Zhang, Y.; Harrington, T.; Jiang, S.; Hu, T.; Quinn, M. C.; Mellor, W. M.; Zhou, N.; Vecchio, K.; Luo, J., High-Entropy Metal Diborides: A New Class of High-Entropy Materials and a New Type of Ultrahigh Temperature Ceramics. *Scientific Reports* **2016,** *6*, 37946.

[22] Gild, J.; Braun, J.; Kaufmann, K.; Marin, E.; Harrington, T.; Hopkins, P.; Vecchio, K.; Luo, J., A high-entropy silicide: (Mo0.2Nb0.2Ta0.2Ti0.2W0.2)Si2. *Journal of Materiomics* **2019,** *5* (3), 337-343.

[23] Sun, Y.; Dai, S., High-entropy materials for catalysis: A new frontier. *Science Advances* **2021,** *7* (20), eabg1600.

[24] Dai, S., Across the Board: Sheng Dai on Catalyst Design by Entropic Factors. *ChemSusChem* **2020,** *13* (7), 1915-1917.

[25] Liu, M.; Zhang, Z.; Okejiri, F.; Yang, S.; Zhou, S.; Dai, S., Entropy-Maximized Synthesis of Multimetallic Nanoparticle Catalysts via a Ultrasonication-Assisted Wet Chemistry Method under Ambient Conditions. *Advanced Materials Interfaces* **2019,** *6*, 1900015.

[26] Okejiri, F.; Yang, Z.; Chen, H.; Do-Thanh, C.-L.; Wang, T.; Yang, S.; Dai, S., Ultrasound-driven fabrication of high-entropy alloy nanocatalysts promoted by alcoholic ionic liquids. *Nano Research* **2021**.

[27] Zhang, Y., Preparation of heterogeneous catalysts based on CWAO technology. *Journal of Physics: Conference Series* **2020,** *1549*, 032052.

[28] Campanati, M.; Fornasari, G.; Vaccari, A., Fundamentals in the preparation of heterogeneous catalysts. *Catal. Today* **2003,** *77* (4), 299-314.

[29] Hutchings, G. J.; Védrine, J. C., Heterogeneous Catalyst Preparation. Springer Berlin Heidelberg: **2004**; pp 215-258.

[30] Zhao, H.; Xiong, G.; Baron, G. V., Pore-wall modified metal/ceramic catalytic membranes prepared by the sol-gel method. In *Stud. Surf. Sci. Catal.*, Delmon, B.; Jacobs, P. A.; Maggi, R.; Martens, J. A.; Grange, P.; Poncelet, G., Eds. Elsevier: **1998**; Vol. 118, pp 717-724.

[31] Martínez, C.; Corma, A., 5.05 - Zeolites. In *Comprehensive Inorganic Chemistry II (Second Edition)*, Reedijk, J.; Poeppelmeier, K., Eds. Elsevier: Amsterdam, 2013; pp 103-131.

[32] Wise, W. S., MINERALS | Zeolites☆. In *Reference Module in Earth Systems and Environmental Sciences*, Elsevier: **2013**.

[33] Xie, Y.; Kocaefe, D.; Chen, C.; Kocaefe, Y., Review of Research on Template Methods in Preparation of Nanomaterials. *Journal of Nanomaterials* **2016,** *2016*, 1-10.

[34] Sietsma, J. R. A.; Jos van Dillen, A.; de Jongh, P. E.; de Jong, K. P., Application of ordered mesoporous materials as model supports to study catalyst

preparation by impregnation and drying. In *Stud. Surf. Sci. Catal.*, Gaigneaux, E. M.; Devillers, M.; De Vos, D. E.; Hermans, S.; Jacobs, P. A.; Martens, J. A.; Ruiz, P., Eds. Elsevier: **2006**; Vol. 162, pp 95-102.

[35] Waye, K. P., Effects of Low-Frequency Noise and Vibrations: Environmental and Occupational Perspectives. In *Encyclopedia of Environmental Health*, Nriagu, J. O., Ed. Elsevier: Burlington, **2011**; pp 240-253.

[36] Goldstein, A.; Powis, R. L., 2 - Medical Ultrasonic Diagnostics. In *Physical Acoustics*, Thurston, R. N.; Pierce, A. D.; Papadakis, E. P., Eds. Academic Press: **1999**; Vol. 23, pp 43-195.

[37] Keilman, G., Unusual Applications of Ultrasound in Industry. *Physics Procedia* **2016,** *87*, 79-84.

[38] Awad, T. S.; Moharram, H. A.; Shaltout, O. E.; Asker, D.; Youssef, M. M., Applications of ultrasound in analysis, processing and quality control of food: A review. *Food Research International* **2012,** *48* (2), 410-427.

[39] Kim, S., 7 - Bio-inspired engineered sonar systems based on the understanding of bat echolocation. In *Biomimetic Technologies*, Ngo, T. D., Ed. Woodhead Publishing: **2015**; pp 141-160.

[40] Au, W. W. L., Echolocation. In *Encyclopedia of Marine Mammals (Second Edition)*, Perrin, W. F.; Würsig, B.; Thewissen, J. G. M., Eds. Academic Press: London, **2009**; pp 348-357.

[41] Maltby, A.; Jones, K. E.; Jones, G., Chapter 2.4 - Understanding the evolutionary origin and diversification of bat echolocation calls. In *Handbook of Behavioral Neuroscience*, Brudzynski, S. M., Ed. Elsevier: **2010**; Vol. 19, pp 37-

47.

[42] Suslick Kenneth, S., Sonochemistry. *Science* **1990,** *247* (4949), 1439-1445.

[43] Bang, J. H.; Suslick, K. S., Applications of Ultrasound to the Synthesis of Nanostructured Materials. *Adv. Mater.* **2010,** *22* (10), 1039-1059.

[44] Xu, H.; Zeiger, B. W.; Suslick, K. S., Sonochemical synthesis of nanomaterials. *Chem. Soc. Rev.* **2013,** *42* (7), 2555-2567.

[45] Gedanken, A., Using sonochemistry for the fabrication of nanomaterials. *Ultrason. Sonochem.* **2004,** *11* (2), 47-55.

[46] Suslick, K. S. The Chemistry of Ultrasound. https://suslick.scs.illinois.edu/sonochembrittanica.html (accessed 10/23/2021).

[47] Vyas, N.; Manmi, K.; Wang, Q.; Jadhav, A. J.; Barigou, M.; Sammons, R. L.; Kuehne, S. A.; Walmsley, A. D., Which Parameters Affect Biofilm Removal with Acoustic Cavitation? A Review. *Ultrasound in Medicine & Biology* **2019,** *45* (5), 1044-1055.

[48] Shah, Y. T.; Pandit, A. B.; Moholkar, V. S., Factors Affecting Cavitation Behavior. Springer US: **1999**; pp 55-83.

[49] Kozuch, S.; Martin, J. M. L., “Turning Over” Definitions in Catalytic Cycles. *ACS Catal.* **2012,** *2* (12), 2787-2794.

CHAPTER 2: INSTRUMENTATION AND CHARACTERIZATION TECHNIQUES

2.1 Catalyst characterization

This chapter discusses the main characterization techniques used to understand the crystalline nature, chemical composition, surface chemistry, and textural features of the fabricated nanocatalysts and their relationship to catalytic performance.

2.2 X-ray diffraction

X-ray diffraction (XRD) is an effective non-destructive technique for studying the crystal structure of crystalline/semicrystalline materials. Unlike electron microscopy techniques that view only localized areas of a sample, XRD enables a relatively fast sampling of the material bulk. Various pieces of information that can be obtained from XRD this technique includes crystallinity level, crystal phases, interplanar spacing, preferred crystal orientation, and other structural parameters including average grain size, strain, and crystal defects.[1] XRD technique takes advantage of the dual wave-particle nature of electromagnetic radiation and utilizes the X-ray scattering phenomenon by regular ordered arrays of components in crystalline lattice to construct a unique diffraction pattern that bestows a qualitative image of the atomic arrangements within the lattice.[1] Every crystalline material possesses a discreet atomic structure and when irradiated with a monochromatic collimated beam of X-rays causes constructive

and destructive interferences of the diffracted X-rays, producing a definite diffraction pattern. A quick search of a standard database library of diffraction patterns enables rapid identification of the crystalline phases of a wide range of crystalline materials.

The diffraction of X-rays incident on the crystalline sample is governed by Bragg's law expressed in equation 2.1:

$$n\lambda = 2dsin\theta \qquad eqn\ 2.1$$

where n is an integer, known as order the reflection, λ is the wavelength of the monochromatic beam of incident X-ray, d is interplanar between pairs of adjacent planes, θ is the angle of incidence (Bragg angle). Figure 2.1 illustrates Bragg's law. Constructive interference occurs only when Bragg's law is satisfied, hence, a family of planes only produces diffraction peaks at only a specific angle. Whereas peaks positions are determined by the interplanar spacing, peak intensities are determined by the atomic positions within the diffracting planes.[1] While amorphous materials display intensity maximum over several degrees of angles (2θ), crystalline materials exhibit well-defined peaks at specific scattering angles. Figure 2.2 shows typical diffraction patterns of amorphous versus crystalline materials.

Ideally, the Bragg diffraction peak defines a line with no width. The diffraction peaks from real-life samples, however, produce peaks with a certain width. This phenomenon is known as peak broadening. The peak width is determined by the grain size and is inversely related to it. Generally, peak width widens as the crystallite size decreases. The average crystallite size of the sample

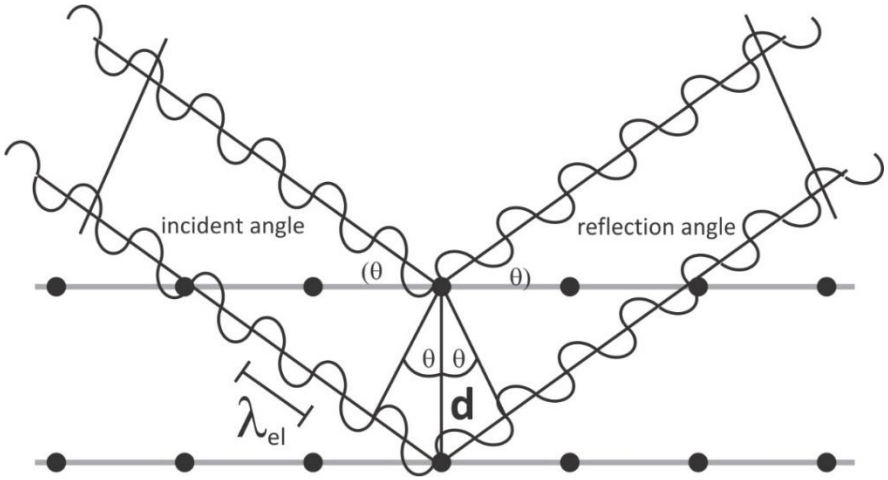

Figure 2.1. Bragg analysis for X-ray diffraction by adjacent planes within a crystal lattice. . Figure reprinted from reference three.[3]

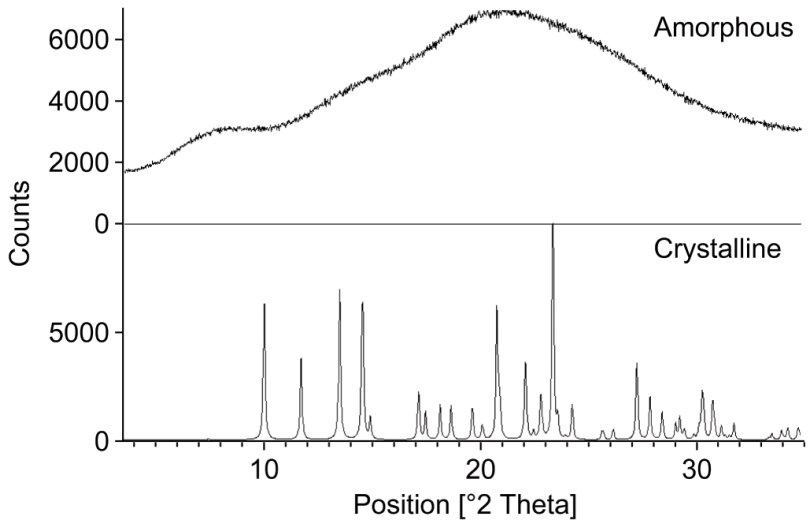

Figure 2.2. Typical XRD patterns of a crystalline and an amorphous and crystalline material. Figure reprinted from reference four.[4]

can be estimated by applying the Scherrer formula given in equation 2.2.[2] Scherrer equation assumes that crystallite size is the primary source of line broadening in diffraction peaks. It is important to note, however, that other factors such as instrument profile and microstrain can also contribute.[5]

According to Scherrer's equation[2], the crystallite size, *D* can be determined by:

$$D = \frac{\lambda k}{\beta \cos\theta} \qquad eqn\ 2.2$$

where: $D\ (nm)$ is the crystallite size normalized to the reflecting plane, $k\ (0.94)$ is the shape factor (but differs with crystallite shape), λ is the wavelength of the incident X-ray in nm, β is the full width at half maximum intensity (FWHM) of the peaks in radians, and θ is the Bragg angle.

2.3 X-ray photoelectron spectroscopy

X-ray photoelectron spectroscopy (XPS) is a surface-sensitive, non-destructive, quantitative spectroscopic technique used to determine the elemental composition, empirical formula, electronic state, and chemical state of elements that exist within a material (except for H and He) with an atomic sensitivity of 0.1% – 1.0%.[6] XPS utilizes low-energy X-rays (such as MgKα and AlKα) to eject core-level electrons with quantized binding energy from the surface of the sample, adding any excess energy over the binding energy to the kinetic energy of the free electrons.[6] The kinetic energy and the number of ejected photoelectrons from the surface of the sample are measured with the aid of an electron energy analyzer.

Since the energy of the incident X-ray is known, the binding energy of the electrons can be determined from the kinetic energy of the free electrons using the equation below:[6]

$$E_p - (E_k + \Phi) = E_b \qquad eqn\ 2.3$$

where E_p is the photon energy of the incident X-ray, E_k is the kinetic energy of the ejected electrons measured by the electron-energy analyzer, and Φ is the work function of the electron energy analyzer, and E_b is the binding energy of the ejected electrons.

Since every element shows a set of characteristic XPS peaks at a unique binding energy value, the energy spectrum of the photoelectrons can be used to ascertain the electronic structures of the atoms that the electrons originated from. By measuring the integrated area under a given elemental peak, quantitative information can be obtained.

2.4 Electron microscopy

Advanced electron microscopy techniques such as scanning electron microscopy (SEM) and transmission electron microscopy (TEM) are important characterization techniques for elucidating the morphology, structure, chemical composition, and electronic properties of a sample. This technique utilizes a focused beam of electrons, which upon interaction with the samples produces different signals including elastic or inelastically scattered electrons, X-rays, Auger electrons, etc.[7]

2.4.1 Scanning electron microscopy

Scanning electron microscopy (SEM) is used to ascertain microscopic structure and topographical features of materials.[8,9] This surface-imaging technique produces, high-magnification, high-resolution images of samples by scanning their surface in a raster pattern with a focused electron beam. The negatively charged incident electron beam interacts with the electron clouds of the samples, producing various signals that can be used to obtain topographic details and atomic composition of the surface being scanned.[10] Present-day SEM can magnify objects up to 1,000,000 times their original size and can resolve features below 1 nm in dimension.[9] The resolving power of an SEM depends on several factors including the electron spot size and the interaction volume of the electron beam with the specimen.[9]

In SEM technique, the sample-electron interaction generates different kinds of electrons or characteristic X-rays that can be detected using the appropriate detector.[8, 9] SEM images can be constructed using two different types of electrons: the backscattered electrons (BSE) and the secondary electrons (SE). BSEs originate from the primary electron beam that are reflected back following elastic interactions with the specimen.[8,9] BSE detectors are typically solid-state detectors that are positioned above the samples, concentrically to the electron beam for optimized BSE collection. On the other hand, SEs originate from the surface of the specimen mainly detected by scintillating material that generates a flash of light for every electron.[8, 9] These flashes are amplified by a photomultiplier tube; images are formed by correlating the sample scan position with the resulting signal. The

detector is usually positioned at an angle at the side of the electron to maximize the SE collection. While BSE is more sensitive to differences in atomic number (the higher the atomic number, the brighter the spots that show in the image), SE provides more details on sample morphology/topography.[8]

Also, the primary electron beam can cause the emission of characteristic X-rays via interaction with atoms on the surface of the sample.[8] These generated X-rays can be used to elucidate the elemental composition of the sample (since every element produces X-rays with specific energy) via a technique called energy dispersive X-Ray analysis (EDX).

2.4.2 Transmission electron microscopy (TEM)

In TEM, electromagnetic lenses are used to focus high-energy electrons into a small, thin, coherent beam and onto the path of an ultrathin sample. The transmitted or scattered electrons signals are magnified by a series of electromagnetic lenses and then observed by electron diffraction, amplitude-contrast imaging such as diffraction contrast, or phase-contrast imaging such as high-resolution TEM (HR-TEM).[7] Whereas electron diffraction patterns can provide information about the crystallographic structure of the sample on a fine scale, the amplitude-contrast images give information about the chemistry and microstructure of the sample and its defects.[1,7] Phase-contrast imaging (HR-TEM) is capable of direct imaging of the crystallographic structure of a specimen at an atomic-scale resolution.[7] In addition to the high spatial resolution of TEM, several analytical techniques can be attached to the TEM for qualitative and qualitative

analysis of the chemical compositions of the specimen sample.[1, 7] Examples include the energy-dispersive X-ray spectroscopy (EDX) and energy loss spectroscopy (EELS), for chemical composition and electronic structure elucidation, respectively.[7]

Some modern TEM instruments are commuted to the STEM (scanning transmission electron microscopy) mode where an analyst can benefit from the advantages of both SEM and TEM techniques. STEM utilizes a highly focused electron probe to raster-scan across the sample where various types of scattering are acquired as a function of position. Rasterizing the electron beam in this manner significantly enhances the versatility microscope.[7]

The transmitted electrons at high scattering angles are used to form directly interpretable, chemically sensitive, high-resolution, atomic number (-Z) contrast images.[1, 7] The generated X-rays can be detected using an EDS detected and used to generate high spatial resolution compositional maps.

2.5 BET surface area and porosity measurement

Adsorption-desorption isotherm coupled with Brunauer, Emmett, and Teller (BET) theory is a standard technique in which specific surface area, pore-volume, and pore size distribution of solid catalyst are determined through the adsorption of an unreactive gas.[11] The BET theory is an extension of Langmuir's theory of monolayer adsorption to multilayers adsorption. The theory presupposes the outermost layer of molecules in an adsorbed stack are in dynamic equilibrium with

the vapor – just like the monolayer adsorbate and that there is no 'horizontal' interaction between molecules at different sites.[11]

In the nitrogen sorption experiment, for example, used in this work, first, the solid is evacuated to remove any pre-adsorbed species. Next, the catalyst is cooled to liquid nitrogen temperature at constant temperature or under isothermal conditions, while increasing the concentration or pressure of the absorbing nitrogen gas. The quantity of the physisorbed nitrogen is then measured. The capacity of the monolayer is determined by fitting the resulting adsorption isotherm to the BET equation below:

$$\frac{1}{\mathrm{V}[(\mathrm{P_o}/\mathrm{P})-1]} = \frac{1}{V_m C} + \frac{C-1}{V_m \mathrm{C}}\left(\frac{P}{P_\mathrm{o}}\right) \qquad eqn\ 2.4$$

where V is the quantity of the adsorbed N_2 at pressure P, P and P_o are the equilibrium and saturation pressures of the adsorbate at the temperature of adsorption, V_m is the monolayer capacity, C is the BET constant which is related to the heat of adsorption. BET describes a linear plot $1/[[\mathrm{V}(\mathrm{P_o}/\mathrm{P})-1]$ versus (P/P_o) which for most solid that utilized N_2 as the adsorbing gas is confined to a limited region of the adsorption isotherm, usually in the range of $0.05 \leq (P/P_\mathrm{o}) \leq 0.35$. Hence, the slope and intercept of the curve can be solved to determine the monolayer capacity, V_m. From this, the total surface area, S_t can be determined since the cross-sectional area of the adsorbate is usually known.

$$S_t = (V_m N_A A_x)/V_n \qquad eqn\ 2.5$$

Where N_A is the Avogadro's number, A_x is the cross-sectional area of the adsorbate, V_n is the molar volume of the adsorbing gas. Conventionally, the

surface area is expressed on a per gram basis; therefore, the total surface area can be divided by the weight of the sample to obtain its specific surface areas (SSA) in m^2/g.

While nitrogen gas is the most widely used adsorbate, other gases such as argon or xenon can be utilized for samples with low surface area.

Meanwhile, for pore size analysis, the pressure is continually increased until the gases condense inside the pore of the material, starting with the smallest. The pressure is then gradually reduced to allow for evaporation of the condensed gases.[11] Through the analyses of the hysteresis loop created by this process, the pore size, volume, and shape can be determined. The Barrett-Joyner-Halenda (BJH) theory can be used to determine the pore size distribution.[11]

2.6 Fourier-transform infrared (FTIR) spectroscopy

Infrared (IR) absorption spectroscopy is used to obtain chemical information about the molecular structure of a material by identifying characteristic vibrational bands of bonded units.[12,13]

Modern IR spectrometers are configured as Fourier-transform infrared (FTIR) instruments. The full spectrum of IR radiation is passed through an interferometer which consists of a beam splitter, a moving mirror, and a fixed mirror. The beams are split into two parts: one part is reflected in a fixed mirror and the part is transmitted to a moving mirror that moves back and forth at a constant speed. The beams are reflected from the two mirrors, recombine at the beam splitter creating an interference pattern before reaching the sample specimen

where some of the energy is absorbed and some transmitted. The absorbance spectrum is obtained after Fourier transform of the interferogram that converts the intensity versus the optical path difference plot into intensity versus wavenumber spectrum.[13]

To probe the surface chemistry of a solid catalyst, a diffuse reflectance infrared Fourier transform (DRIFT) accessory is attached to the instrument. Here, the IR radiation is directed onto the surface of the catalysts where they are scattered in many directions due to the rough surface of the powder.[14] The DRIFTS accessory contains a strategically positioned ellipsoidal/parabolic mirror that directs the scattered IR radiation towards the detector for signal processing. This is a very powerful technique for investigating the nature and surface features of a heterogeneous catalyst. For instance, the interaction between CO and a metal active center can induce a π – backbonding through the donation of electron pairs from the metal center to the π* orbital of CO, weakening the C-O interaction and lowering the vibrational frequency of CO.[15] As the oxidation state of the metal decreases, so does the vibrational frequency.[15] Thus, by monitoring the changes in the C-O stretching vibration using DRIFTS, one can see changes in the electronic states of the metal-binding sites.

2.7 Gas chromatography (GC)

Gas chromatography (GC) is an important analytical technique used for the analysis of compounds that be vaporized without decomposing. The GC method of separating sample mixtures is based on their interaction with a stationary phase

of the column as they travel through. These liquids or gaseous sample mixture is pushed through by an inert carrier gas such as He, Ar, or N_2, and the molecules travel at different rates depending on their adsorption strength with the stationary phase and therefore elute at different times. The time taken for a given analyte to pass through the column after being injected is called its retention time. The column, column temperature, injection temperature, carrier gas flow rate, etc are critical for good separation and can be optimized via method development.[16]

As the sample leaves the GC column, it is fed into a detector to generate the chromatograph which is a signal intensity that is plotted against the retention times of the analytes. Once the chromatogram is generated, analytes are qualitatively determined by their order of elution.

For quantitative analysis, a calibration curve can be made by injecting the standard mixtures of the analytes so that integration of the chromatography peaks can produce an accurate value of the concentration of each analyte.

REFERENCES

[1] Kaliva, M.; Vamvakaki, M., Chapter 17 - Nanomaterials characterization. In *Polymer Science and Nanotechnology*, Narain, R., Ed. Elsevier: **2020**; pp 401-433.

[2] Patterson, A. L., The Scherrer Formula for X-Ray Particle Size Determination. *Physical Review* **1939,** *56* (10), 978-982.

[3] X-ray Diffraction. https://www.letstalkacademy.com/publication/read/x-ray-diffraction (accessed 10/23/2021).

[4] Lee, A. Y.; Erdemir, D.; Myerson, A. S., Crystals and Crystal Growth. In *Handbook of Industrial Crystallization*, 3 ed.; Lee, A. Y.; Myerson, A. S.; Erdemir, D., Eds. Cambridge University Press: Cambridge, **2019**; pp 32-75.

[5] Williamson, G. K.; Hall, W. H., X-ray line broadening from filed aluminium and wolfram. *Acta Metall.* **1953,** *1* (1), 22-31.

[6] Oswald, S., X-Ray Photoelectron Spectroscopy in Analysis of Surfaces. *Encyclopedia of Analytical Chemistry* **2013**.

[7] Su, D., Advanced electron microscopy characterization of nanomaterials for catalysis. *Green Energy & Environment* **2017,** *2* (2), 70-83.

[8] de Assumpção Pereira-da-Silva, M.; Ferri, F. A., 1 - Scanning Electron Microscopy. In *Nanocharacterization Techniques*, Da Róz, A. L.; Ferreira, M.; de Lima Leite, F.; Oliveira, O. N., Eds. William Andrew Publishing: **2017**; pp 1-35.

[9] Ul-Hamid, A., Introduction. In *A Beginners' Guide to Scanning Electron Microscopy*, Ul-Hamid, A., Ed. Springer International Publishing: Cham, **2018**; pp 1-14.

[10] Amonpattaratkit, P.; Ananta, S., Effects of calcination temperature on phase formation and particle size of Zn2Nb34O87 powder synthesized by solid-state reaction. *Mater. Chem. Phys.* **2013,** *139* (2), 478-482.

[11] Chapter 13 Adsorption methods for the assessment of the specific surface area, the pore size distribution and the active sites of heterogeneous catalysts. In *Stud. Surf. Sci. Catal.*, van Santen, R. A.; van Leeuwen, P. W. N. M.; Moulijn, J. A.; Averill, B. A., Eds. Elsevier: **1999**; Vol. 123, pp 543-566.

[12] Grainger, D. W.; Castner, D. G., 3.301 - Surface Analysis and Biointerfaces: Vacuum and Ambient In Situ Techniques. In *Comprehensive Biomaterials*, Ducheyne, P., Ed. Elsevier: Oxford, **2011**; pp 1-22.

[13] Colthup, N. B., Infrared Spectroscopy. In *Encyclopedia of Physical Science and Technology (Third Edition)*, Meyers, R. A., Ed. Academic Press: New York, **2003**; pp 793-816.

[14] Lercher, J. A.; Jentys, A., Chapter 13 - Infrared and Raman Spectroscopy for Characterizing Zeolites. In *Stud. Surf. Sci. Catal.*, Čejka, J.; van Bekkum, H.; Corma, A.; Schüth, F., Eds. Elsevier: **2007**; Vol. 168, pp 435-476.

[15] Bistoni, G.; Rampino, S.; Scafuri, N.; Ciancaleoni, G.; Zuccaccia, D.; Belpassi, L.; Tarantelli, F., How π back-donation quantitatively controls the CO stretching response in classical and non-classical metal carbonyl complexes. *Chemical Science* **2016,** *7* (2), 1174-1184.

[16] Shellie, R. A., Gas Chromatography. In *Encyclopedia of Forensic Sciences (Second Edition)*, Siegel, J. A.; Saukko, P. J.; Houck, M. M., Eds. Academic Press: Waltham, **2013**; pp 579-585.

CHAPTER 3: ROOM-TEMPERATURE SYNTHESIS OF HIGH-ENTROPY PEROVSKITE OXIDE NANOPARTICLE CATALYSTS THROUGH ULTRASONICATION-BASED METHOD

3.1 Publication disclosure

This chapter is based on a previously published article referenced below: Okejiri, F.; Zhang, Z. H.; Liu, J. X.; Liu, M. M.; Yang, S. Z.; Dai, S. Room-temperature synthesis of high-entropy perovskite oxide nanoparticle catalysts through ultrasonication-based method. *ChemSusChem* **2020**, 13, 111–115.

My contributions to this work include identification of the research objectives, searching of relevant literature, design and conducting of the synthetic experiments, characterization of the samples except for the electron microscopy, which was conducted by Shize Yang, drafting of the manuscript with reviews and edits from all listed authors.

3.2 Abstract

In the present study, a sonochemical-based method for one-pot synthesis of entropy-stabilized perovskite oxide nanoparticle catalysts with a high surface area was developed. The high-entropy perovskite oxides were synthesized as monodispersed, spherical nanoparticles with an average crystallite size of approximately 5.9 nm. Taking advantage of the acoustic cavitation phenomenon in the ultrasonication process, $BaSr(ZrHfTi)O_3$, $BaSrBi(ZrHfTiFe)O_3$, and $Ru/BaSrBi(ZrHfTiFe)O_3$ nanoparticles were crystallized as single-phase

perovskite structures via ultrasound irradiation without calcination. Notably, the entropically-driven stability of Ru/BaSrBi(ZrHfTiFe)O_3 with excellent dispersion of Ru in the perovskite phase bestowed the nanoparticles with good catalytic activity for CO oxidation.

3.3 Introduction

A significant breakthrough in multicomponent alloy systems has inspired the exploration of the vast compositional space offered by high-entropy materials (HEMs).[1-6] HEMs are based on the premise of incorporating multiple components (usually five or more) into a single crystal phase to attain a unique combination of properties that are otherwise unattainable in conventional solid solutions.[7] Among this novel class of crystalline materials, high-entropy alloys were first reported in 2004 by the independent pioneering works of Cantor et al. and Yeh et. al.[5,6] Recent studies have extended the high-entropy concept to include the ionic compounds, where five or more metallic elements have been used to populate a single cation sublattice to introduce high-configurational entropy into the crystal structure. Examples include the high-entropy metal diborides,[2] high-entropy nitrides,[8,9] and high-entropy metal-oxides (HEMOs).[10] More recently, Jiang et al. extended the HEMO study to include the perovskite-type oxides with six and seven metallic elements.[11] The synthesis involved blending and ball milling of stoichiometric amounts of the corresponding metal-oxide precursors for approximately 6 hours and subsequent calcination at temperatures above 1300 °C to form the high-entropy perovskite oxide (HEPO) ceramics. Although the particle size distribution

of the synthesized perovskites was not reported, several studies have demonstrated that such extreme temperature during the synthetic process causes coagulation of grain boundaries, leading to the formation of clumps, and consequent reduction in the available surface area for reactions.[10,12,13] Although traditional perovskites with high surface areas have been previously made,[14,15] high-entropy perovskites with high surface area, have not been reported previously to the best of our knowledge.

Perovskites are an important class of materials that exhibit a wide range of functionality, making them desirable for use in different areas of application including heterogeneous catalysis.[16] In 1975, Gallagher et al. reported the use of perovskites as a potential replacement for noble-metal-based catalysts in automotive exhaust systems.[17] The initial enthusiasm was however dampened by the inherent low surface area and sulfur poisoning associated with this material type. Although there are evidences of sulfur-tolerant and high-surface-area traditional perovskites in literature,[15,18,19] their comparative inferior catalytic activity has so far remained the most important limiting factors for their practical application. The traditional solid-state reaction and solution-mediated processes commonly used for the synthesis of high-entropy materials, at some stage, require calcination in extreme temperature conditions that cause nucleation of nanoclusters and more particle growth. It is therefore imperative to develop synthesis strategies that are not limited by this temperature requirement. Sonochemical synthesis is one of such unique techniques; it relies on an acoustic cavitation phenomenon from high-intensity ultrasound irradiation to initiate

chemical changes. The acoustic cavitation phenomenon, which can be described as the formation, successive growth, and implosive collapse of microscopic-sized bubbles in ultrasound-irradiated liquids, generates massive in a microscopic region with temperatures above 5000 °C, pressures exceeding 2000 atm in a timescale of ≤ 10^{-9} s.[20]

Thermodynamically, the Gibbs free energy associated with the formation of crystalline, entropy-stabilized, perovskite nanoparticles in sonochemical synthesis can be expressed as $\Delta G_{mix} = \Delta H_{mix} - T\Delta S_{mix}$; because the entropic contributions to Gibbs free energy are temperature dependent, we believe that the extremely localized release of massive energy (5000 °C) in momentary lifespan, would overpower the enthalpy contributions and afford a seemingly room-temperature synthesis of nanocrystals – a process that will otherwise require calcination for an extended period of time. In the absence of any available literature, we report the first sonochemical synthesis of entropy-stabilized, single-phase, perovskite oxide nanoparticle catalysts: Ru/BaSrBi(ZrHfTiFe)O_3 for carbon monoxide (CO) oxidation. The entropically-driven stability of Ru/BaSrBi(ZrHfTiFe)O_3 with excellent dispersion of Ru in the perovskite phase, conferred the nanoparticles with good catalytic activity for CO oxidation. This technically feasible and facile synthetic approach holds great promises for the development of other classes of HEMs with large surface areas. Via this method, $BaZrO_3$ and the high-entropy analogues - $Ba_{0.5}Sr_{0.5}(Zr_{0.4}Hf._{0.3}Ti_{0.3})O_3$, $Ba_{0.4}Sr_{0.4}Bi_{0.2}(Zr_{0.3}Hf_{0.3}Ti_{0.2}Fe_{0.2})O_3$, and $Ru_{0.13}/Ba_{0.3}Sr_{0.3}Bi_{0.4}(Zr_{0.2}Hf_{0.2}Ti_{0.2}Fe_{0.27})O_3$ (referred to as HEPO-5, HEPO-7 and Ru/HEPO-7, respectively) were synthesized and characterized.

3.4 Materials

All the chemical reagents used in this work were of analytical grade. Barium chloride dihydrate (99.0 % $BaCl_2 \cdot 2H_2O$, Fischer chemicals, USA), strontium chloride hexahydrate (99.0% $SrCl_2 \cdot 6H_2O$, Acros, USA), bismuth nitrate hydrate (99.9% $Bi(NO_3)_3 \cdot xH_2O$, Alfa Aesar, USA), zirconium chloride (98% $ZrCl_4$, Acros, USA), hafnium chloride (99.9% $HfCl_4$, Alfa Aesar, USA), titanium chloride (99.9% $TiCl_4$, Acros, USA), iron (III) nitrate nonahydrate (99.0% $Fe(NO_3)_3 \cdot 9H_2O$, Acros, USA), Alfa Aesar, USA) and ruthenium chloride (98.0% $RuCl_3$, Alfa Aesar, USA) were all used as received without further purification.

3.5 Synthesis method

To synthesize high-entropy perovskite metal-oxide NPs with eight metallic elements - $Ru_{0.13}/Ba_{0.3}Sr_{0.3}Bi_{0.4}(Zr_{0.2}Hf_{0.2}Ti_{0.2}Fe_{0.27})O_3$ stoichiometric amounts of $BaCl_2 \cdot 2H_2O$ (0.63 mmol), $SrCl_2 \cdot 6H_2O$ (0.63 mmol), $Bi(NO_3)_3 \cdot xH_2O$ (0.84 mmol), $ZrCl_4$ (0.42 mmol) and $HfCl_4$ (0.42 mmol) were mixed together in a scintillating vial and dissolved with 2.5 mL 0.42 mmol solution of $TiCl_4$. In a separate vial, stoichiometric amounts of $Fe(NO_3)_3 \cdot 9H_2O$ (0.56 mmol) and $RuCl_3$ (0.28 mmol) were dissolved in 2.5 mL DI and stirred for about 15 minutes. Following this, the ultrasonication equipment was set and the precursors were gradually introduced into the sonication glassware that contains 20.0 mL of a 20.0 M NaOH solution as the precipitating agent in a 50 mL beaker. These mixtures were exposed to ultrasonic irradiation by direct immersion of an ultrasonic titanium horn operating

at 20 kHz. The ultrasonic processor with a maximum power output of 750 watts was purchased from Sonics & Materials, INC. and equipped with a cylindrical probe of ¾ ″ diameter. The instrument was operated in pulsed mode at 9 seconds on 3 seconds off under 45 % amplitude for about 10 mins. When the sonication was finished, the resulting precipitate was allowed to cool to room temperature and then separated by centrifugation. The solid was washed four times with DI water before being dried in an oven at 80 °C for 3 hours to obtain the final crystallite. $BaZrO_3$, $BaRuO_3$, $Ba_{0.5}Sr_{0.5}(Zr_{0.4}Hf_{.0.3}Ti_{0.3})O_3$, and $Ba_{0.4}Sr_{0.4}Bi_{0.2}(Zr_{0.3}Hf_{0.3}Ti_{0.2}Fe_{0.2})O_3$ were synthesized in a similar fashion using the corresponding metal precursors and by adjusting the respective molar ratios. $BaRuO_3$ in particular was calcined at 750 °C under air to obtain the single-phase perovskite structure. Figure 3.1 is a schematic illustration of the general synthetic procedure.

3.6 Characterization

The powder X-ray diffraction (XRD) data were collected on a PANalytical Empyrean diffractometer with Cu K_α radiation operated at 45 kV and 40 mA (scanning step: 0.02° per step). The crystallite size was estimated using Scherrer's equation: $D_{XRD} = (\lambda \mathrm{K})/(\beta \cos\theta)$; where: D_{XRD} is the crystallite size (nm) normalized to the reflecting plane, K is the shape factor (0.94), λ is the wavelength of the X-ray in nm (0.15406), β is the full width at half maximum intensity (FWHM) in radians, and θ is the scattered angle. The nitrogen adsorption and desorption isotherms were recorded at 77 K using Gemini 2375 surface area analyzer.

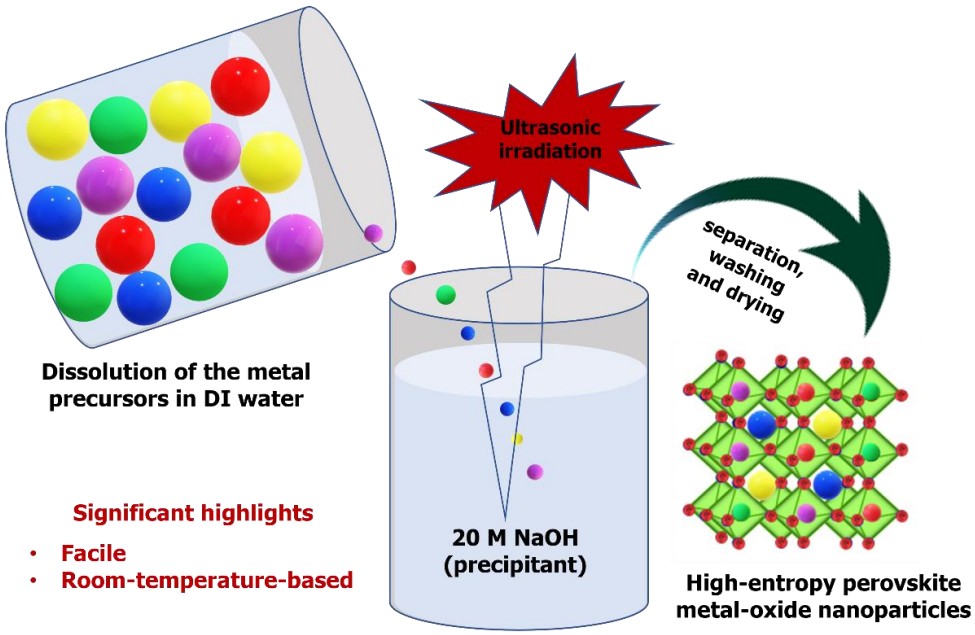

Figure 3.1. Schematic illustration of the sonochemical-based synthesis of HEPO-5 nanoparticles [$BaSr(ZrHfTi)O_3$].

The elemental composition was determined by inductively coupled plasma optical emission spectroscopy (ICP-OES) analysis performed on an Agilent 5110 ICP-OES spectrometer. The sample was dissolved in aqua regia and diluted with 2.0% nitric acid prior to analysis.

High-angle annular dark-field scanning transmission electron microscopy (HAADF-STEM) images and EDX mappings were collected on the FEI Talos F200X microscope operated at 200 keV.

The catalytic oxidation was performed in a fixed-bed reactor made of quartz tube at atmospheric pressure. For the measurement of CO light-off curves showing CO_2 conversion as a function of reaction temperature, approximately 20 mg of the catalysts were loaded into the reactor which was supported by a ball of quartz wool. A feed gas of approximately 1% CO balanced with dry air was passed through the catalysts bed at a flow rate of ~10.0 mL/min which corresponds to a gas hourly space velocity (GHSV) of 30,000 mL $(h\ g_{cat})^{-1}$. The concentrations of CO_2 and CO in the reactor effluent were analyzed by Buck Scientific 910 gas chromatograph (GC) equipped with a thermal conductivity detector (TCD).

3.7 Results and discussion

The XRD patterns of the as-synthesized nanocrystals were obtained to gain some crystallographic information on the structure. The diffraction patterns of HEPO-5, HEPO-7, and Ru/HEPO-7 (figure 3.2) synthesized under 10 min of ultrasonic exposure have perovskite peaks that very closely adopt a perfect cubic crystal structure of $BaZrO_3$ (JCPDS 06-0399) in the *Pm3m* space group. Similar to

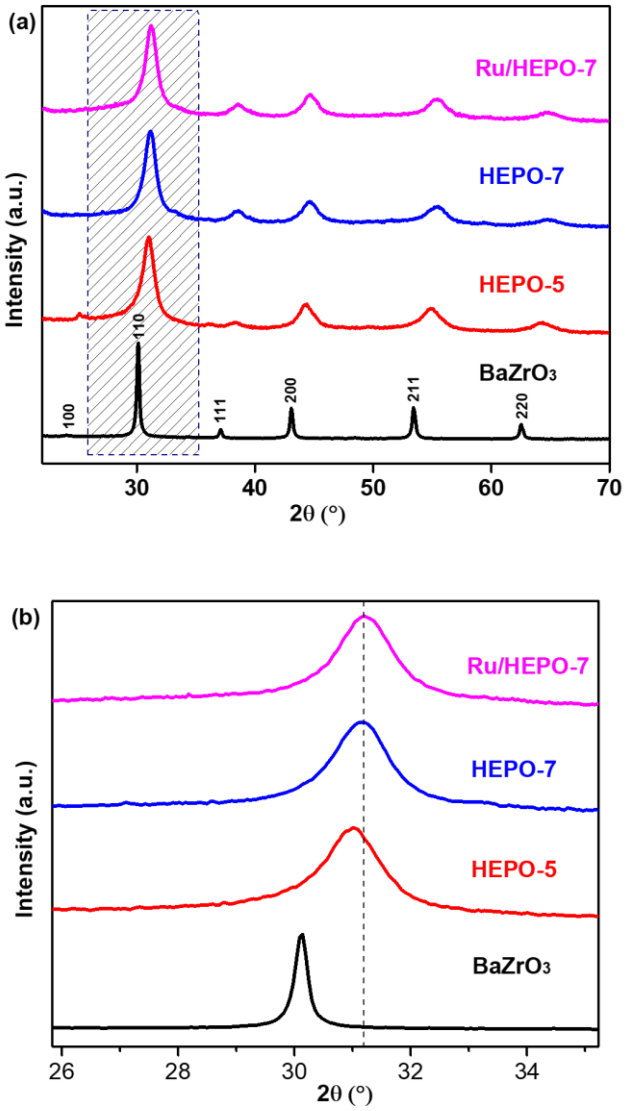

Figure 3.2. (a) XRD patterns of $BaZrO_3$, HEPO-5, HEPO-7, and Ru/HEPO-7. The shift in reflection position of HEPO-5, HEPO-7, and Ru/HEPO-7 relative to conventional perovskite ($BaZrO_3$) is denoted by a dashed line in (b).

$BaZrO_3$, the nanocrystals of HEPO-5, HEPO-7, and Ru/HEPO-7 are also characterized by well-resolved peaks with the most intense peak located around 30.5°, which indicates that the crystals are also preferentially oriented along the (1 1 0) plane. The X-ray reflections of the HEPO-NP are broad owing to small crystallite size and were estimated using Scherrer's equation[21] to be approximately 5.9 nm. Conceptually, the as-synthesized HEPO-NPs could be likened to high-entropy analogs of $BaZrO_3$, wherein configuration disorder was introduced into the crystal structure by partial substitution of barium and zirconium in their respective sublattices with different metallic elements. The characteristic reflections were slightly shifted towards higher 2θ angles as seen in figure 3.2 (b) which clearly indicates that the participating dopants have, indeed, diffused into their respective host lattices and altered the lattice constants. The absence of any secondary diffraction peaks detectable by XRD strongly suggests that the as-synthesized nanoparticles were predominantly crystallized as a single-phase perovskite structure. The entropy-driven stability of Ru/HEPO-7 nanocrystals, in particular, was investigated by studying its crystalline transition behavior at low calcination temperature. Previous studies have demonstrated that a single-phase entropy-stabilized structure segregates into multiple phases at low temperature ($\Delta H > T\Delta S$), but re-combines to form a single-phase structure at high temperature ($T\Delta S > \Delta H$).[22] To this end, the as-synthesized single-phase nanocrystals of Ru/HEPO-7 was calcined at 750 °C for 2 hours and the XRD pattern was closely analyzed. The emergence of some unidentified secondary diffraction peaks, as seen in figure 3.3,

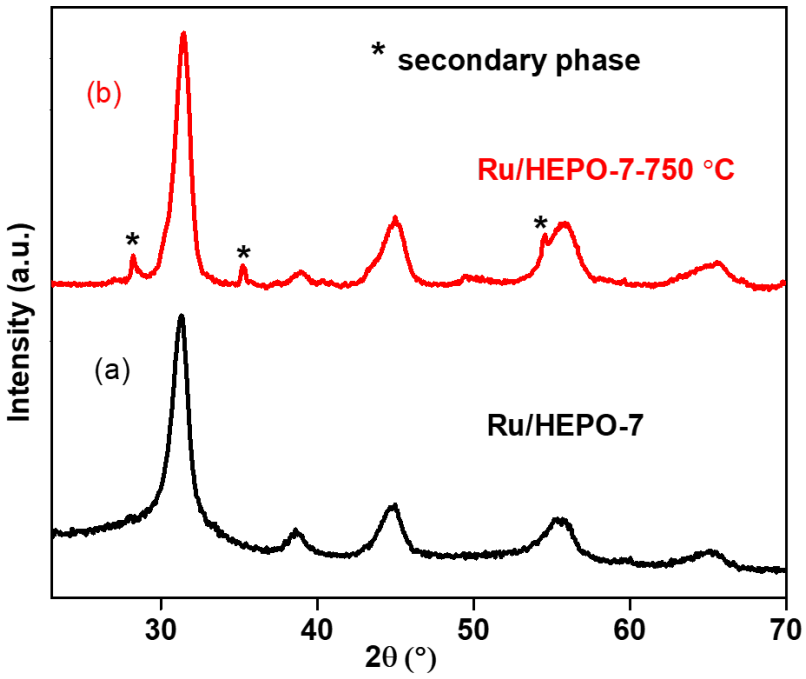

Figure 3.3. XRD patterns of high-entropy perovskite oxide nanocrystals synthesized through ultrasonication-based method (a) without calcination and (b) calcined in air at 750 °C for 2 hours**.**

provides clear evidence that entropy indeed, played a major role in the stabilization of the chemically complex structure of $Ru_{0.13}/Ba_{0.3}Sr_{0.3}Bi_{0.4}(Zr_{0.2}Hf_{0.2}Ti_{0.2}Fe_{0.27})O_3$.

Figure 3.4 and figure 3.5 display the particle morphologies and elemental distributions of the as-prepared HEPO-5 materials. It is evident from the STEM images that the samples mainly consist of monodispersed spherical nanoparticles with an average diameter of 76 ± 1.7 nm. The particle size range is broad which may have resulted from inhomogeneous distributions of the metal precursors during the sonication process. There is some degree of aggregation in the sample, which is consistent with other observations for these types of systems.[23,24] The energy-dispersive X-ray spectroscopy (EDS) spectrum in figure 3.6 shows that the HEPO-5 nanosphere is composed of elements of Ba, Sr, Zr, Hf, and Ti, as expected. The elemental distribution of HEPO-5 clearly indicates that all five metals are present in all nanoparticles as no particular element is preferentially located in any given particle. To clarify the homogeneity of HEPO-5 in the nanosphere, the EDS maps of other areas of the sample were acquired (figure 3.7) as all results indicate that the NPs of HEPO-5 are chemically and structurally homogenous. Figure 3.8 and figure 3.9 show the elemental distributions of Ru/HEPO-7; the results are quite similar to those in figure 3.4 and figure 3.5 all metals are uniformly distributed within the nanosphere. We can conclude from this evidence that a sonochemical-based method is indeed a feasible and universal way of synthesizing HEPO-NPs without calcination.

Nitrogen physisorption measurement was used to examine the surface area of the as-synthesized HEPO-NPs. As seen in figure 3.10, the nanoparticles of

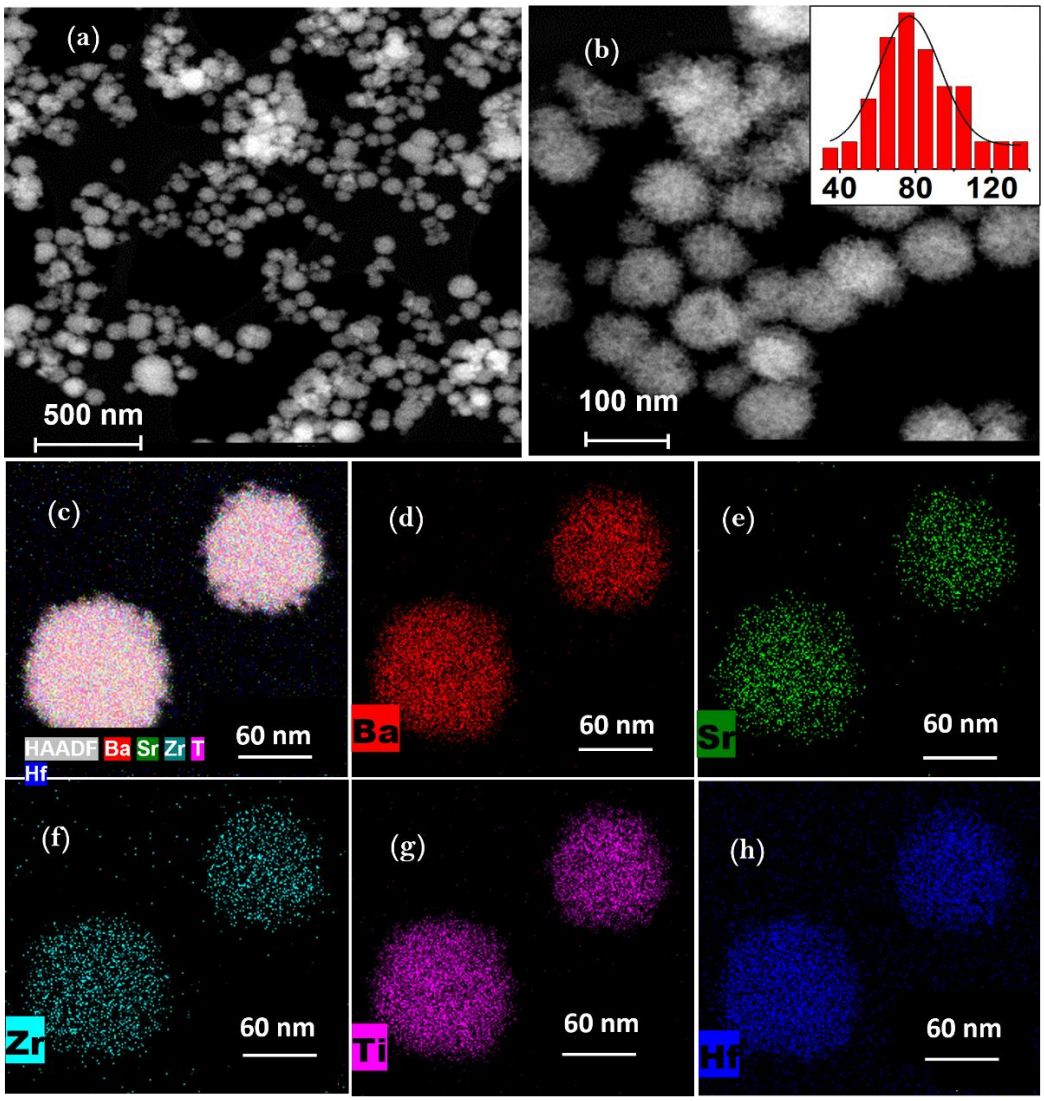

Figure 3.4. STEM image of HEPO-5 showing monodispersed spherical nanoparticles at (a) low resolution and (b) higher resolution. High-angle annular dark-field (HAADF) image and EDS elemental maps of (c) mixed, (d) Ba, (e) Sr, (f) Zr, (g) Ti, and (h) Hf for HEPO-5.

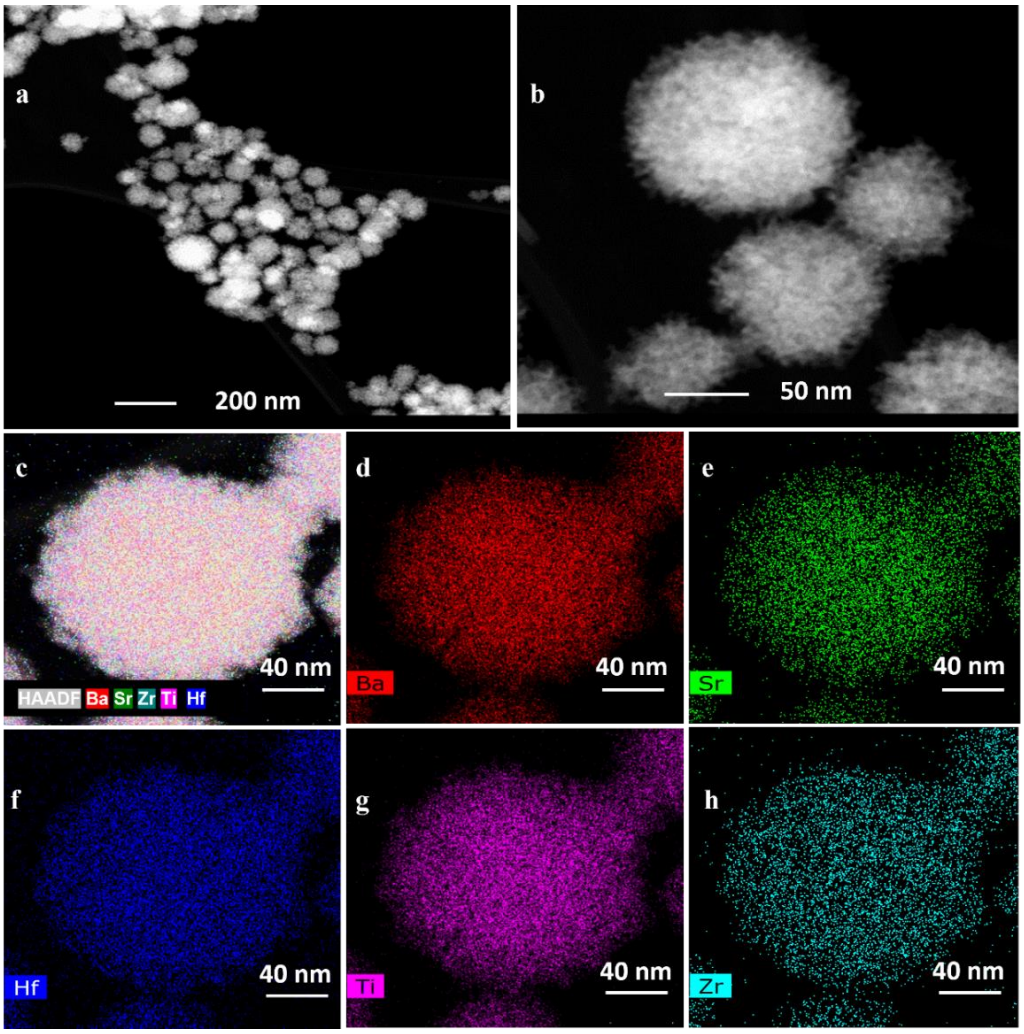

Figure 3.5. STEM image of a different area of HEPO-5 showing monodispersed spherical nanoparticles at (a) low resolution and (b) higher resolution. High-angle annular dark-field (HAADF) image and EDS elemental maps of (c) mixed, (d) Ba, (e) Sr, (f) Hf, (g) Ti, and (h) Zr for HEPO-5.

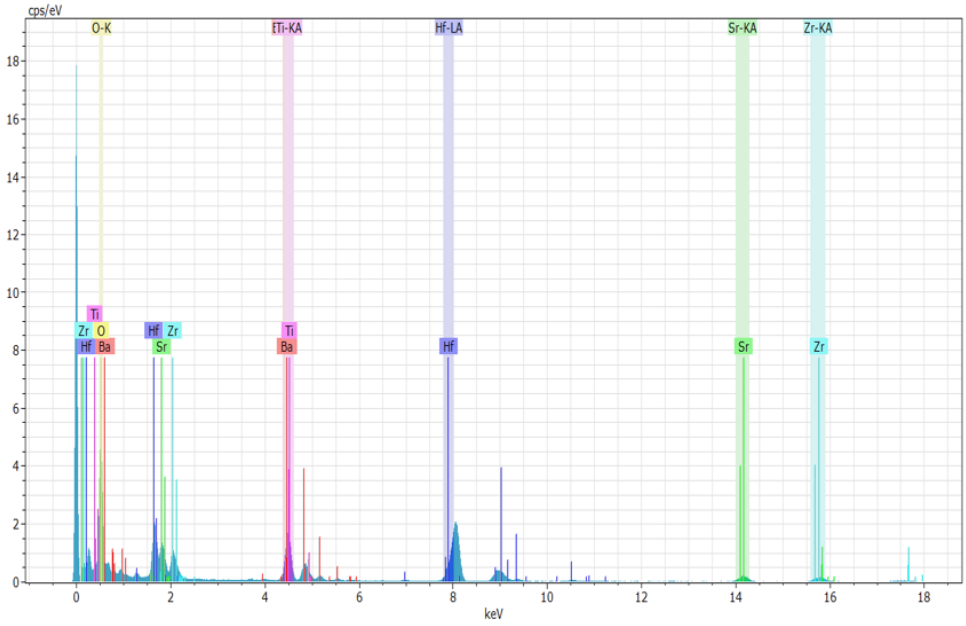

Figure 3.6. EDS analysis of HEPO-5 synthesized under 10 minutes ultrasonication exposure without calcination.

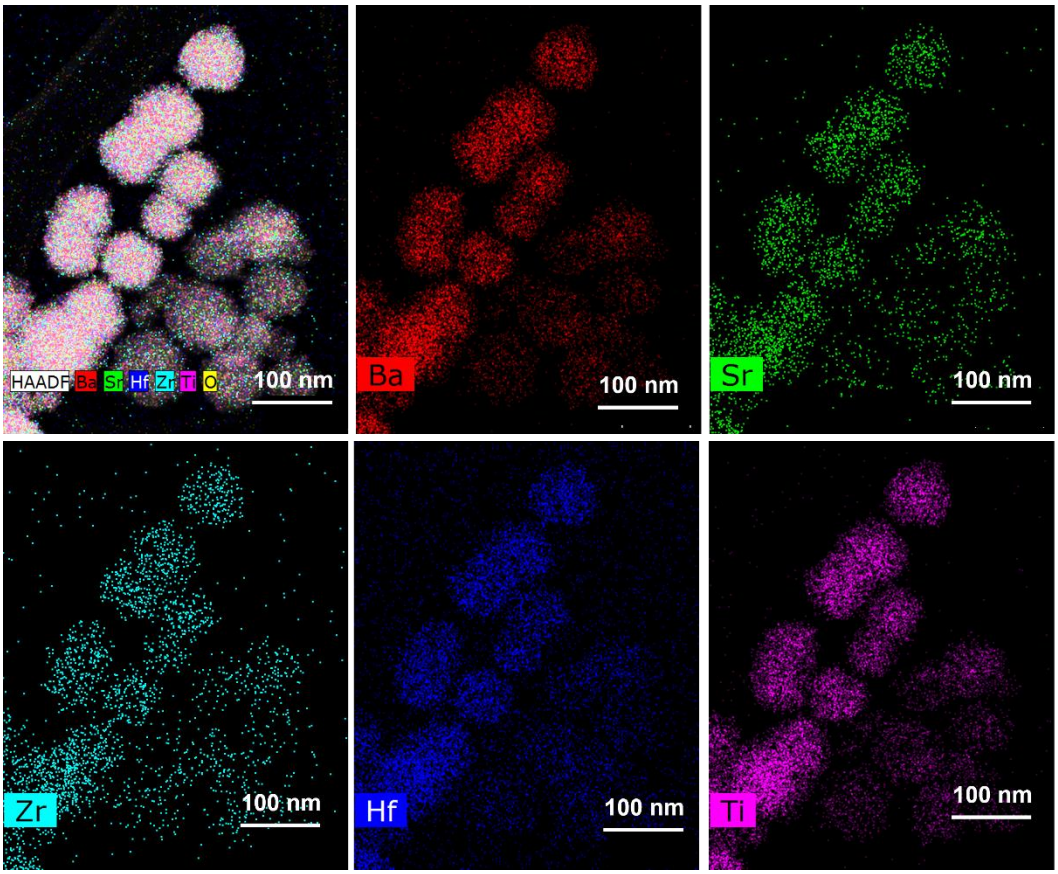

Figure 3.7. HAADF image and EDS elemental maps of HEPO-5 synthesized via ultrasonication-based method without calcination.

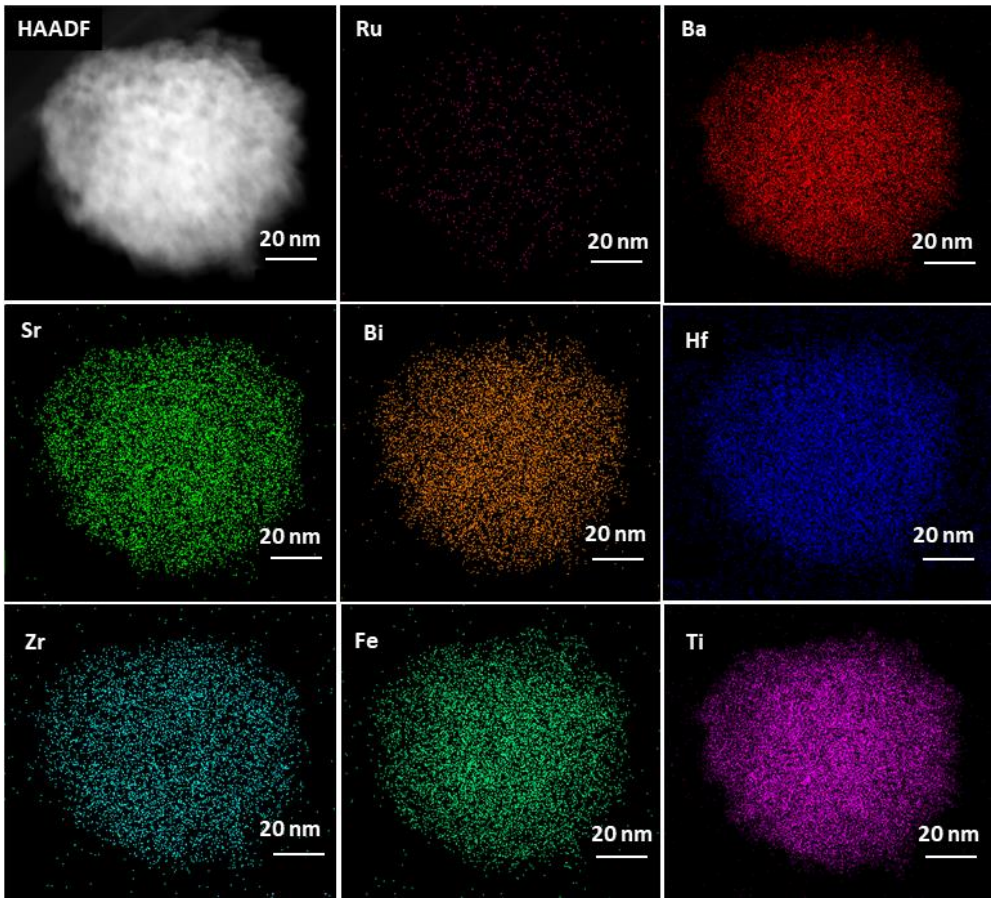

Figure 3.8. EDS elemental maps of Ru/BaSrBi(ZrHfTiFe)O_3 - Ru/HEPO-7 synthesized through the ultrasonication-based method without calcination.

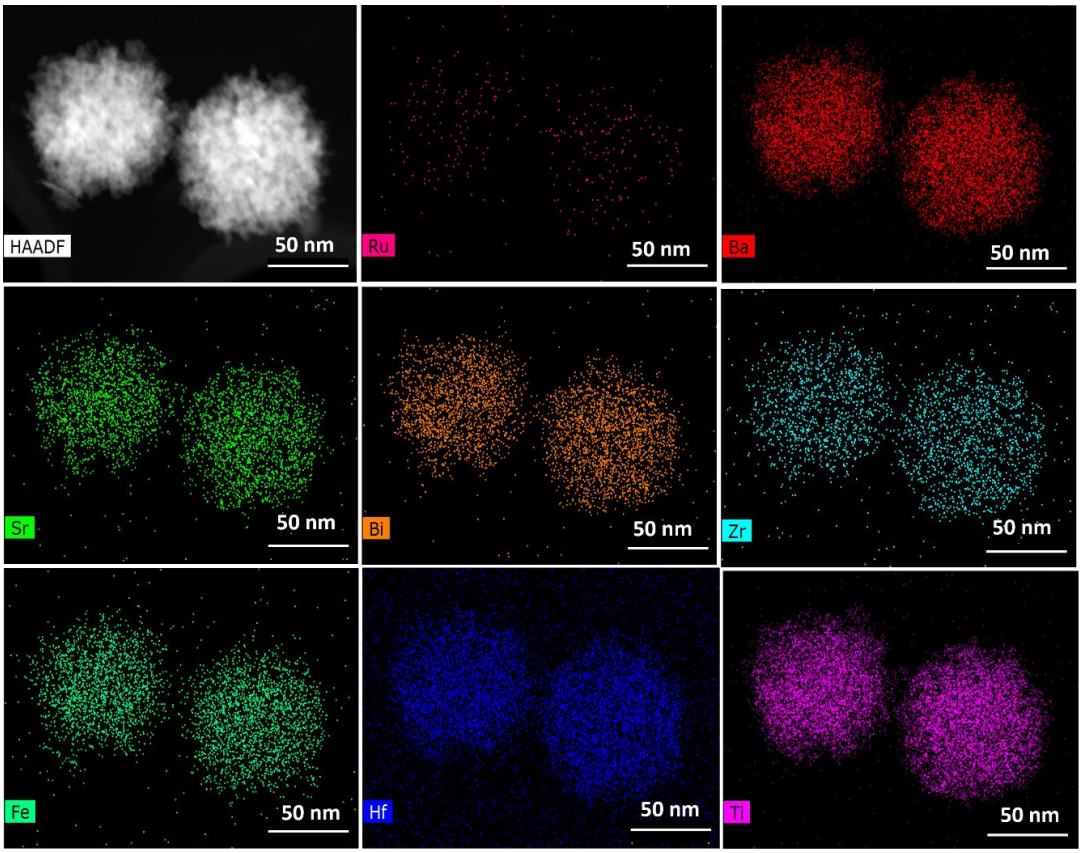

Figure 3.9. EDS elemental maps of a different area of Ru/BaSrBi(ZrHfTiFe)O_3 - Ru/HEPO-7.

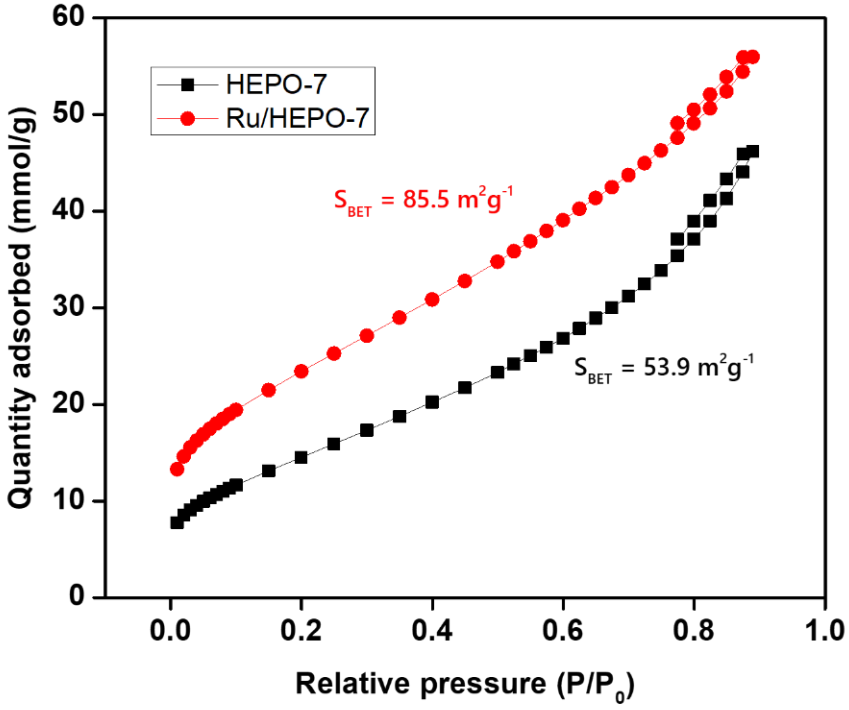

Figure 3.10. N_2 adsorption-desorption isotherms of the as-synthesized high-entropy perovskite oxide nanoparticles.

Ru/HEPO-7 and HEPO-7 both exhibit the type IV adsorption isotherm with hysteresis loops. A high Brunauer–Emmett–Teller (BET) specific surface area of 85.5 $m^2 g^{-1}$ and 53.9 $m^2 g^{-1}$ respectively were obtained. The difference in the BET surface area is possibly due to more restructuring and growth of the crystalline phase that occurred in HEPO-7 during ultrasonic exposure since HEPO-7 has one less chemical element than Ru/HEPO-7 for the maximization of the high-entropy phase.

A direct comparison of the catalytic activity of the Ru/HEPO-7 and the conventional perovskite counterpart - $BaRuO_3$ (also synthesized through the ultrasonication method), was made via CO oxidation. Catalytic oxidation of CO is an extremely important reaction in the depollution process for the removal of toxic CO from the environment. The oxidation was performed in a fixed-bed reactor at ambient pressure with the ruthenium metal functioning as the main active site of the catalysts. For the measurement of CO light-off curves showing CO_2 conversion as a function of reaction temperature, approximately 20 mg of the catalysts were loaded into the reactor which was supported by quartz wool. A feed gas of approximately 1% CO balanced with dry air was passed through the catalyst's bed at a constant flow rate. The concentration of CO_2 and CO in the reactor effluent was determined by gas chromatography (GC) equipped with a thermal conductivity detector (TCD). As seen in figure 3.11**,** within a retention reaction time of less than 1 second, 51% CO conversion was reached at 90 °C for the Ru/HEPO-NP-7 catalyst with just 0.2 wt.% Ru. $BaRuO_3$, in contrast, contains significantly more wt.% Ru (53 wt.% Ru) and attained 50% CO conversion at approximately 255 °C.

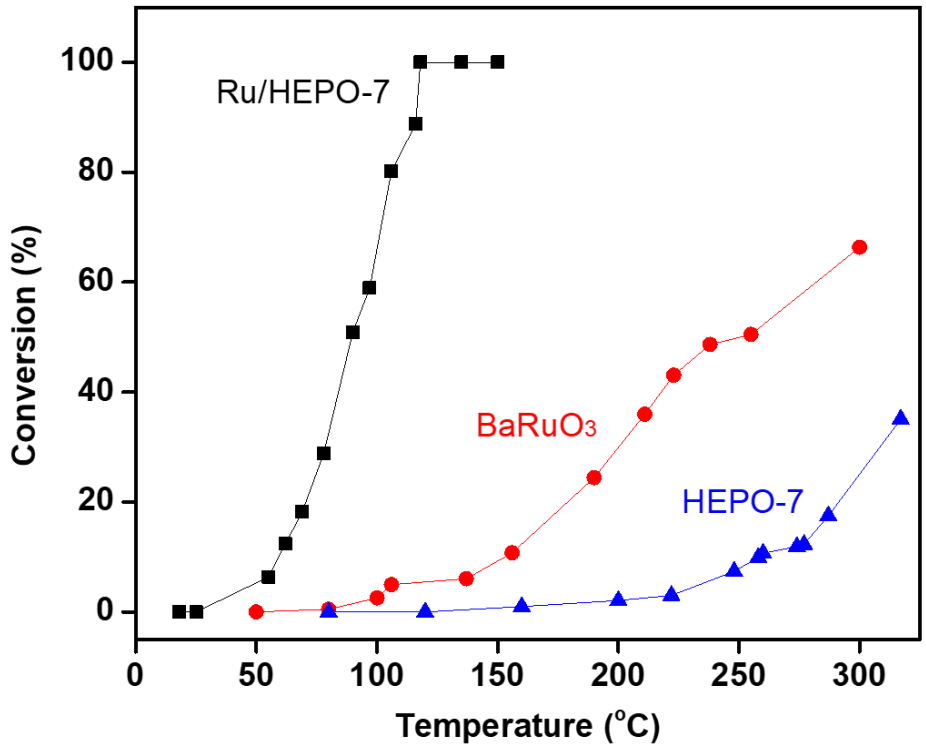

Figure 3.11. Light-off curves of CO conversion over Ru/HEPO-7, HEPO-7, and $BaRuO_3$ catalysts synthesized through the ultrasonication-based method.

In a similar trend, 100% conversion was achieved by the Ru/HEPO-NP-7 catalyst at 118 °C, whereas $BaRuO_3$ catalysts could not achieve a complete CO conversion even at a much higher temperature of 300 °C. The synthesized HEPO-NPs with 0 wt.% Ru showed no appreciable activity at temperatures below 250 °C. The superior catalytic activity exhibited by the Ru/HEPO-NP-7 catalyst over the conventional perovskite counterparts ($BaRuO_3$) can be ascribed to the excellent dispersion of Ru (figure 3.8 and figure 3.9) site in the high-entropy phase.

In contrast to the traditional solid-state reaction and solution-mediated processes commonly used for the synthesis of perovskite-type oxide, this present study utilizes cavitation phenomenon from high-intensity ultrasound irradiations to synthesize entropy-maximized perovskite-oxide NPs with high-surface-area at seemingly room-temperature condition. The extremely localized, massive energy released during the cavitation phenomenon was sufficient to activate reactant molecules, accelerate reactions and crystallize products without external heat treatment. This technologically feasible and facile synthetic approach holds great promises for the development of other classes of HEMs. The entropically-induced stability of Ru/HEPO-7 with excellent dispersion of Ru in the perovskite phase bestowed the NPs with good catalytic activity.

3.8 Acknowledgments

This work was supported by the Division of Chemical Sciences, Geosciences, and Biosciences, Office of Basic Energy Sciences, US Department of Energy.

REFERENCES

[1] Rost, C. M.; Sachet, E.; Borman, T.; Moballegh, A.; Dickey, E. C.; Hou, D.; Jones, J. L.; Curtarolo, S.; Maria, J.-P. Entropy-stabilized oxides. *Nature Communications* **2015,** *6*, 8485.

[2] Liu, M.; Zhang, Z.; Okejiri, F.; Yang, S.; Zhou, S.; Dai, S. Entropy-maximized synthesis of multimetallic nanoparticle catalysts via a ultrasonication-assisted wet chemistry method under ambient conditions. *Advanced Materials Interfaces* **2019,** *6*, 1900015.

[3] Miracle, D. B.; Senkov, O. N. A critical review of high entropy alloys and related concepts. *Acta Mater.* **2017,** *122*, 448-511.

[4] Yeh, J.-W.; Lin, S.-J. Breakthrough applications of high-entropy materials. *J. Mater. Res.* **2018,** *33*, 3129-3137.

[5] Cantor, B.; Chang, I.; Knight, P.; Vincent, A. J. B. *Microstructural development in equiatomic multicomponent alloys*. 2004.

[6] Yeh, J.-W.; Lin, S.-J.; Chin, T.-S.; Gan, J.-Y.; Chen, S.-K.; Shun, T.-T.; Tsau, C.-H.; Chou, S.-Y. Formation of simple crystal structures in cu-co-ni-cr-al-fe-ti-v alloys with multiprincipal metallic elements. *Metallurgical and Materials Transactions A* **2004,** *35*, 2533-2536.

[7] Fu, Z.; Jiang, L.; Wardini, J. L.; MacDonald, B. E.; Wen, H.; Xiong, W.; Zhang, D.; Zhou, Y.; Rupert, T. J.; Chen, W. et al. A high-entropy alloy with hierarchical nanoprecipitates and ultrahigh strength. *Science Advances* **2018,** *4*, eaat8712.

[8] Tsai, C.-W.; Lai, S.-W.; Cheng, K.-H.; Tsai, M.-H.; Davison, A.; Tsau, C.-H.; Yeh, J.-W. Strong amorphization of high-entropy albcrsiti nitride film. *Thin Solid Films* **2012,** *520*, 2613-2618.

[9] Jin, T.; Sang, X.; R. Unocic, R.; Kinch, R.; Liu, X.; Hu, J.; Liu, H.; Dai, S. *Mechanochemical-assisted synthesis of high-entropy metal nitride via a soft urea strategy*. 2018.

[10] Chen, H.; Fu, J.; Zhang, P.; Peng, H.; Abney, C. W.; Jie, K.; Liu, X.; Chi, M.; Dai, S. Entropy-stabilized metal oxide solid solutions as co oxidation catalysts with high-temperature stability. *Journal of Materials Chemistry A* **2018,** *6*, 11129-11133.

[11] Jaing, S.; Hu, T.; Gild, J.; Zhou, N.; Nie, J.; Qin, M.; Harrington, T.; Vecchio, K.; Luo, J. *A new class of high-entropy perovskite oxides*. 2018.

[12] Amonpattaratkit, P.; Ananta, S. Effects of calcination temperature on phase formation and particle size of zn2nb34o87 powder synthesized by solid-state reaction. *Mater. Chem. Phys.* **2013,** *139*, 478-482.

[13] Zhang, Z.; Yang, Q.; Chen, H.; Chen, K.; Lu, X.; Ouyang, P.; Fu, J.; Chen, J. G. In situ hydrogenation and decarboxylation of oleic acid into heptadecane over a cu–ni alloy catalyst using methanol as a hydrogen carrier. *Green Chem.* **2018,** *20*, 197-205.

[14] Wu, Q.; Yan, B.; Cen, J.; Timoshenko, J.; Zakharov, D. N.; Chen, X.; Xin, H. L.; Yao, S.; Parise, J. B.; Frenkel, A. I. et al. Growth of nanoparticles with desired catalytic functions by controlled doping-segregation of metal in oxide. *Chem. Mater.* **2018,** *30*, 1585-1592.

[15] Tian, C.; Zhu, X.; Abney, C. W.; Liu, X.; Foo, G. S.; Wu, Z.; Li, M.; Meyer,

H. M.; Brown, S.; Mahurin, S. M. et al. Toward the design of a hierarchical perovskite support: Ultra-sintering-resistant gold nanocatalysts for co oxidation. *ACS Catal.* **2017,** *7*, 3388-3393.

[16] Adler, S. B. Mechanism and kinetics of oxygen reduction on porous la1−xsrxcoo3−δ electrodes. *Solid State Ionics* **1998,** *111*, 125-134.

[17] Gallagher, P. K.; Johnson, D. W.; Vogel, E. M.; Schrey, F. Effects of the pt content of la0.7pb0.3mno3 on its catalytic activity for the oxidation of co in the presence of so2. *Mater. Res. Bull.* **1975,** *10*, 623-627.

[18] Rossetti, I.; Buchneva, O.; Biffi, C.; Rizza, R. *Effect of sulphur poisoning on perovskite catalysts prepared by flame-pyrolysis*. 2009.

[19] Wang, W.; Qu, J.; Zhao, B.; Yang, G.; Shao, Z. Core–shell structured li0.33la0.56tio3 perovskite as a highly efficient and sulfur-tolerant anode for solid-oxide fuel cells. *Journal of Materials Chemistry A* **2015,** *3*, 8545-8551.

[20] Gedanken, A. Using sonochemistry for the fabrication of nanomaterials. *Ultrason. Sonochem.* **2004,** *11*, 47-55.

[21] Patterson, A. L. The scherrer formula for x-ray particle size determination. *Physical Review* **1939,** *56*, 978-982.

[22] Sarkar, A.; Djenadic, R.; Usharani, N. J.; Sanghvi, K. P.; Chakravadhanula, V. S. K.; Gandhi, A. S.; Hahn, H.; Bhattacharya, S. S. Nanocrystalline multicomponent entropy stabilised transition metal oxides. *J. Eur. Ceram. Soc.* **2017,** *37*, 747-754.

[23] Zhou, H.; Mao, Y.; Wong, S. S. Shape control and spectroscopy of crystalline bazro3 perovskite particles. *J. Mater. Chem.* **2007,** *17*, 1707-1713.

[24] Mao, Y.; Wong, S. S. *Composition and shape control of crystalline ca1-xsrxtio3 perovskite nanoparticles*. 2005.

CHAPTER 4: ULTRASOUND-DRIVEN FABRICATION OF HIGH-ENTROPY ALLOY NANOCATALYSTS PROMOTED BY ALCOHOLIC IONIC LIQUIDS

4.1 Publication disclosure

This chapter is based on a previously published article referenced below: Okejiri, F.; Yang, Z.; Chen, H.; Do-Thanh, C.-L.; Wang, T.; Yang, S.; Dai, S. Ultrasound-driven fabrication of high-entropy alloy nanocatalysts promoted by alcoholic ionic liquids. *Nano Research* **2021**.

My contributions to this work include identification of the research objectives, searching of relevant literature, design and conducting of the synthetic experiments, characterization of the samples except for the electron microscopy, which was conducted by Shize Yang, drafting of the manuscript with reviews and edits from all listed authors.

4.2 Abstract

High-entropy alloy nanoparticles (HEA-NPs) are highly underutilized in heterogeneous catalysis due to the absence of a reliable, sustainable, and facile synthetic method. Herein, we report a facile synthesis of HEA nanocatalysts realized via an ultrasound-driven wet chemistry method promoted by alcoholic ionic liquids (AILs). Owing to the intrinsic reducing ability of the hydroxyl group, AILs were synthesized and utilized as environmentally friendly alternatives to conventional reducing agents and volatile organic solvents in the synthetic

process. Under high-intensity ultrasound irradiation, Au^{3+}, Pd^{2+}, Pt^{2+}, Rh^{3+}, and Ru^{3+} ions were co-reduced and transformed into single-phase HEA (AuPdPtRhRu) nanocrystals without calcination. Characterization results revealed that the as-synthesized nanocrystals are composed of elements of Au, Pd, Pt, Rh, and Ru as expected. Compared to the unary, binary, ternary, and quaternary counterparts, the carbon-supported HEA nanocatalysts showed superior catalytic performance for selective hydrogenation of phenol to cyclohexanone in terms of yield and selectivity. Our synthetic strategy provides an improved and facile methodology for the sustainable synthesis of multicomponent alloys for catalysis and other applications.

4.3 Introduction

High-entropy alloys (HEAs) are a unique class of materials with great technological prospects. Unlike traditional alloys, which do not exceed three elements, HEAs are based on the premise of integrating near-equimolar concentrations of five or more elements to form a single-phase solid solution.[1,2] Nanosized HEAs are highly underutilized in heterogeneous catalysis due to the absence of a reliable, sustainable, and facile synthetic method and may constitute a whole new paradigm in catalysis.[3–8] There has been a growing interest in the development of simple processes to fabricate HEA nanocatalysts for thermally-driven and electrocatalytic reactions.[2,9–21] Hu and coworkers have reported a carbothermal shock method in which metal salt precursors loaded onto carbon-nanofibers were thermally shocked to obtain HEA-nanoparticle (NP) catalysts.[9]

However, this synthetic strategy is limited to the production of NPs immobilized on conductive oxygenated carbon supports. Immobilization of ultrasmall-sized HEA-NPs on granular supports has been realized by the fast-moving bed pyrolysis method following wet impregnation.[22] The drawback to this fabrication strategy is that it is technologically demanding and requires highly specialized equipment to rapidly raise the temperature of the mixed metal precursors to 923 K in less than 5 s. Nanoporous HEAs with enhanced surface area and uniform pore structure have been synthesized via the dealloying method.[23,24] While the scalability of this remarkable strategy is highly promising, the inevitable microstructural coarsening resulting from the high-temperature treatment (> 1,123 K) degrades the functionality of the materials over time. Also, HEA-NP-graphene composite has been synthesized by mechanical alloying of the pure metal powders with graphite, followed by sonication-based exfoliation.[25] The distribution in the composition between the NPs is unsuitably large.[25] More recently, Chen et al. synthesized monodispersed HEA-NPs by converting a two-phase core@shell NPs to single-phase HEA-NPs via annealing.[10] Other promising strategies that have been reported include sputtering deposition,[26] kinetically controlled laser synthesis,[16] and solvothermal syntheses,[27] being limited by the ultrahigh vacuum requirement, restrictive element applicability, and low productivity, respectively.

Studies have shown that liquids irradiated with high-intensity ultrasound generate acoustic cavitation, which drives bubble formation, growth, and implosive collapse in a monetary lifespan while producing enormous heat and pressure in a highly localized region (hotspot).[28] This transient localized hotspot with a

temperature above 5,000 K and pressures exceeding 1,000 atm can drive a high-energy chemical reaction and serve as an exceptional route for nanoparticle synthesis.[29,30] Taking advantage of this unique phenomenon, we recently demonstrated the feasibility of fabricating HEA-NPs via an ultrasound-driven wet chemistry method using ethylene glycol (EG) as the reaction medium.[31] Unfortunately, the resultant NPs displayed a two-phase microstructure, requiring further heat treatment at 700 °C under N_2 to be transformed into single-phase HEA nanocrystals. A single-step ultrasound-driven pathway will rely on the design of multifunctional reaction media capable of well dissolving and reducing the metal species while simultaneously stabilizing the as-afforded HEA NPs. Room-temperature ionic liquids (ILs) can be tailored to meet these requirements due to the relative ease at which simple and small alterations can be made to their chemical structure.[32–37]

Rationally, owing to the intrinsic reducing ability of the hydroxyl group, alcoholic ionic liquid (AIL) was fabricated as the desired multifunctional reaction media in the present study. Under high-intensity ultrasound irradiation, Au^{3+}, Pd^{2+}, Pt^{2+}, Rh^{3+}, and Ru^{3+} ions were co-reduced by the AIL and transformed into single-phase HEA (AuPdPtRhRu) nanocrystals, effectively eliminating the need for an external heat-treatment process. Notably, the hydroxyl functionality played a significant role in the formation of single-phase nanocrystals of AuPdPtRhRu in one step. Characterization results revealed that the as-obtained nanocrystals are composed of elements of Au, Pd, Pt, Rh, and Ru as expected. Compared to the unary, binary, ternary, and quaternary counterparts, the carbon-supported HEA-

NP catalysts show superior catalytic performance for selective hydrogenation of phenol to cyclohexanone in terms of yield and selectivity. This synthetic strategy provides an improved and facile methodology for the sustainable synthesis of multicomponent alloys in one step under mild conditions.

4.4 Materials

All the chemical reagents used in this work were of analytical grade. Potassium tetrachloropalladate (II) (K_2PdCl_4), potassium tetrachloroplatinate (II) (K_2PtCl_4), ruthenium chloride ($RuCl_3$), gold chloride hydrate ($HAuCl_4 \cdot 3H_2O$), rhodium chloride ($RhCl_3$), ethylene glycol ($HO\text{-}CH_2CH_2\text{-}OH$), acetone ($CH_3\text{-}CO\text{-}CH_3$), cyclohexanone ($(CH_2)_2CO$), commercial Pd/carbon catalyst (Pd weight loading - 10 %), acetonitrile (CH_3CN) were purchased from Fisher Chemicals. N-methylmorpholine ($O(CH_2CH_2)_2NCH_3$), phenol (C_6H_5OH), cyclohexanol ($HOCH(CH_2)5$), 2-bromoethanol ($BrCH_2CH_2OH$), bromoethane ($BrCH_2CH_3$), acetonitrile (CH_3CN), ethyl ether ($(CH_3CH_2)_2O$), and ethyl acetate ($CH_3COOC_2H_5$), were acquired from ACROS ORGANICS. Lithium bis(trifluoromethane)sulfonimide ($LiNTf_2$), sodium tetrafluoroborate ($NaBF_4$), and activated charcoal were purchased from SigmaAldrich. Carbon (Vulcan XC-72R) was bought from the Fuel Cell Store. All the chemicals were used without further purification.

4.5 Synthesis of the ionic liquids

[HEMMor][NTf_2]

N-(2-Hydroxyethyl)-N-methylmorpholinium bis(trifluoromethylsulfonyl) imide) abbreviated as [HEMMor][NTf_2] was synthesized according to previous

reports with some modifications.[39] N-Methylmorpholine (0.55 mol) and excess 2-bromoethanol (0.60 mol) were mixed with 300 mL acetonitrile in a round-bottom flask and stirred at 90 °C for 12 hours under an N_2 atmosphere. The solvent was removed under reduced pressure, and the residue was washed with ethyl ether to obtain N-(2-hydroxyethyl)-N-methylmorpholinium bromide ([HEMMor][Br]) as a crystalline solid. The solid was redissolved in 300 mL deionized water (DI) and decolorized with activated charcoal by refluxing at 70 °C overnight. The aqueous layer was recovered via vacuum filtration and used for the anionic exchange with lithium bis(trifluoromethylsulfonyl)imide (0.55 mol) at room temperature. The non-aqueous layer was extracted in ethyl acetate and dried under removed pressure to obtain HEMMor][NTf_2] as a clear, viscous liquid. The reaction scheme is shown in figure 4.1 (a).

[HEMMor][BF_4]

N-(2-hydroxyethyl)-N-methylmorpholinium tetrafluoroborate abbreviated as [HEMMor]BF_4] was synthesized according to previous reports with some modifications.[39] N-methylmorpholine (0.55 mol) and excess 2-bromoethanol (0.60 mol) were mixed with 300 mL acetonitrile in a round-bottom flask and stirred at 90 ^oC for 12 hours under an N_2 atmosphere. The solvent was removed under reduced pressure, and the residue was washed with ethyl ether to obtain ethyl-N-methylmorpholinium bromide ([HEMMor][Br]) as a crystalline solid. The solid was redissolved in 300 mL deionized water (DI) and decolorized with activated charcoal by refluxing overnight. The aqueous layer was recovered by vacuum filtration and used for the anionic exchange with $NaBF_4$ (0.55mol) at room temperature.

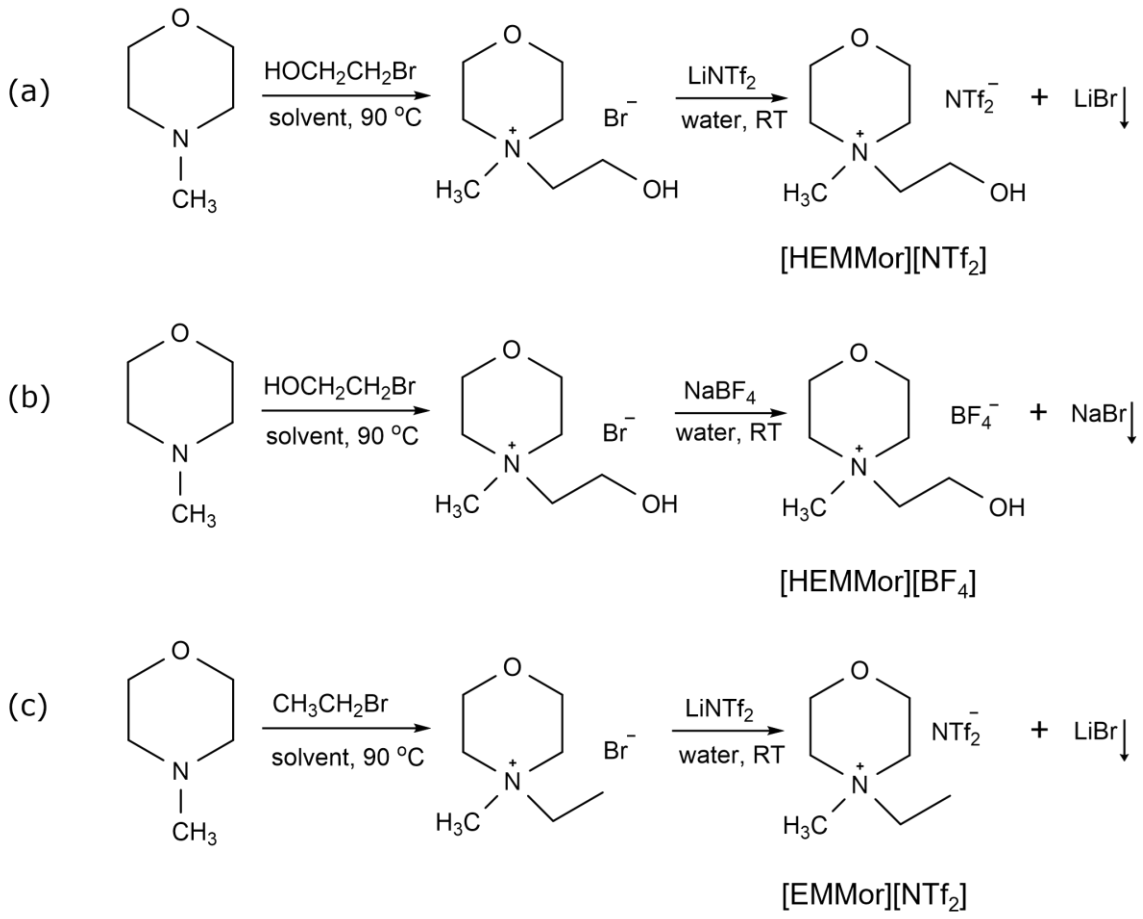

Figure 4.1. Synthesis of the various ionic liquids utilized in this work. (a) [HEMMor][NTf_2], (b) [HEMMor][BF_4] and (c) [EMMor][NTf_2].

The residual of NaBr was removed from the ionic liquid through low-temperature filtration. The reaction scheme is shown in figure 4.1 (b).

[EMMor][NTf_2]

Ethyl-N-methylmorpholinium bis(trifluoromethylsulfonyl)imide abbreviated as [EMMor][NTf_2] was synthesized according to previous reports with some modifications.[39] N-methylmorpholine (0.55 mol) and excess bromoethane (0.60 mol) were mixed with 300 mL acetonitrile in a round-bottom flask and stirred at 90 ^oC for 12 hours under an N_2 atmosphere. The solvent was removed under reduced pressure, and the residue was washed with ethyl ether to obtain ethyl-N-methylmorpholinium bromide ([EMMor][Br]) as a crystalline solid. The solid was redissolved in 300 mL deionized water (DI) and decolorized with activated charcoal by refluxing overnight. The aqueous layer was recovered by vacuum filtration and used for the anionic exchange with $LiNTf_2$ (0.55mol) at room temperature. The non-aqueous layer was extracted in ethyl acetate and dried under removed pressure to obtain [EMMor][NTf_2]. The reaction scheme is shown in figure 4.1 (c).

4.6 Synthesis of the catalysts:

(a.) HEA-NPs/C (AuPdPtRhRh-NPs/C)

An aqueous solution of the metal precursors was made by the dissolution of 0.005 mmol each of $HAuCl_4 \cdot 3H_2O$, K_2PdCl_4, K_2PtCl_4, $RhCl_3$, and $RuCl_3$ in 5 mL DI water. The precursors were combined with a calculated mass of XC-72 carbon support pre-dispersed in a 30 mL IL for a total metallic loading of 10 wt.%. The mixture was exposed to sonication treatment for 10 minutes by direct immersion

of ultrasonic titanic horn operating at 20 kHz at ambient conditions, as shown schematically in figure 4.2. When the sonication time was reached, the solid was recovered by centrifugation and washed thoroughly with DI before being dried in an oven at 100 °C overnight. The unary, binary, ternary, and quaternary counterparts were synthesized in a similar as described below.

(b.) AuPdPtRh-NPs/C

An aqueous solution of the metal precursors was made by the dissolution of 0.00625 mmol each of $HAuCl{\cdot}3H_2O$, K_2PdCl_4, K_2PtCl_4, and $RhCl_3$, in 5 mL DI water. The solution was combined with a calculated mass of XC-72 carbon support pre-dispersed in 30 mL IL for a total metal loading of 10 wt.%. The mixture was exposed to sonication treatment for 10 minutes by direct immersion of ultrasonic titanic horn operating at 20 kHz at ambient conditions. When the sonication time was reached, the solid was recovered by centrifugation and washed thoroughly with DI before being dried in an oven at 100 ^oC overnight.

(c.) AuPdPt-NPs/C

An aqueous solution of the metal precursors was made by the dissolution of 0.00833 mmol each of $HAuCl_4{\cdot}3H_2O$, K_2PdCl_4, and K_2PtCl_4 in 5 mL DI water. The solution was combined with a calculated mass of XC-72 carbon support pre-dispersed in 30 mL IL for a total metal loading of 10 wt.%. The mixture was exposed to sonication treatment for 10 minutes by direct immersion of ultrasonic titanic horn operating at 20 kHz at ambient conditions. When the sonication time was reached, the solid was recovered by centrifugation and washed thoroughly with DI before being dried in an oven at 100 ^oC overnight.

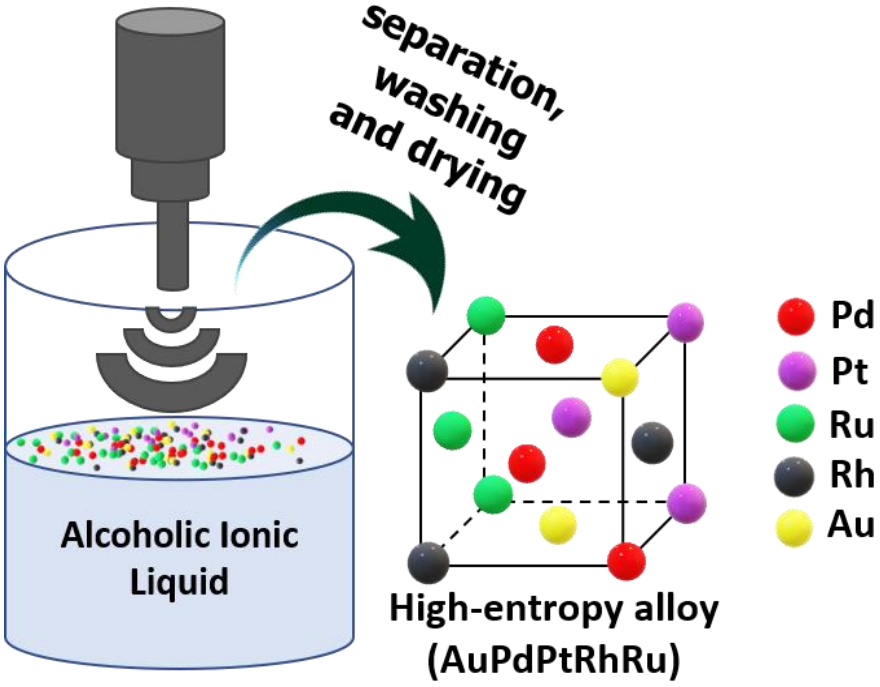

Figure 4.2. Schematic illustration of the synthesis of high-entropy alloy nanocatalysts realized via an ultrasound-driven wet chemistry method promoted by an alcoholic ionic liquid.

(d.) AuPd-NPs/C

An aqueous solution of the metal precursors was made by the dissolution of 0.0125 mmol each of $HAuCl_4 \cdot 3H_2O$ and K_2PdCl_4, in 5 mL DI water. The solution was combined with a calculated mass of XC-72 carbon support pre-dispersed in 30 mL IL for a total metal loading of 10 wt.%. The mixture was exposed to sonication treatment for 10 minutes by direct immersion of ultrasonic titanic horn operating at 20 kHz at ambient conditions. When the sonication time was reached, the solid was recovered by centrifugation and washed thoroughly with DI before being dried in an oven at 100 ^oC overnight.

(e.) Pd-NPs/C

K_2PdCl_4 (0.025 mmol) was dissolved in a minimum volume of DI water to form a salt solution. The solution was combined with a calculated mass of XC-72 carbon support pre-dispersed in 30 mL IL for a total metal loading of 10 wt.%. The mixture was exposed to sonication treatment for 10 minutes by direct immersion of ultrasonic titanic horn operating at 20 kHz at ambient conditions. When the sonication time was reached, the solid was recovered by centrifugation and washed thoroughly with DI before being dried in an oven at 100 ^oC overnight.

(f.) Au-NPs/C

$HAuCl_4 \cdot 3H_2O$ (0.025 mmol) was dissolved in a minimum volume of DI water to form a salt solution. Thi solution was combined with a calculated mass of XC-72 carbon support pre-dispersed in 30 mL IL for a total metal loading of 10 wt.%. The mixture was exposed to sonication treatment for 10 minutes by direct immersion of ultrasonic titanic horn operating at 20 kHz at ambient conditions.

When the sonication time was reached, the solid was recovered by centrifugation and washed thoroughly with DI before being dried in an oven at 100 ^{o}C overnight.

4.7 Characterization of the ionic liquids

^{1}H NMR spectra were recorded on JEOL JNM-ECZS 400 MHz spectrometer using dry DMSO-d_6 as the solvent. The chemical shifts are in ppm. The splitting patterns are represented by the following abbreviations: s (singlet), d (doublet), t (triplet), q (quartet), and m (multiplet).

4.8 Characterization of the catalysts

X-ray diffraction (XRD) patterns were recorded on a PANalytical Empyrean diffractometer with Cu Kα1 radiation (λ = 1.5406 Å), operated at 45 kV and 40 mA. The 2θ range angles were scanned between 20° to 80° at a step size of 0.02°.

High-angle annular darkfield scanning transmission electron microscopy (HAADF-STEM) images and energy-dispersive X-ray (EDS) spectra were collected on FEI Talos F200X microscope operated at 200 keV. The particle size distribution was estimated by randomly measuring more than 200 particles on the images.

The elemental composition was determined by inductively coupled plasma optical emission spectroscopy (ICP-OES) analysis performed on an Agilent 5110 ICP-OES spectrometer. The sample was dissolved in aqua regia and diluted with 2.0% nitric acid prior to analysis.

4.9 Hydrogenation of Phenol

Phenol hydrogenation was performed in a 100 mL stainless steel autoclave equipped with a pressure gauge and a magnetically driven stir bar. In a typical run, 1.3 mmol of phenol, catalyst (2.8 mol% relative to phenol), and 6.0 mL hexane were loaded into the reactor and sealed properly. The residual air was expelled from the reactor by purging with purified hydrogen five times before being pressurized to the desired pressure. The reactor was heated in an oil bath at 150 °C with constant stirring for a predetermined period. At the end of the reaction time, the reactor was cooled to room temperature and depressurized. The catalysts were recovered by centrifugation, and the supernatant liquid was analyzed using a gas chromatograph (Agilent 9790-GC) equipped with a flame ionization detector (FID).

4.10 Results and discussion

First, the ionic liquids were synthesized via a two-step process and characterized by NMR spectroscopy. The following peak positions were observed for the various ionic liquids.

[EMMor][NTf_2]: ^{1}H NMR (400 MHz, DMSO-d_6, δ/ppm, relative to DMSO): δ 1.22 - 1.28 (t, 3H), 3.08 (s, 3H), 3.34 – 3.38 (t, 4H), 3.45 – 3.54 (q, 2H), 3.88 – 3.98 (s, 4H). The NMR spectrum is shown in figure 4.3.

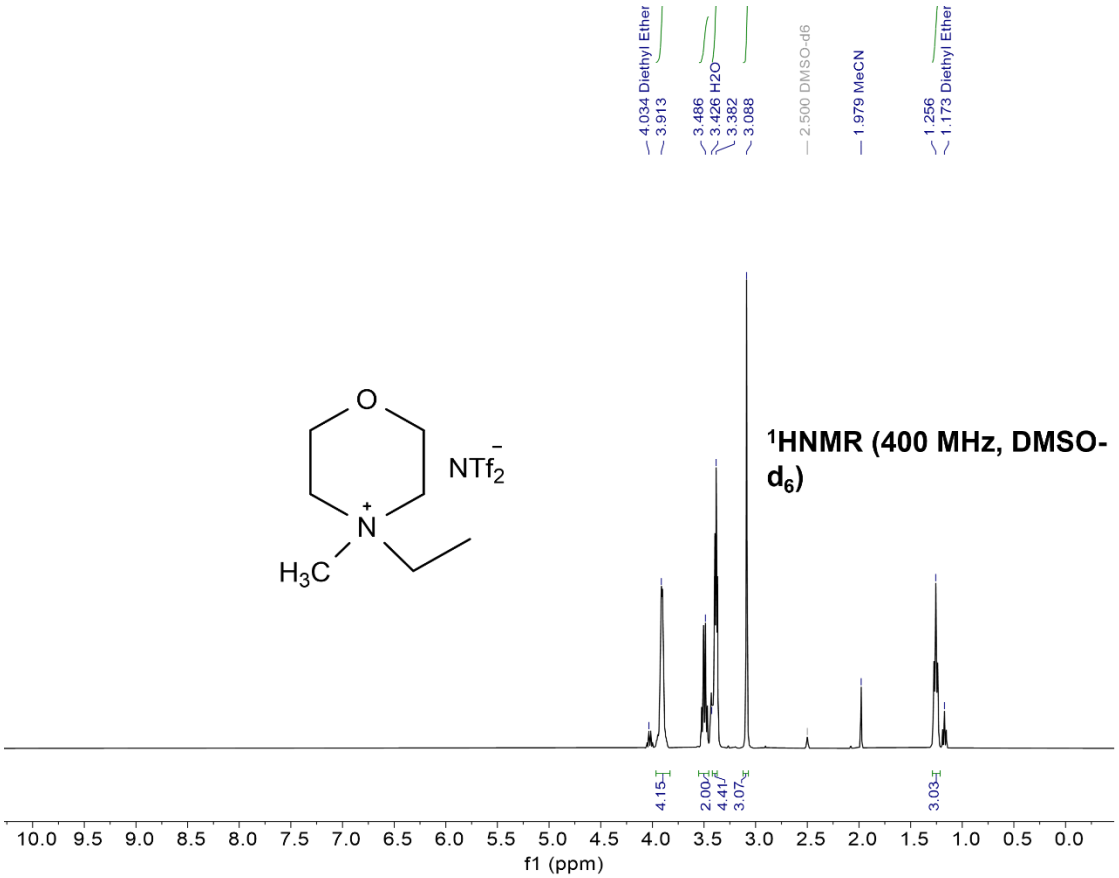

Figure 4.3. NMR spectrum of [EMMor][NTf_2].

[HEMMor][BF_4]: ^{1}H NMR (400 MHz, DMSO-d_6, δ/ppm, relative to DMSO): δ 3.22 (s, 3H), 3.41 – 3.47 (t, 2H), 3.50 – 3.55 (t, 2H), 3.60 – 3.61 (t, 2H), 3.85 (s, 2H), 3.90 (s, 4H), 5.34 (s, 1H). The NMR spectrum is shown in figure 4.4.

[HEMMor][NTf_2]: ^{1}H NMR (400 MHz, DMSO-d_6, δ/ppm, relative to DMSO): δ 3.21 (s, 3H), 3.41 – 3.47 (t, 2H), 3.50 – 3.58 (t, 2H), 3.60 – 3.64 (t, 2H), 3.84 (s, 2H), 3.89 (s, 4H), 5.33 (s, 1H). The NMR spectrum is shown in figure 4.5.

To test the feasibility of fabricating supported HEA nanocatalysts by our ultrasound-driven AIL-promoted strategy, commercial XC-72 carbon support, and the metal salt precursors were dispersed in the ionic liquid and exposed to high-intensity ultrasound irradiation for 10 min. The product was recovered by centrifugation, washed in DI water, and characterized by XRD, scanning transmission electron microscopy (STEM), EDS, and ICP-OES. For simplicity, the as-obtained carbon-supported HEA-NP catalyst is denoted as HEA-NPs/C.

The crystallinity of HEA-NPs/C was determined by the XRD technique and presented in figure 4.6(a). HEA-NPs/C shows four distinct peaks that correspond to the standard Braggs reflections ((111), (200), (220), and (311)) of face-centered cubic (fcc) lattice with a preferential growth along the (111) plane. The shift in characteristic reflection with respect to Au-NPs/C standard, shown in figure 4.6(b), is attributed to the change in lattice parameters. The absence of secondary diffraction peaks suggests that Pt, Pd, Rh, and Ru particles are well incorporated into the Au lattice to form an entropy-stabilized single-phase solid solution.

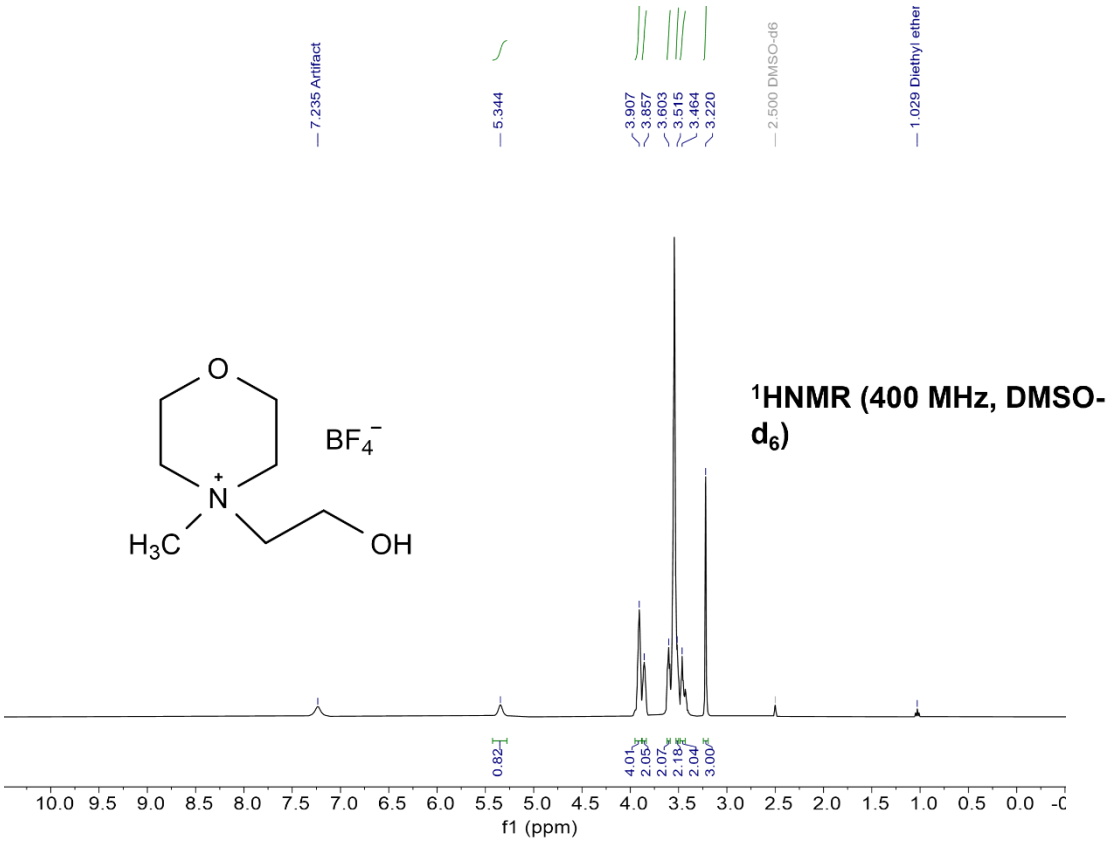

Figure 4.4. NMR spectrum of [HEMMor][BF_4].

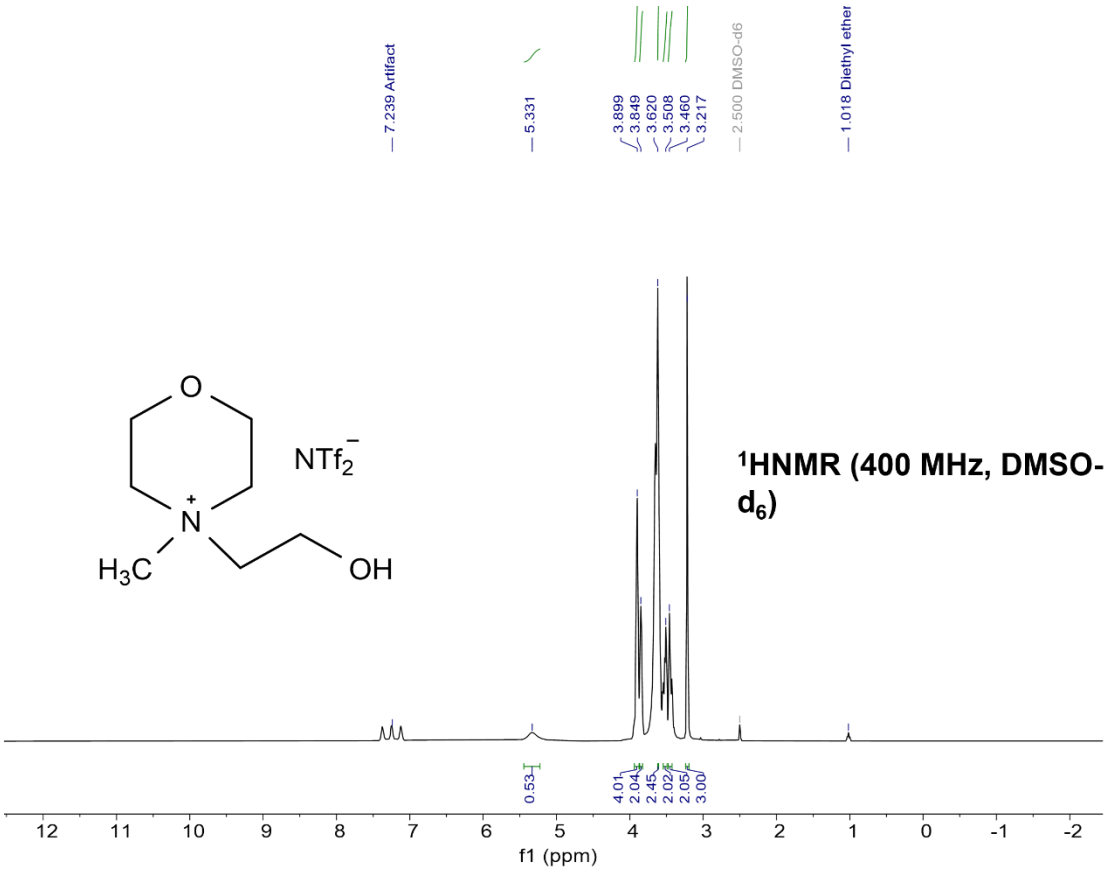

Figure 4.5. NMR spectrum of [HEMMor][NTf_2].

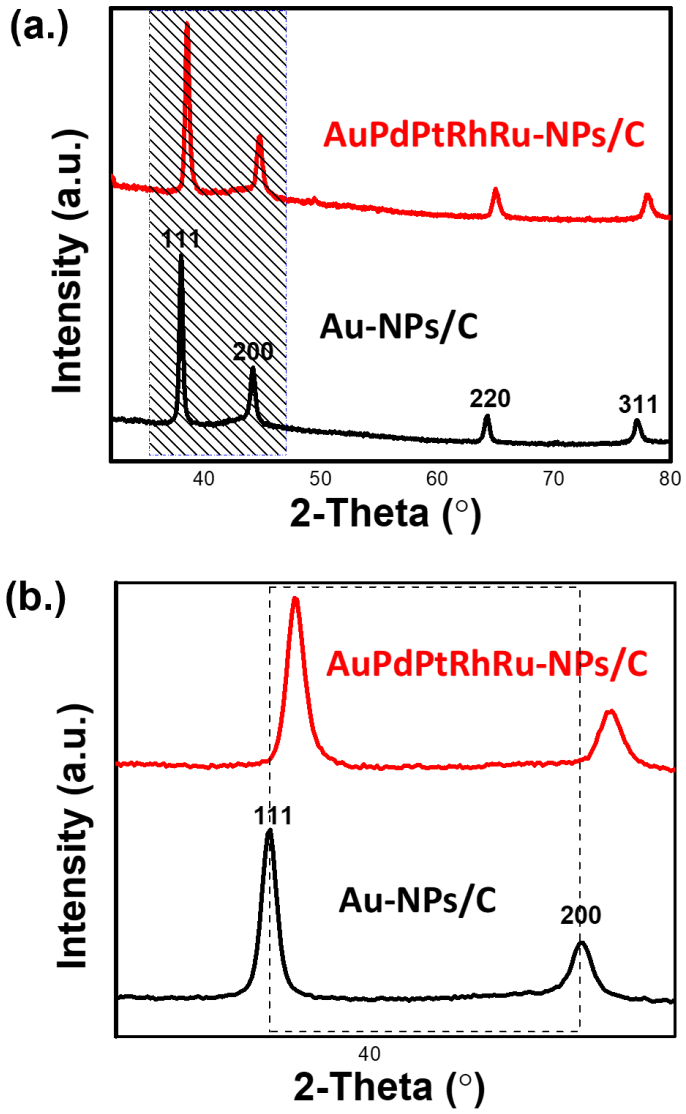

Figure 4.6. (a) XRD patterns of the AuPdPtRhRu-NPs/C and the gold standard (Au-NPs/C). The shift in reflection positions of AuPdPtRhRu-NPs/C relative to Au-NPs/C is denoted by the dotted lines in (b).

The high-resolution (HR)-STEM image in figure 4.7(a) shows lattice fringe spacing of 0.24 nm, which is consistent with the (111) plane of an fcc crystal lattice; the corresponding selected area electron diffraction (SAED) pattern additionally corroborates this. The radial intensity line profile as a function of reciprocal lattice distance extracted from the SAED pattern is presented in fig. 4.7(b).

Figure 4.7(c) and figure 4.7(d) display the STEM image of HEA-NPs/C showing nanocrystalline particles of AuPdPtRhRu dispersed on the XC-72 carbon support. The particle size range is narrow which may have resulted from the controllable growth of NPs induced by the electrostatic and steric properties of the IL. There are, however, quite a few remarkably larger particles that possibly result from inhomogeneous mixing of the precursor ions and their subsequent sintering during the sonication process. Overall, the majority of the particles have diameters in the nanoscale range.

Figure 4.8 shows the STEM-EDS elemental map of HEA-NPs/C. The uniform distribution of Au, Pd, Pt, Rh, and Ru in the nanosphere directly validates the formation of an alloy system. The EDS spectrum in figure 4.9 shows the signal intensities of all five metals, which additionally corroborates this. The EDS elemental map analyses of different areas on the sample were acquired (figure 4.10) to demonstrate the homogeneity of HEA-NPs/C. The results show that HEA-NPs/C is both structurally and chemically homogeneous. The elemental composition of HEA-NPs/C was further determined by the ICP-OES analysis. The atomic percentage of Au, Pd, Pt, Rh, and Ru, are respectively 19.8, 19.0, 20.5, 21.3, and 19.4, which approximates to 1:1:1:1:1 mole ratio used in the starting mat

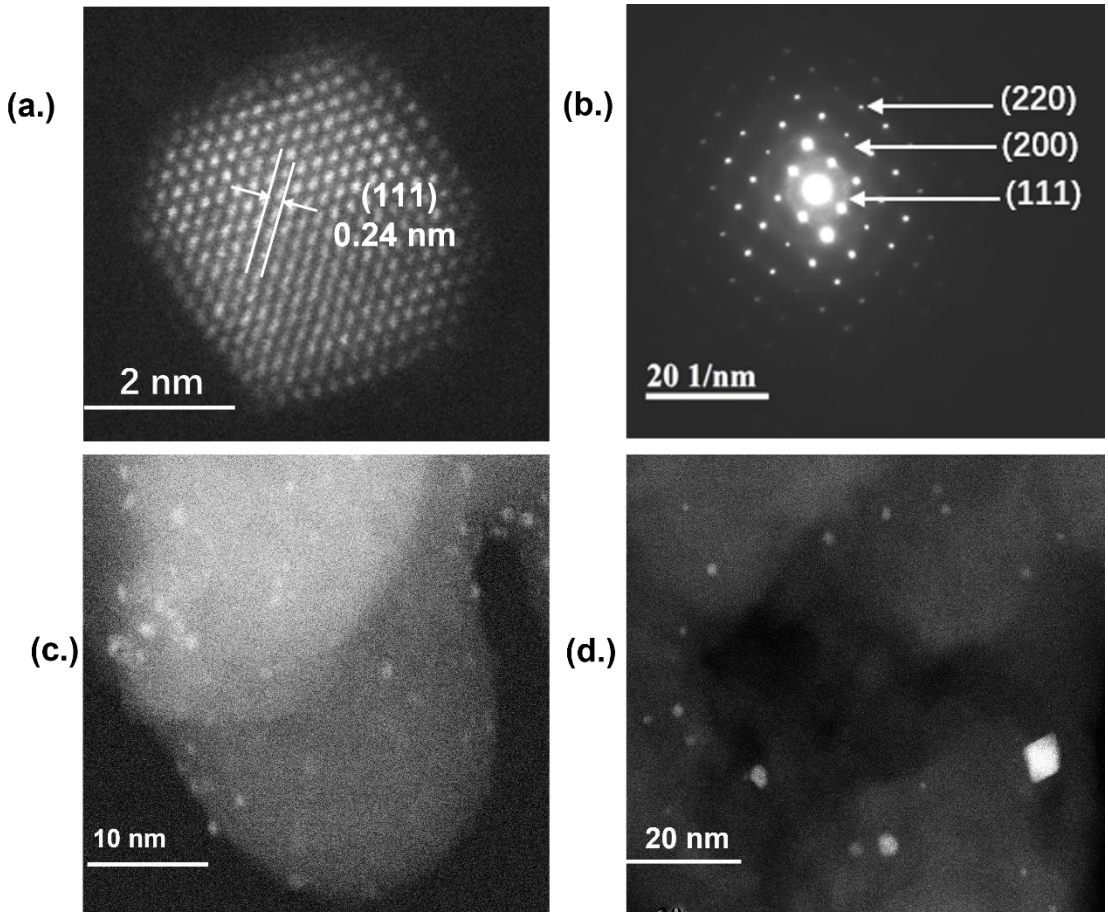

Figure 4.7. (a) HR-STEM image of HEA-NPs/C showing a lattice fringe spacing of 0.24 nm consistent with (111) plane of a face-centered cubic crystal structure. (b) SAED pattern of HEA-NPs/C displaying a Debye-Scherrer ring pattern consistent with a polycrystalline fcc lattice. (c) STEM image of HEA-NPs/C at a higher resolution. (d) STEM image of HEA-NPs/C at a lower resolution.

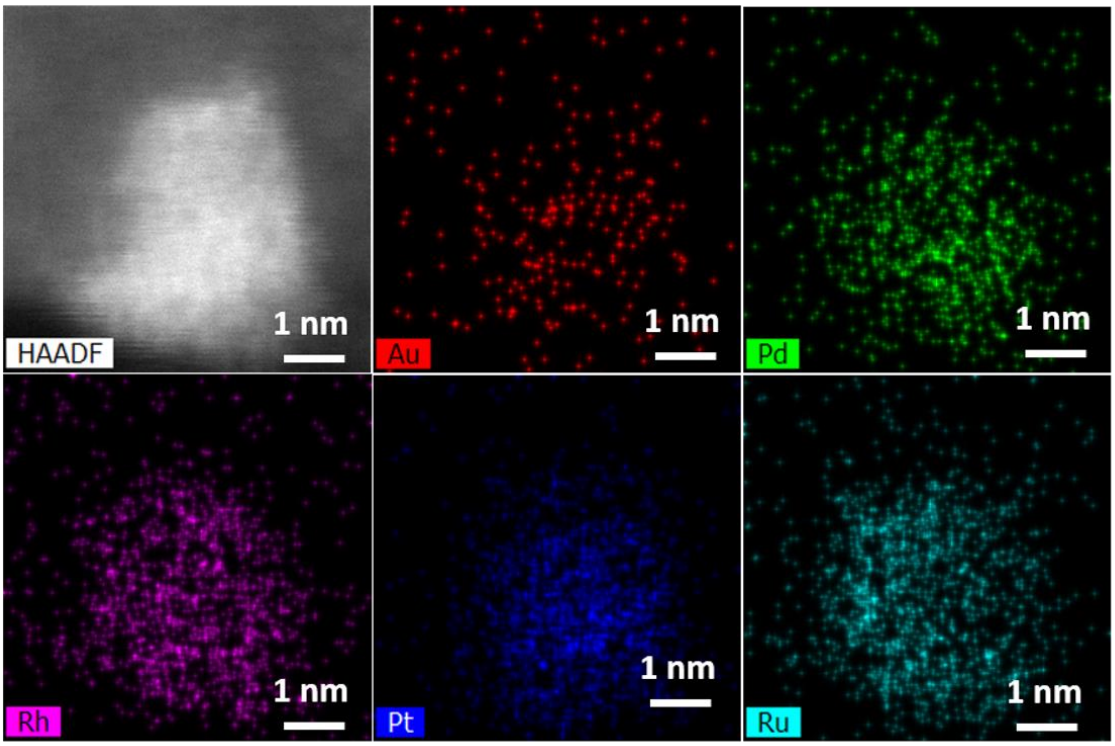

Figure 4.8. HAADF image and EDS elemental maps of the HEA-NPs/C synthesized via the ultrasound-driven wet chemistry method promoted by alcoholic ionic liquid.

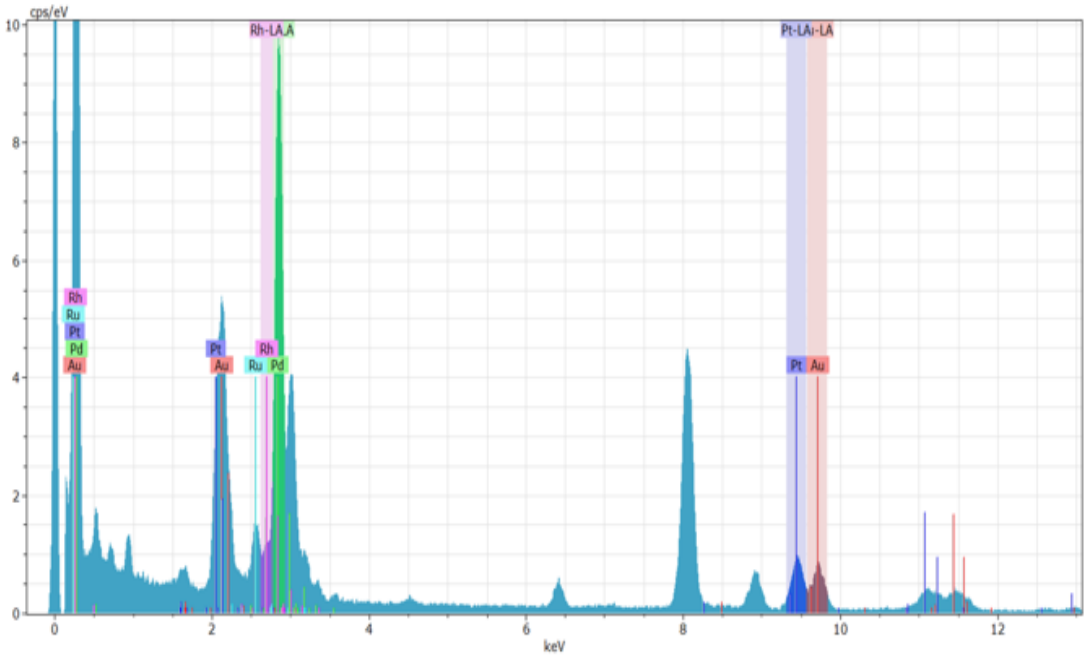

Figure 4.9. EDS spectrum of the supported high-entropy alloy nanoparticle catalysts (HEA-NP/C) showing the constituent elements.

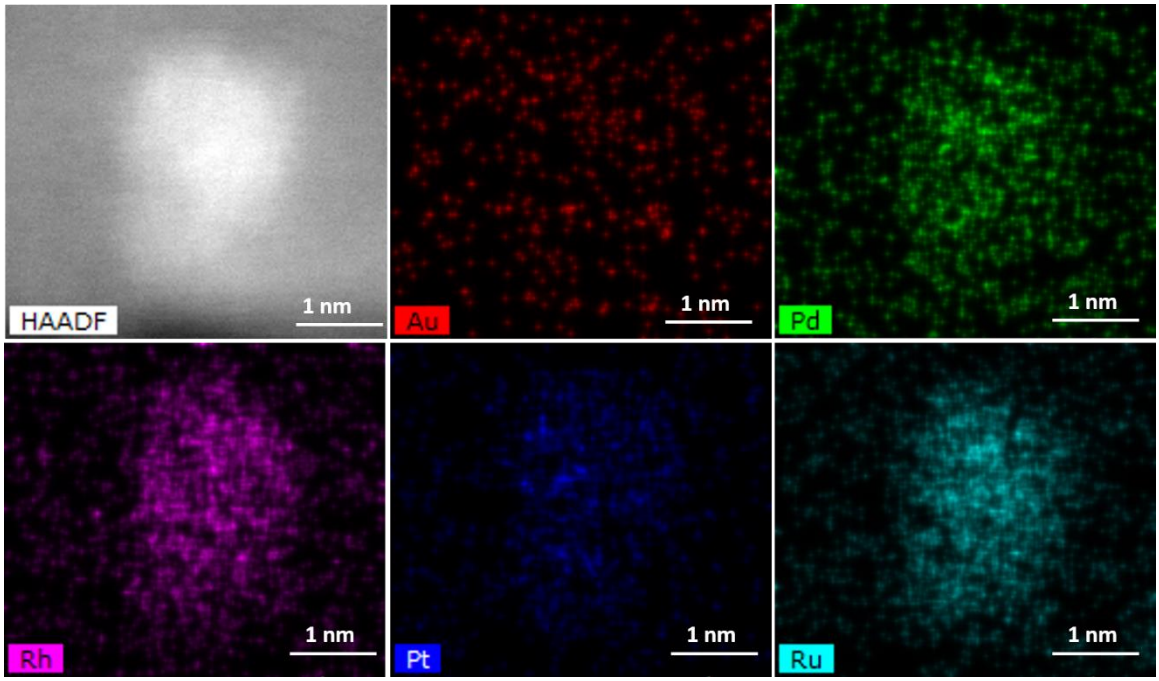

Figure 4.10. HAADF image and EDS elemental maps of the supported high-entropy alloy nanocatalyst (HEANPs/C) synthesized via the ultrasound-driven wet chemistry method promoted by alcoholic ionic liquid (AIL).

erials. Also, the overall metal loading is determined to be 9.7 wt.%, which is close to the theoretical 10 wt.% metal loadings. We can conclude from these results that a single-phase solid solution of AuPdPtRhRh-NPs has been realized in one step via the proposed ultrasound-driven wet chemistry protocol promoted by AIL.

To demonstrate the flexibility of our synthetic strategy, binary, ternary, and quaternary multicomponent alloys were fabricated following the synthetic protocol. As seen in fig. 4.11, the XRD patterns, like the quinary alloy display four distinct peaks that correspond to the standard Braggs reflections of the fcc crystal lattice with no phase segregation. Also, a quinary alloy with theoretical atomic percent of 15, 25, 25, 20, and 15 for Au, Pd, Pt, Rh, and Ru respectively was synthesized to investigate how easily the alloy composition can be controlled. The actual atomic percentages based on the ICP-OES data analysis are 14.7, 24.9, 25.2, 19.8, and 15.4 which corresponds to approximately 0.6:1:1:0.8:0.6 mole ratio respectively as expected. Additionally, we utilized [HEMMor][BF_4], which has markedly distinct physical properties from [HEMMor][NTf_2] as the reaction medium to demonstrate the flexibility of the reaction medium. The as-obtained nanocrystals, (see figure 4.12), show similar diffraction peaks as those from [HEMMor][NTf_2], which unambiguously proves the adaptability of our synthetic protocol. To underscore the importance of the hydroxyl functionality in the formation of single-phase nanocrystals of AuPdPtRhRh in one step, [HEMMor][NTf_2] was replaced with the “non-hydroxyl” counterpart, i.e., [EMMor][NTf_2] as the reaction medium. The formation of phase-segregated XRD patterns (see figure 4.12) provides evidence

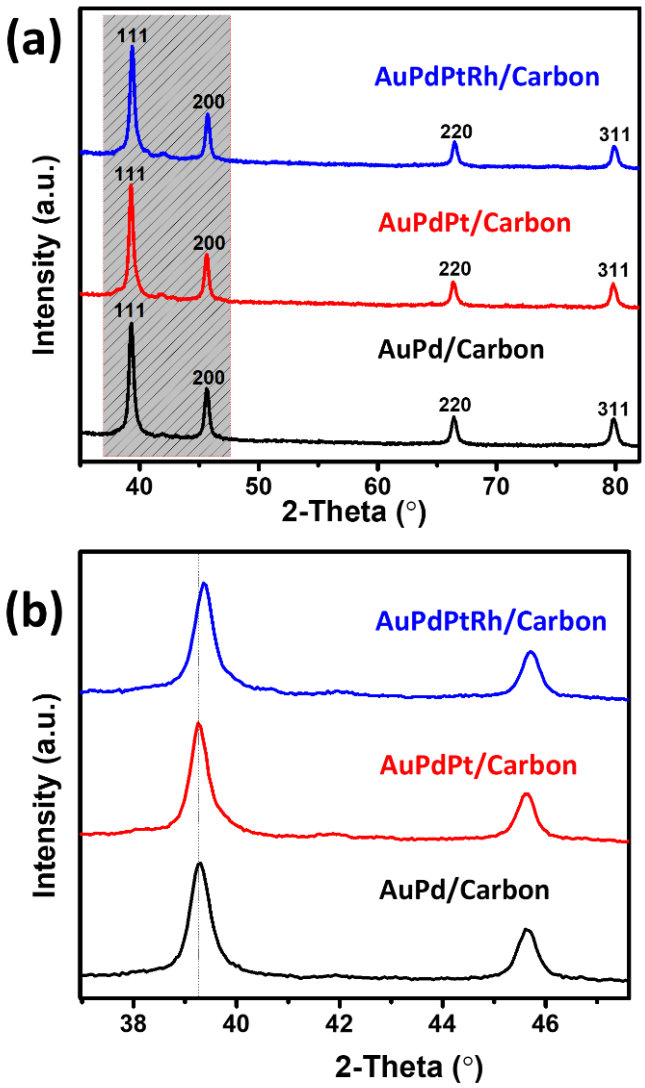

Figure 4.11. (a) XRD patterns of supported multicomponent alloy nanocatalysts synthesized via the ultrasound-driven wet chemistry method promoted by alcoholic ionic liquid (AIL). The shift in reflection positions with the addition of more elements is denoted by the dotted lines in (b).

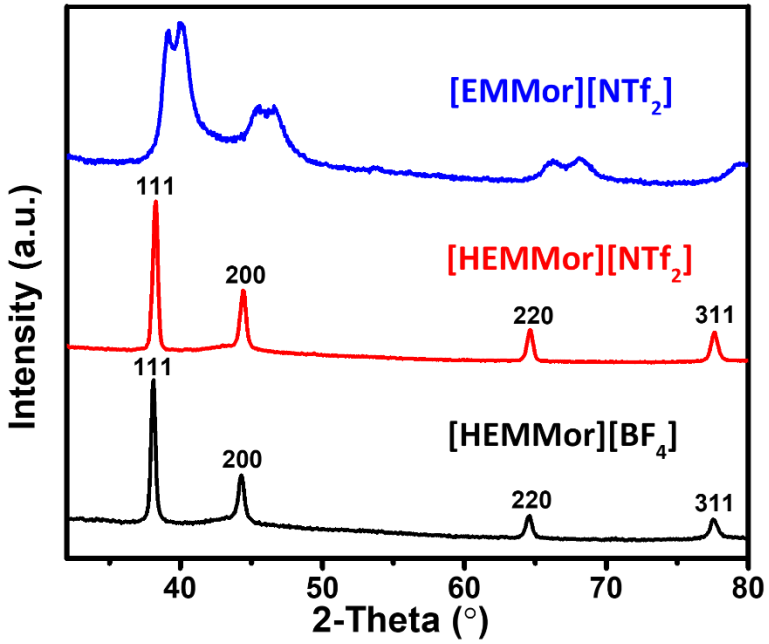

Figure 4.12. XRD patterns of multicomponent alloys derived in different kinds of IL (AIL—bottom two and non-AIL—top one.)

that the hydroxyl functionality is crucial in the formation of single-phase HEA nanocrystals in one step.

Notably, alcohol-functionalized imidazolium-based ionic liquids applied under similar synthesis conditions as [HEMMor][NTf_2] and [HEMMor][BF_4] yielded complex XRD patterns that are quite difficult to interpret. The origin of this complexity is not exactly known at this at this period.

The surface composition of HEA-NPs/C was analyzed by the XPS technique. Figure 4.13 (a) shows the XPS survey spectrum, which contains C and O in higher concentrations along with the anticipated metals (Pd, Pt, Ru, Rh, and Au) in much lower concentrations. To understand the valence states of metals, the core-level spectra of Au 4f, Pd 3d, Pt 4f, Rh $3d_{5/2}$, and Ru $3d3d_{5/2}$ were acquired (see figure 4.13). Au, Pd, and Pt show asymmetric peak shapes, which indicates that they are primarily in their metallic states. The C1s spectrum overlapped with the Ru 3d which precludes the ability to determine the valence state of Ru. Also, the valence state for the weak Rh peak could not be determined from this data.

4.11 Selective phenol hydrogenation

Cyclohexanone is an important chemical intermediate in the manufacture of ε-caprolactam, a raw material used in the production of nylon-6.[38–40] It can be obtained by the oxidation of cyclohexane which requires high temperature and pressure and often leads to the formation of undesirable side products.[41] Selective hydrogenation of phenol (figure 4.14) is an alternative pathway in which cyclohexanone selectivity largely depends on the properties of the catalysts.[41–49]

Tunning the electronic and geometric structures of the catalysts is a workable strategy to improve performance, as has been demonstrated from the results of various bimetallic catalysts.[50–55] HEAs consist of even more elements and thus regulate the geometric and electronic structures to a larger extent. The severe lattice distortion induced by the atomic size mismatch raises their potential energy, resulting in lower activation energy during catalytic processes.[4] Rationally, the catalytic activity of HEA-NPs/C was investigated for selective hydrogenation of phenol. As seen in Table 4.1, HEA-NPs/C efficiently catalyzes phenol hydrogenation, yielding cyclohexanone as the predominant product. The phenol conversion is 88.7% within 1 hour at 150 °C and 1 MPa H_2 pressure (Table 4.1, entry 1). Upon increasing the reaction time to 2.5 hours, the phenol conversion reaches 96.3% with a cyclohexanone selectivity of 96.4%. Beyond 2.5 hours reaction time, a close to 100% phenol conversion and cyclohexanone selectivity are achieved. Meanwhile, as the pressure is increased to 2.0 MPa, the conversion exceeds 98% within 1 hour, with selectivity for cyclohexanone as high as 99.8% (Table 1, entry 6). The relatively high selectivity of HEANPs/C is possibly due to the favorable desorption of cyclohexanone on the catalyst surface, inhibiting its further hydrogenation to cyclohexanol.[56,57] A similar selectivity trend towards cyclohexanone production has also been demonstrated in other liquid-phase phenol hydrogenation catalyzed by Pd-based materials.[58] Under similar conditions, the catalytic performance of other multi-component alloys investigated in the hydrogenation process decreases in the following order (figure 4.15): quinary (AuPdPtRhRu) > quaternary (AuPdPtRh) > ternary (AuPdPt) > binary (AuPd).

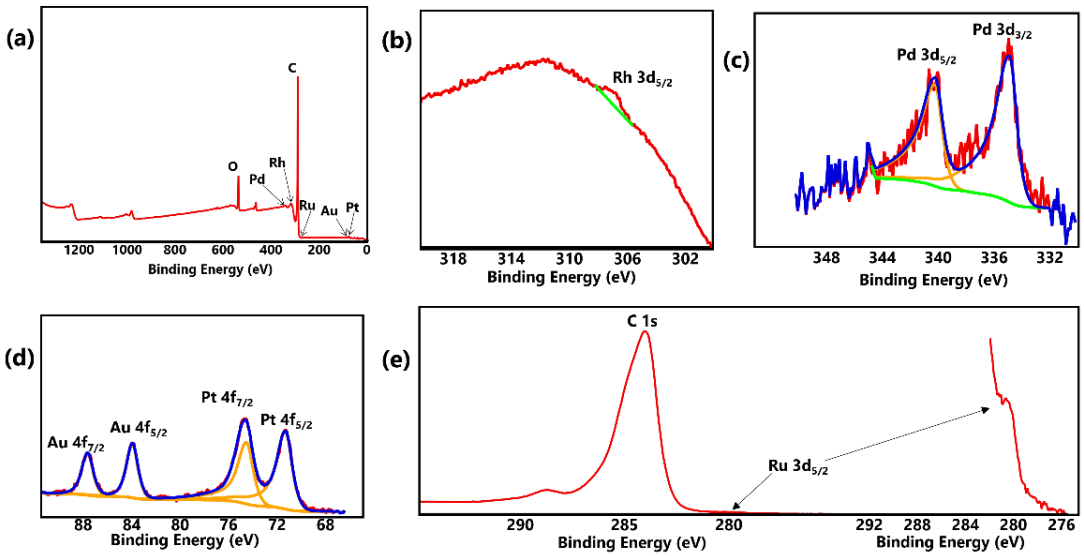

Figure 4.13. (a) XPS survey spectrum of HEA-NPs/C; (b) core-level spectra of Rh 3d; (c) core-level spectra of Pd 3d; (d) core-level spectra of Au 4f and Pt 4f, (e) core-level spectra of C 1s and Ru 3d.

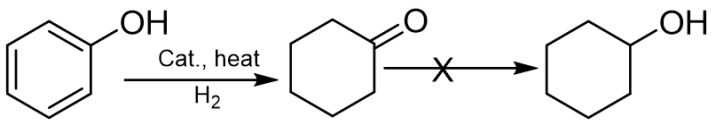

Figure 4.14. Catalytic selective hydrogenation of phenol to cyclohexanone.

The configurational entropy of the multicomponent alloys increases with the addition of different elements; alloys in higher configurational entropy state demonstrate a higher synergistic effect, hence, superior catalytic performance. Notably, a commercial Pd-NPs/C (Pd-NP/C_com) shows an inferior catalytic performance relative to HEA-NPs/C but similar to as-synthesized Pd-NPs/C under similar reaction conditions. In figure 4.16, HEA-NPs/C displays a phenol conversion of 88.7% at 150 °C with 1 MPa H_2 pressure within 1 hour, which is higher than commercial Pd-NP/C_com (76.9%) and as-synthesized Pd-NPs/C catalysts (70.5%) under the same reaction conditions. Meanwhile, the cyclohexanone selectivity over all three catalysts is virtually the same. Although Pd-based catalysts are predominantly used in selective hydrogenation of phenol, it is important to note that Pt,[59–61] Rh,[38,62–64] and even Ru-based catalysts [65,66] have all been investigated with satisfactory results (Table 4.2). Nevertheless, our HEA-NPs/C performs better than several noble metallic catalysts so far reported at relatively milder conditions.[67–69] For example, while Ru/γ-Al_2O_3 exhibits an 88% phenol conversion and 83% cyclohexanone selectivity at 160 °C, 2 hours reaction time and 5 MPa H_2 pressure (Table 4.2, entry 3), our HEA-NPs/C catalyst shows a much higher phenol of 98.5% and cyclohexanone selectivity of 99.8% at milder conditions (150 °C, 1 hour reaction time and 2 MPa H_2 pressure). Similarly, HEA-NPs/C shows superior cyclohexanone selectivity of 99.8% compared to Rh/SiO_2 with 82.6% cyclohexanone selectivity (Table 4.2, entry 27). While there are a few single component noble metal catalysts that are more active and/or selective in

Table 4.1. Results of phenol hydrogenation by HEA-NPs/C under different conditions.

Entry	Time (h)	H_2 pressure (MPa)	Conversion (%)	Selectivity	
				C═O	C─O
1	1	1.0	88.7	97.8	2.2
2	2.5	1.0	96.3	96.4	3.6
3	6	1.0	99.8	99.5	0.5
4	12	1.0	99.8	99.1	0.9
5	24	1.0	99.2	99.6	0.4
6	1	2.0	98.5	99.8	0.2

Reaction conditions: phenol (1.3 mmol), AuPdPtRhRu (10wt.% in HEA-NPs/C, 2.8 mol% relative to phenol; average molecular mass ≈ 140.5 g/mol), temperature = 150 °C, C═O denotes cyclohexanone and C─O denotes cyclohexanol.

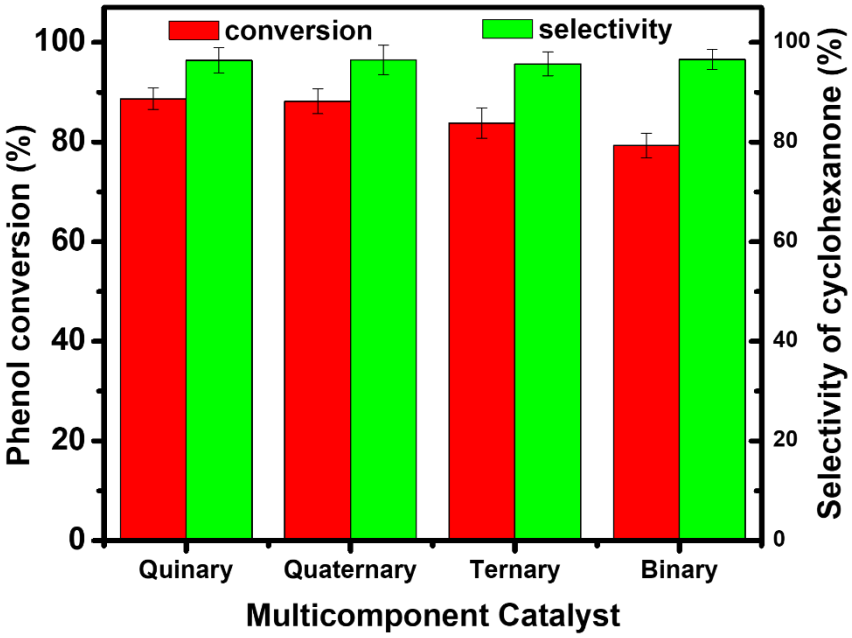

Figure 4.15. Selective hydrogenation of phenol over different multicomponent catalysts (quinary (AuPdPtRhRu), quaternary (AuPdPtRh), ternary (AuPdPt), binary (AuPd), 1.3 mmol phenol, 2.8 mol% active metals relative to phenol, 150 ^{o}C, 1 MPa H_2, 1 hour)

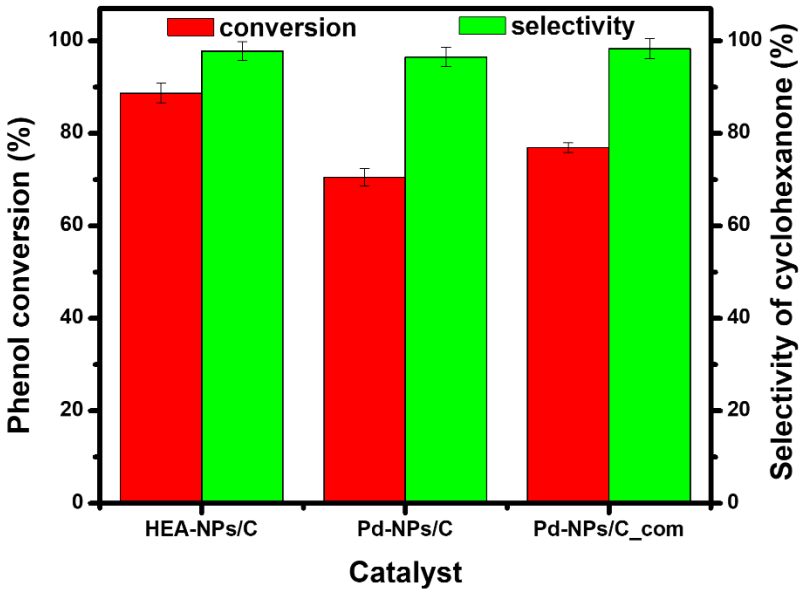

Figure 4.16. Selective hydrogenation of phenol over different catalysts (1.3 mmol phenol, 2.8 mol% active metals relative to phenol, 150 °C, 1 MPa H_2, 1 hour).

Table 4.2 Summary of hydrogenation of phenol to cyclohexanone over noble metal-based catalysts (Referenced articles are found on page 124).

Catalyst	Solvent	Reactor	Temp. (°C)	Time (h)	H_2 pressure (MPa)	Conversion (%)	Selectivity (%)	Ref.
9.7 wt% AuPdPtRhRu/C	Hexane	Autoclave	150	2.5	1	96.3	96.4	This work
9.7 wt% AuPdPtRhRu/C	Hexane	Autoclave	150	1	2	98.5	99.8	This work
5.0 wt% Ru/γ-Al_2O_3	Cyclohexane	Autoclave	160	2	5	88	83	[12]
5.0 wt% Ru/MIL-101	CH_2Cl_2	Batch reactor	50	4	0.5	80	74	[13]
5.0 wt% Ru/MIL-101	H_2O	Batch reactor	50	4	0.5	90	90	[13]
Pd/mpg-C_3N_4	H_2O		45	12	0.1	99	98.5	[14]
Pd/mpg-C_3N_4	H_2O		100	1	0.1	99	99	[14
Pd–Ca/La_2O_3	C_2H_5OH	Tubular reactor	220		0.1	52	93	[15]
Pd–Ca/CeO_2	C_2H_5OH	Tubular reactor	220		0.1	55	92	[15]
Pd–Ca/Al_2O_3	C_2H_5OH	Tubular reactor	220		0.1	38	93	[15]
5 wt%Ru/γ-Al_2O_3	Cyclohexane	Autoclave	160	3	5	100	90	[16]
2.7 wt%Pd/A-45	H_2O	Reactor	100	3	1	100	89.9	[17]
2.2 wt%Rh@S-MIL-101	CH_2Cl_2	Batch reactor	50	2	0.5	91	85	[18]
5 wt%Pd/MIL-101	H_2O	Autoclave	25	11	0.1	99.9	99.9	[19]
2 mol%Pd/C	H_2O, HCOOK	Round bottom flask	90	6	Open atmosphere	99	99	[20]
Rh	Cyclodextrins		60	3	4	88	100	[21]
5 wt%Pd/Al_2O_3	CH_2Cl_2		30	12	1	15.5	89.5	[22]
5 wt%Pd/Al_2O_3, $AlCl_3$	CH_2Cl_2		30	8	1	99.9	99.9	[22]
2mol%Pd/C	H_2O, HCOOK	Round bottom flask	90	6	Open atmosphere	99	99	[21]
8.1 wt% Rh@SiCN	GVL, H_2O	Steel autoclave	25	4	0.6	67	72	[23]
8.1 wt% Rh@SiCN	H_2O	Steel autoclave	25	2	0.6	54	67	[23]
8.1 wt% Rh@SiCN	CH_3COCH_3, H_2O	Steel autoclave	25	2	0.6	37	82	[23]
2.2 wt%Rh@S-MIL-101	H_2O	Batch reactor	50	2	0.5	95	92	[18]
0.6 wt%Ru@NaX	H_2O	Three-necked flask	80	10	0.1	90	99.9	[24]
1 wt%Pd–HAP	H_2O	Tube	75	3	0.1	100	100	[25]
1 wt%Pt@TNT	CH_2Cl_2	Autoclave	50		0.5	95	83	[26]
5 wt%Rh/SiO_2	Cyclohexane	Autoclave	30	9	0.1	100	82.6	[27]
Pd/CNTs	CH_3OH	Tubular reactor	220		3.5[a]	18	99	[28]
3 wt%Pt-out/CNTs	CH_2Cl_2	Autoclave	50	0.5	0.5	11.6	72.3	[29]

[a] Argon pressure.

reaction conditions that are milder than reported in the present work, it is important to note, however, that these single noble metal catalysts are often used in conjunction with Lewis acids as dual catalysts to activate the benzene ring and suppress further hydrogenation of cyclohexanone to cyclohexanol.[40] The superior catalytic performance of HEA-NPs/C is ascribed to the strong synergistic effect resulting from the combination of catalytically active metals. The numerous possible arrangements of different atoms on the catalyst surface may have provided different adsorption modes for phenol and its intermediate, hence the superior catalytic performance. The recyclability of HEA-NPs/C was investigated through repeated hydrogenation experiments following a facile solvent wash process with acetone. As seen in figure 4.17, HEA-NPs/C demonstrates excellent stability, yielding phenol conversion and selectivity for cyclohexanone greater than 95% under the test conditions across all five usage cycles.

4.12 Conclusions

Summarily, we demonstrate a facile synthetic method to fabricate HEA-NP catalysts on a carbon support. Our methodology is based on the transient localized hotspot induced by the physical phenomenon of acoustic cavitation (formation, growth, and implosive collapse of microscopic-sized bubbles in a liquid) observed in ultrasound irradiation of liquids. Owing to the reducing ability of alcohols, AILs were utilized as environmentally friendly reducing agent-cum-solvent in our strategy, co-reducing the precursor ions under high-intensity ultrasound irradiation in ambient conditions. The as-obtained NPs show superior performance for

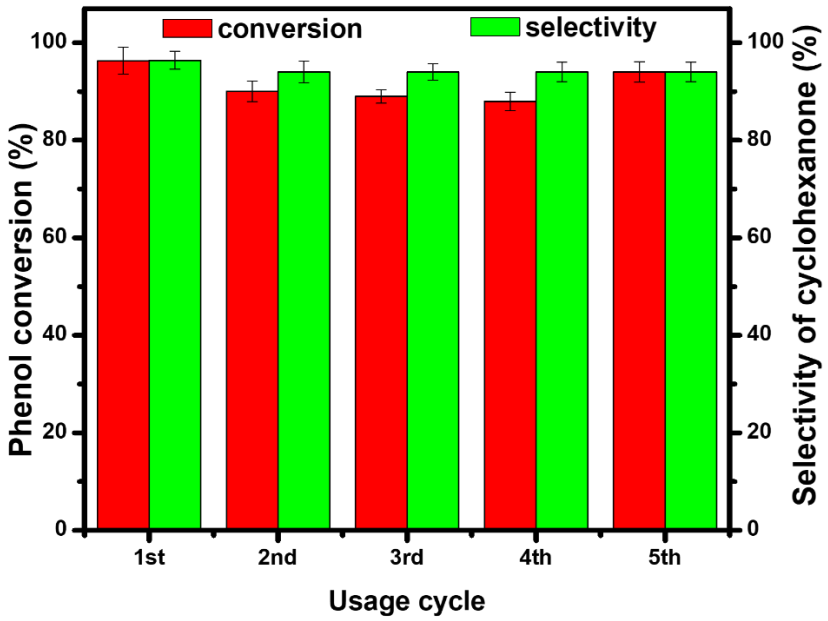

Figure 4.17. Reusability performance of HEA-NPs/C catalyst in phenol hydrogenation (1.3 mmol phenol, 2.8 mol% active metals relative to phenol, 150 °C, 2 MPa H_2, 1 hour)

selective hydrogenation of phenol compared to the monometallic counterparts due to the strong synergistic effects. Such a technologically feasible and facile synthetic method provides an improved methodology for the sustainable synthesis of multicomponent alloys for catalysis and other applications.

4.13 Acknowledgments

This work was supported by the Division of Chemical Sciences, Geosciences, and Biosciences, Office of Basic Energy Sciences, US Department of Energy. We also thank the Science Alliance for the Graduate Advancement, Training, and Education (GATE) scholarship award. We are truly grateful to Avery Blockmon for his contributions.

REFERENCES

[1] Fu, Z. Q.; Jiang, L.; Wardini, J. L.; MacDonald, B. E.; Wen, H. M.; Xiong, W.; Zhang, D. L.; Zhou, Y. Z.; Rupert, T. J.; Chen, W. P. et al. A high-entropy alloy with hierarchical nanoprecipitates and ultrahigh strength. *Sci*. *Adv*. **2018**, *4*, eaat8712.

[2] Yao, Y. G.; Liu, Z. Y.; Xie, P. F.; Huang, Z. N.; Li, T. Y.; Morris, D.; Finfrock, Z.; Zhou, J. H.; Jiao, M. L.; Gao, J. L. et al. Computationally aided, entropy-driven synthesis of highly efficient and durable multi-elemental alloy catalysts. *Sci*. *Adv*. **2020**, *6*, eaaz0510.

[3] Löffler, T.; Savan, A.; Garzón-Manjón, A.; Meischein, M.; Scheu, C.; Ludwig, A.; Schuhmann, W. Toward a paradigm shift in electrocatalysis using complex solid solution nanoparticles. *ACS Energy Lett*. **2019**, *4*, 1206–1214.

[4] Xin, Y.; Li, S. H.; Qian, Y. Y.; Zhu, W. K.; Yuan, H. B.; Jiang, P. Y.; Guo, R. H.; Wang, L. B. High-entropy alloys as a platform for catalysis: Progress, challenges, and opportunities. *ACS Catal*. **2020**, *10*, 11280–11306.

[5] Chen, H.; Jie, K. H.; Jafta, C. J.; Yang, Z. Z.; Yao, S. Y.; Liu, M. M.; Zhang, Z. H.; Liu, J. X.; Chi, M. F.; Fu, J. et al. An ultrastable heterostructured oxide catalyst based on high-entropy materials: A new strategy toward catalyst stabilization via synergistic interfacial interaction. *Appl*. *Catal*. *B Environ*. **2020**, *276*, 119155.

[6] Xu, H. D.; Zhang, Z. H.; Liu, J. X.; Do-Thanh, C. L.; Chen, H.; Xu, S. H.; Lin, Q. J.; Jiao, Y.; Wang, J. L.; Wang, Y. et al. Entropy-stabilized single-atom Pd

catalysts via high-entropy fluorite oxide supports. *Nat*. *Commun*. **2020**, *11*, 3908.

[7] Shu, Y.; Bao, J. F.; Yang, S. Z.; Duan, X. L.; Zhang, P. F. Entropy-stabilized metal-CeO_x solid solutions for catalytic combustion of volatile organic compounds. *AlChE J*. **2021**, *67*, e17046.

[8] Feng, D. Y.; Dong, Y. B.; Zhang, L. L.; Ge, X.; Zhang, W.; Dai, S.; Qiao, Z. A. Holey lamellar high-entropy oxide as an ultra-high-activity heterogeneous catalyst for solvent-free aerobic oxidation of benzyl alcohol. *Angew*. *Chem*. **2020**, *132*, 19671–19677.

[9] Yao, Y. G.; Huang, Z. N.; Xie, P. F.; Lacey, S. D.; Jacob, R. J.; Xie, H.; Chen, F. J.; Nie, A. M.; Pu, T. C.; Rehwoldt, M. et al. Carbothermal shock synthesis of high-entropy-alloy nanoparticles. *Science* **2018**, *359*, 1489–1494.

[10] Chen, Y. F.; Zhan, X.; Bueno, S. L. A.; Shafei, I. H.; Ashberry, H. M.; Chatterjee, K.; Xu, L.; Tang, Y. W.; Skrabalak, S. E. Synthesis of monodisperse high entropy alloy nanocatalysts from core@shell nanoparticles. *Nanoscale Horiz*. **2021**, *6*, 231–237.

[11] Xie, P. F.; Yao, Y. G.; Huang, Z. N.; Liu, Z. Y.; Zhang, J. L.; Li, T. Y.; Wang, G. F.; Shahbazian-Yassar, R.; Hu, L. B.; Wang, C. Highly efficient decomposition of ammonia using high-entropy alloy catalysts. *Nat*. *Commun*. **2019**, *10*, 4011.

[12] Lv, Z. Y.; Liu, X. J.; Jia, B.; Wang, H.; Wu, Y.; Lu, Z. P. Development of a novel high-entropy alloy with eminent efficiency of degrading azo dye solutions. *Sci*. *Rep*. **2016**, *6*, 34213.

[13] Wu, S. K.; Pan, Y.; Wang, N.; Lu, T.; Dai, W. J. Azo dye degradation behavior of AlFeMnTiM (M = Cr, Co, Ni) high-entropy alloys. *Int*. *J*. *Min*. *Met*. *Mater*.

2019, *26*, 124–132.

[14] Qiu, H. J.; Fang, G.; Wen, Y. R.; Liu, P.; Xie, G. Q.; Liu, X. J.; Sun, S. H. Nanoporous high-entropy alloys for highly stable and efficient catalysts. *J. Mater. Chem. A* **2019**, *7*, 6499–6506.

[15] Zhang, G. L.; Ming, K. S.; Kang, J. L.; Huang, Q.; Zhang, Z. J.; Zheng, X. R.; Bi, X. F. High entropy alloy as a highly active and stable electrocatalyst for hydrogen evolution reaction. *Electrochim. Acta* **2018**, *279*, 19–23.

[16] Waag, F.; Li, Y.; Ziefuß, A. R.; Bertin, E.; Kamp, M.; Duppel, V.; Marzun, G.; Kienle, L.; Barcikowski, S.; Gökce, B. Kinetically-controlled laser-synthesis of colloidal high-entropy alloy nanoparticles. *RSC Adv.* **2019**, *9*, 18547–18558.

[17] Pedersen, J. K.; Batchelor, T. A. A.; Bagger, A.; Rossmeisl, J. High-entropy alloys as catalysts for the CO_2 and CO reduction reactions. *ACS Catal.* **2020**, *10*, 2169–2176.

[18] Sun, Y. F.; Dai, S. High-entropy materials for catalysis: A new frontier. *Sci. Adv.* **2021**, *7*, eabg1600.

[19] Dai, S. Across the board: Sheng dai on catalyst design by entropic factors. *ChemSusChem* **2020**, *13*, 1915–1917.

[20] Wang, T.; Chen, H.; Yang, Z. Z.; Liang, J. Y.; Dai, S. High-entropy perovskite fluorides: A new platform for oxygen evolution catalysis. *J. Am. Chem. Soc.* **2020**, *142*, 4550–4554.

[21] Yang, Y.; Song, B. A.; Ke, X.; Xu, F. Y.; Bozhilov, K. N.; Hu, L. B.; Shahbazian-Yassar, R.; Zachariah, M. R. Aerosol synthesis of high entropy alloy nanoparticles. *Langmuir* **2020**, *36*, 1985–1992.

[22] Gao, S. J.; Hao, S. Y.; Huang, Z. N.; Yuan, Y. F.; Han, S.; Lei, L. C.; Zhang, X. W.; Shahbazian-Yassar, R.; Lu, J. Synthesis of high-entropy alloy nanoparticles on supports by the fast-moving bed pyrolysis. *Nat*. *Commun*. **2020**, *11*, 2016.

[23] Joo, S. H.; Bae, J. W.; Park, W. Y.; Shimada, Y.; Wada, T.; Kim, H. S.; Takeuchi, A.; Konno, T. J.; Kato, H.; Okulov, I. V. Beating thermal coarsening in nanoporous materials via high-entropy design. *Adv*. *Mater*. **2020**, *32*, 1906160.

[24] Okulov, A. V.; Joo, S. H.; Kim, H. S.; Kato, H.; Okulov, I. V. Nanoporous high-entropy alloy by liquid metal dealloying. *Metals* **2020**, *10*, 1396.

[25] Rekha, M. Y.; Mallik, N.; Srivastava, C. First report on high entropy alloy nanoparticle decorated graphene. *Sci*. *Rep*. **2018**, *8*, 8737.

[26] Löffler, T.; Meyer, H.; Savan, A.; Wilde, P.; Garzón Manjón, A.; Chen, Y. T.; Ventosa, E.; Scheu, C.; Ludwig, A.; Schuhmann, W. Discovery of a multinary noble metal–free oxygen reduction catalyst. *Adv*. *Energy Mater*. **2018**, *8*, 1802269.

[27] Bondesgaard, M.; Broge, N. L. N.; Mamakhel, A.; Bremholm, M.; Iversen, B. B. General solvothermal synthesis method for complete solubility range bimetallic and high-entropy alloy nanocatalysts. *Adv*. *Funct*. *Mater*. **2019**, *29*, 1905933.

[28] Bang, J. H.; Suslick, K. S. Applications of ultrasound to the synthesis of nanostructured materials. *Adv*. *Mater*. **2010**, *22*, 1039–1059.

[29] Xu, H. X.; Zeiger, B. W.; Suslick, K. S. Sonochemical synthesis of nanomaterials. *Chem*. *Soc*. *Rev*. **2013**, *42*, 2555–2567.

[30] Okejiri, F.; Zhang, Z. H.; Liu, J. X.; Liu, M. M.; Yang, S. Z.; Dai, S. Room-temperature synthesis of high-entropy perovskite oxide nanoparticle catalysts

through ultrasonication-based method. *ChemSusChem* **2020**, *13*, 111–115.

[31] Liu, M. M.; Zhang, Z. H.; Okejiri, F.; Yang, S. Z.; Zhou, S. H.; Dai, S. Entropy-maximized synthesis of multimetallic nanoparticle catalysts via a ultrasonication-assisted wet chemistry method under ambient conditions. *Adv*. *Mater*. *Interfaces* **2019**, *6*, 1900015.

[32] Kim, K. S.; Choi, S.; Cha, J. H.; Yeon, S. H.; Lee, H. Facile one-pot synthesis of gold nanoparticles using alcohol ionic liquids. *J*. *Mater*. *Chem*. **2006**, *16*, 1315–1317.

[33] Yeon, S. H.; Kim, K. S.; Choi, S.; Lee, H.; Kim, H. S.; Kim, H. Physical and electrochemical properties of 1-(2-hydroxyethyl)-3-methyl imidazolium and *N*-(2-hydroxyethyl)-*N*-methyl morpholinium ionic liquids. *Electrochim*. *Acta* **2005**, *50*, 5399–5407.

[34] Anderson, J. L.; Clark, K. D. Ionic liquids as tunable materials in (bio)analytical chemistry. *Anal*. *Bioanal*. *Chem*. **2018**, *410*, 4565–4566.

[35] Wu, Q. M.; Hong, X.; Zhu, L. F.; Meng, X. J.; Han, S. C.; Zhang, J.; Liu, X. L.; Jin, C. H.; Xiao, F. S. Generalized ionothermal synthesis of silica-based zeolites. *Microporous Mesoporous Mater*. **2019**, *286*, 163–168.

[36] Zhang, P. F.; Gong, Y. T.; Lv, Y. Q.; Guo, Y.; Wang, Y.; Wang, C. M.; Li, H. R. Ionic liquids with metal chelate anions. *Chem*. *Commun*. **2012**, *48*, 2334–2336.

[37] Lu, H. F.; Zhang, P. F.; Qiao, Z. A.; Zhang, J. S.; Zhu, H. Y.; Chen, J. H.; Chen, Y. F.; Dai, S. Ionic liquid-mediated synthesis of meso-scale porous lanthanum-transition-metal perovskites with high CO oxidation performance. *Chem*. *Commun*. **2015**, *51*, 5910–5913.

[38] Fujita, S. i.; Yamada, T.; Akiyama, Y.; Cheng, H. Y.; Zhao, F. Y.; Arai, M. Hydrogenation of phenol with supported Rh catalysts in the presence of compressed CO_2: Its effects on reaction rate, product selectivity and catalyst life. *J*. *Supercrit*. *Fluids* **2010**, *54*, 190–201.

[39] Xiang, Y. Z.; Ma, L.; Lu, C. S.; Zhang, Q. F.; Li, X. N. Aqueous system for the improved hydrogenation of phenol and its derivatives. *Green Chem*. **2008**, *10*, 939–943.

[40] Liu, H. Z.; Jiang, T.; Han, B. X.; Liang, S. G.; Zhou, Y. X. Selective phenol hydrogenation to cyclohexanone over a dual supported Pd–Lewis acid catalyst. *Science* **2009**, *326*, 1250–1252.

[41] Mahata, N.; Raghavan, K. V.; Vishwanathan, V.; Park, C.; Keane, M. A. Phenol hydrogenation over palladium supported on magnesia: Relationship between catalyst structure and performance. *Phys*. *Chem*. *Chem*. *Phys*. **2001**, *3*, 2712–2719.

[42] Chatterjee, M.; Kawanami, H.; Sato, M.; Chatterjee, A.; Yokoyama, T.; Suzuki, T. Hydrogenation of phenol in supercritical carbon dioxide catalyzed by palladium supported on Al-MCM-41: A facile route for one-pot cyclohexanone formation. *Adv*. *Synth*. *Catal*. **2009**, *351*, 1912–1924.

[43] Nelson, N. C.; Manzano, J. S.; Sadow, A. D.; Overbury, S. H.; Slowing, I. I. Selective hydrogenation of phenol catalyzed by palladium on high-surface-area ceria at room temperature and ambient pressure. *ACS Catal*. **2015**, *5*, 2051–2061.

[44] Mahata, N.; Vishwanathan, V. Influence of palladium precursors on structural properties and phenol hydrogenation characteristics of supported

palladium catalysts. *J*. *Catal*. **2000**, *196*, 262–270.

[45] Xu, G. Y.; Guo, J. H.; Zhang, Y.; Fu, Y.; Chen, J. Z.; Ma, L. L.; Guo, Q. X. Selective hydrogenation of phenol to cyclohexanone over Pd-HAP catalyst in aqueous media. *ChemCatChem* **2015**, *7*, 2485–2492.

[46] Zhu, J. F.; Tao, G. H.; Liu, H. Y.; He, L.; Sun, Q. H.; Liu, H. C. Aqueous-phase selective hydrogenation of phenol to cyclohexanone over soluble Pd nanoparticles. *Green Chem*. **2014**, *16*, 2664–2669.

[47] Liu, S. W.; Han, J.; Wu, Q.; Bian, B.; Li, L.; Yu, S. T.; Song, J.; Zhang, C.; Ragauskas, A. J. Hydrogenation of phenol to cyclohexanone over bifunctional Pd/C-heteropoly acid catalyst in the liquid phase. *Catal*. *Lett*. **2019**, *149*, 2383–2389.

[48] Makowski, P.; Demir Cakan, R.; Antonietti, M.; Goettmann, F.; Titirici, M. M. Selective partial hydrogenation of hydroxy aromatic derivatives with palladium nanoparticles supported on hydrophilic carbon. *Chem*. *Commun*. **2008**, 999–1001.

[49] Chen, H.; Sun, J. S. Selective hydrogenation of phenol for cyclohexanone: A review. *J*. *Ind*. *Eng*. *Chem*. **2021**, *94*, 78–91.

[50] Srinivas, S. T.; Rao, P. K. Highly selective Pt–Cr/C alloy catalysts for single-step vapour phase hydrogenation of phenol to give cyclohexanone. *J*. *Chem*. *Soc*., *Chem*. *Commun*. **1993**, 33–34.

[51] Shore, S. G.; Ding, E. R; Park, C.; Keane, M. A. Vapor phase hydrogenation of phenol over silica-supported Pd and Pd-Yb catalysts. *Catal*. *Commun*. **2002**, *3*, 77–84.

[52] Yang, X.; Du, L.; Liao, S. J.; Li, Y. X.; Song, H. Y. High-performance gold-

promoted palladium catalyst towards the hydrogenation of phenol with mesoporous hollow spheres as support. *Catal*. *Commun*. **2012**, *17*, 29–33.

[53] Lin, H. H.; Muzzio, M.; Wei, K. C.; Zhang, P.; Li, J. R.; Li, N.; Yin, Z. Y.; Su, D.; Sun, S. H. PdAu alloy nanoparticles for ethanol oxidation in alkaline conditions: Enhanced activity and C1 pathway selectivity. *ACS Appl*. *Energy Mater*. **2019**, *2*, 8701–8706.

[54] Muzzio, M.; Yu, C.; Lin, H. H.; Yom, T.; Boga, D. A.; Xi, Z.; Li, N.; Yin, Z. Y.; Li, J. R.; Dunn, J. A. et al. Reductive amination of ethyl levulinate to pyrrolidones over AuPd nanoparticles at ambient hydrogen pressure. *Green Chem*. **2019**, *21*, 1895–1899.

[55] Wang, L. X.; He, S. X.; Wang, L.; Lei, Y.; Meng, X. J.; Xiao, F. S. Cobalt–nickel catalysts for selective hydrogenation of carbon dioxide into ethanol. *ACS Catal*. **2019**, *9*, 11335–11340.

[56] Zhong, J. W.; Chen, J. Z.; Chen, L. M. Selective hydrogenation of phenol and related derivatives. *Catal*. *Sci*. *Technol*. **2014**, *4*, 3555–3569.

[57] Scirè, S.; Minicò, S.; Crisafulli, C. Selective hydrogenation of phenol to cyclohexanone over supported Pd and Pd-Ca catalysts: An investigation on the influence of different supports and Pd precursors. *Appl*. *Catal*. *A Gen*. **2002**, *235*, 21–31.

[58] Kong, X. Q.; Gong, Y. T.; Mao, S. J.; Wang, Y. Selective hydrogenation of phenol. *ChemNanoMat* **2018**, *4*, 432–450.

[59] Talukdar, A. K.; Bhattacharyya, K. G.; Sivasanker, S. Hydrogenation of phenol over supported platinum and palladium catalysts. *Appl*. *Catal*. *A Gen*. **1993**,

96, 229–239.

[60] Yang, X.; Yu, X.; Long, L. Z.; Wang, T. J.; Ma, L. L.; Wu, L. P.; Bai, Y.; Li, X. J.; Liao, S. J. Pt nanoparticles entrapped in titanate nanotubes (TNT) for phenol hydrogenation: The confinement effect of TNT. *Chem*. *Commun*. **2014**, *50*, 2794.

[61] Srinivas, S. T.; Kanta Rao, P. Synthesis, characterization and activity studies of carbon-supported platinum alloy catalysts. *J*. *Catal*. **1998**, *179*, 1–17.

[62] Giraldo, L.; Bastidas-Barranco, M.; Moreno-Piraján, J. C. Vapour phase hydrogenation of phenol over rhodium on SBA-15 and SBA-16. *Molecules* **2014**, *19*, 20594–20612.

[63] Martinez-Espinar, F.; Blondeau, P.; Nolis, P.; Chaudret, B.; Claver, C.; Castillón, S.; Godard, C. NHC-stabilised RH nanoparticles: Surface study and application in the catalytic hydrogenation of aromatic substrates. *J*. *Catal*. **2017**, *354*, 113–127.

[64] Rode, C. V.; Joshi, U. D.; Sato, O.; Shirai, M. Catalytic ring hydrogenation of phenol under supercritical carbon dioxide. *Chem*. *Commun*. **2003**, 1960–1961.

[65] Raut, A. N.; Nandanwar, S. U.; Suryawanshi, Y. R.; Chakraborty, M.; Jauhari, S.; Mukhopadhyay, S.; Shenoy, K. T.; Bajaj, H. C. Liquid phase selective hydrogenation of phenol to cyclohexanone over Ru/Al_2O_3 nanocatalyst under mild conditions. *Kinet*. *Catal*. **2016**, *57*, 39–46.

[66] Vinokurov, V.; Glotov, A.; Chudakov, Y.; Stavitskaya, A.; Ivanov, E.; Gushchin, P.; Zolotukhina, A.; Maximov, A.; Karakhanov, E.; Lvov, Y. Core/shell ruthenium–halloysite nanocatalysts for hydrogenation of phenol. *Ind*. *Eng*. *Chem*. *Res*. **2017**, *56*, 14043–14052.

[67] Raspolli Galletti, A. M.; Antonetti, C.; Giaiacopi, S.; Piccolo, O.; Venezia, A. M. Innovative process for the synthesis of nanostructured ruthenium catalysts and their catalytic performance. *Top*. *Catal*. **2009**, *52*, 1065–1069.

[68] Raspolli Galletti, A. M.; Antonetti, C.; Longo, I.; Capannelli, G.; Venezia, A. M. A novel microwave-assisted process for the synthesis of nanostructured ruthenium catalysts active in the hydrogenation of phenol to cyclohexanone. *Appl*. *Catal*. *A Gen*. **2008**, *350*, 46–52.

[69] Zhang, H. W.; Han, A. J.; Okumura, K.; Zhong, L. X.; Li, S. Z.; Jaenicke, S.; Chuah, G. K. Selective hydrogenation of phenol to cyclohexanone by SiO_2-supported rhodium nanoparticles under mild conditions. *J. Catal*. **2018**, *364*, 354–365.

WORKS CITED IN TABLE 4.2

[12] Raspolli Galletti, A. M.; Antonetti, C.; Giaiacopi, S.; Piccolo, O.; Venezia, A. M. Innovative process for the synthesis of nanostructured ruthenium catalysts and their catalytic performance. *Top. Catal.* **2009,** *52*, 1065-1069.

[13] Ertas, I. E.; Gulcan, M.; Bulut, A.; Yurderi, M.; Zahmakiran, M. Metal-organic framework (mil-101) stabilized ruthenium nanoparticles: Highly efficient catalytic material in the phenol hydrogenation. *Microporous Mesoporous Mater.* **2016,** *226*, 94-103.

[14] Wang, Y.; Yao, J.; Li, H.; Su, D.; Antonietti, M. Highly selective hydrogenation of phenol and derivatives over a pd@carbon nitride catalyst in aqueous media. *J. Am. Chem. Soc.* **2011,** *133*, 2362-2365.

[15] Scirè, S.; Minicò, S.; Crisafulli, C. Selective hydrogenation of phenol to cyclohexanone over supported Pd and Pd-ca catalysts: An investigation on the influence of different supports and Pd precursors. *Appl. Catal., A* **2002,** *235*, 21-31.

[16] Raspolli Galletti, A. M.; Antonetti, C.; Longo, I.; Capannelli, G.; Venezia, A. M. A novel microwave-assisted process for the synthesis of nanostructured ruthenium catalysts active in the hydrogenation of phenol to cyclohexanone☆. *Appl. Catal., A* **2008,** *350*, 46-52.

[17] Zhao, M.; Shi, J.; Hou, Z. Selective hydrogenation of phenol to cyclohexanone in water over Pd catalysts supported on amberlyst-45. *Chin. J. Catal.* **2016,** *37*, 234-239.

[18] Ertas, I. E.; Gulcan, M.; Bulut, A.; Yurderi, M.; Zahmakiran, M. Rhodium nanoparticles stabilized by sulfonic acid functionalized metal-organic framework for the selective hydrogenation of phenol to cyclohexanone. *J. Mol. Catal. A: Chem.* **2015,** *410*, 209-220.

[19] Liu, H.; Li, Y.; Luque, R.; Jiang, H. A tuneable bifunctional water-compatible heterogeneous catalyst for the selective aqueous hydrogenation of phenols. *Adv. Synth. Catal.* **2011,** *353*, 3107-3113.

[20] Patil, R. D.; Sasson, Y. Selective transfer hydrogenation of phenol to cyclohexanone on supported palladium catalyst using potassium formate as hydrogen source under open atmosphere. *Appl. Catal., A* **2015,** *499*, 227-231.

[21] Kuklin, S.; Maximov, A.; Zolotukhina, A.; Karakhanov, E. New approach for highly selective hydrogenation of phenol to cyclohexanone: Combination of rhodium nanoparticles and cyclodextrins. *Catal. Commun.* **2016,** *73*, 63-68.

[22] Liu, H.; Jiang, T.; Han, B.; Liang, S.; Zhou, Y. Selective phenol hydrogenation to cyclohexanone over a dual supported Pd–Lewis acid catalyst. *Science* **2009,** *326*, 1250.

[23] Fehn, S.; Zaheer, M.; Denner, C. E.; Friedrich, M.; Kempe, R. Robustly supported rhodium nanoclusters: Synthesis and application in selective hydrogenation of lignin-derived phenolic compounds. *New J. Chem.* **2016,** *40*, 9252-9256.

[24] Zhang, Z.; Ding, L.; Gu, J.; Li, Y.; Xue, N.; Peng, L.; Zhu, Y.; Ding, W. 3d

charged grid induces a high-performance catalyst: Ruthenium clusters enclosed in x-zeolite for hydrogenation of phenol to cyclohexanone. *Catalysis Science & Technology* **2017,** *7*, 5953-5963.

[25] Xu, G.; Guo, J.; Zhang, Y.; Fu, Y.; Chen, J.; Ma, L.; Guo, Q. Selective hydrogenation of phenol to cyclohexanone over Pd-hap catalyst in aqueous media. *ChemCatChem* **2015,** *7*, 2485-2492.

[26] Yang, X.; Yu, X.; Long, L.; Wang, T.; Ma, L.; Wu, L.; Bai, Y.; Li, X.; Liao, S. Pt nanoparticles entrapped in titanate nanotubes (tnt) for phenol hydrogenation: The confinement effect of tnt. *Chem. Commun.* **2014,** *50*, 2794.

[27] Zhang, H.; Han, A.; Okumura, K.; Zhong, L.; Li, S.; Jaenicke, S.; Chuah, G.-K. Selective hydrogenation of phenol to cyclohexanone by sio2-supported rhodium nanoparticles under mild conditions. *J. Catal.* **2018,** *364*, 354-365.

[28] Xiang, Y.; Kong, L.; Xie, P.; Xu, T.; Wang, J.; Li, X. Carbon nanotubes and activated carbons supported catalysts for phenol in situ hydrogenation: Hydrophobic/hydrophilic effect. *Ind. Eng. Chem. Res.* **2014,** *53*, 2197-2203.

[29] Li, F.; Cao, B.; Zhu, W.; Song, H.; Wang, K.; Li, C. Hydrogenation of phenol over pt/cnts: The effects of pt loading and reaction solvents. *Catalysts* **2017,** *7*, 145.

CHAPTER 5: ULTRASOUND-MEDIATED SYNTHESIS OF FLUORITE-STRUCTURED HIGH-ENTROPY OXIDE NANOCATALYSTS FOR EFFICIENT CO OXIDATION

5.1 Publication disclosure

This chapter is based on a prepared manuscript recently submitted to *iScience*: Okejiri, F.; Yang, Z.; Fan, J.; Wang, T.; Suo, X.; Dai, S.

My contributions to this work include identification of the research objectives, searching of relevant literature, design and conducting of the synthetic experiments, characterization of the samples, drafting of the manuscript with reviews and edits from all listed authors.

5.2 Abstract

High-entropy oxides (HEOs) are an emerging class of advanced ceramic materials with great technological prospects. Herein, we report a facile synthesis of single-phase, fluorite-structured HEO ($CeHfZrSnErO_x$) nanocrystals via an ultrasound-mediated coprecipitation strategy in ambient conditions. Characterization results reveal ultrasmall nanocrystals with high surface area and high-oxygen vacancy concentration. Upon introducing palladium to $CeHfZrSnErO_x$, the resultant $Pd/CeHfZrSnErO_x$ displays high dispersion of Pd nanoclusters and atomically dispersed palladium species. Compared to Pd/CeO_2 of similar Pd loading, $Pd/CeHfZrSnErO_x$ exhibits superior catalytic performance towards CO oxidation, highlighting the inherent advantage of $CeHfZrSnErO_x$ as

carrier support over traditional oxide systems. The determined apparent activation energy values are consistent with the activity trend of the catalysts. This technologically feasible, scalable, and facile synthetic strategy hold great promises towards the synthesis of HEO systems of other crystal structures and functional features.

5.3 Introduction

At the turn of the new millennium, a new class of multi-principal-element materials with high configuration was discovered called high-entropy alloys (HEAs).[1-3] HEAs are a unique class of concentrated solid-solution alloys formed on the premise of incorporating five or more principal elements into a single crystal lattice.[2,3] This fundamentally new alloying strategy provided new traction to material design, leading to the discovery of materials with intriguing synergistic properties, unexpected characteristics, and interesting new functionalities.[4-7] Within the past six years, the 'high-entropy concept' has expanded beyond metallic alloys, to include high-entropy nitrides,[8] high-entropy borides,[9] high-entropy silicides,[10] high-entropy carbides,[11] and, the more widely studied, high-entropy oxides (HEOs).[12-15]

The use of configuration entropy in the stabilization of new oxide phases, similar to situations in HEAs, was first demonstrated by Rost et al. who synthesized a HEO system of the rock-salt crystal structure via the solid-state synthesis method.[12] More recent studies have explored HEO systems of different crystalline

structures and functional features, including perovskite oxides,[16] pyrochlores,[17] spinel oxides,[18] fluorite-structured oxides,[19] etc.

Compared to metallic HEAs of simple face-centered cubic (fcc), body-centered cubic (bcc), or hexagonal close-packed (hcp) crystal structure, single-phase HEO systems are generally more difficult to yield because of their larger enthalpy of formation.[19] It should be mentioned that the solid-state synthesis route, as implemented by Rost et al., required high-energy ball milling of the metal precursors in addition to heat treatment at 1000 °C to obtain the desired HEO.[12] Gild et al. and Chen et al. have applied a similar strategy towards the synthesis of single-phase HEOs of fluorite crystal structure.[14,15] However, the rigorous synthetic conditions, including the ultra-high temperature (1500 –1800 °C) and extended reaction times (6–24 hours), constitute major synthetic challenges. Such extreme synthetic conditions typically result in micron-sized particles with a non-uniform size distribution. For most catalytic applications, non-agglomerated powders with high surface areas are preferred. More recently, Xu et al. succeeded in lowering the synthesis temperature to 900 °C,[19] which, unfortunately by many standards is still sufficiently high. Other promising strategies that have been reported include the reverse co-precipitation method,[20] co-precipitation and peptization,[13] hydrothermal synthesis methods,[21] and nebulized spray pyrolysis,[22] being limited by rigorous synthetic processes, multiple reaction procedures, energy-intensive unit operations, and highly specialized pieces of equipment, respectively. The development of technologically feasible, facile, and reliable synthetic strategies is still highly desirable.

Ultrasound can be used to drive high-energy chemical reactions via the physical process of acoustic cavitation. The acoustic cavitation phenomenon, which is described as the formation, growth, and implosive collapse of microbubbles in liquids under ultrasound irradiation, is generally accompanied by a release of massive energy (T ≈ 5000 °C) in a microscopic region at an extremely fast cooling rate (10 billion °C s^{-1}).[23] Recently, we exploited this unique high-energy environment towards the synthesis of nanosized HEA,[4,6] and high-entropy perovskite oxide nanocatalysts.[16] The present study seeks to investigate the feasibility of fabricating fluorite-structured HEO nanocatalyst using an ultrasound-mediated co-precipitation strategy. More specifically, synthesis of nanocrystalline $CeHfZrSnErO_x$ and $CeHfZrSnErO_x$-stabilized palladium catalysts with different Pd loadings ($Pd_{0.5}/CeHfZrSnErO_x$ and $Pd_{1.0}/CeHfZrSnErO_x$) was realized sonochemically at ambient conditions. This technologically feasible, facile, and scalable synthetic strategy holds great promise towards the synthesis of nanostructured HEO systems of other crystalline structures and functional features.

To understand the crystalline structure, chemical composition, and surface chemistry of the synthesized nanocatalysts, various characterization techniques, including X-ray diffraction (XRD), high-resolution transmission electron microscopy (HRTEM), energy-dispersive X-ray spectroscopy (EDS) mapping, X-ray photoelectron spectroscopy (XPS), diffuse reflectance infrared Fourier transform spectroscopy (DRIFTS) and inductively-coupled plasma optical emission spectroscopy (ICP-OES), were utilized. The catalytic activity of $Pd/CeHfZrSnErO_x$

was compared with Pd/CeO_2 of similar metal loading to underscore the inherent advantages of $CeHfZrSnErO_x$ as carrier support.

5.4 Experimental methods

First, the following selection guidelines as suggested by Rost et. and modified by Djenadic et al. were considered for the choice of the metal compositions to favor the formation of a single-phase HEO system: (i) cations of similar ionic radii are preferred over cations with profound ionic size mismatch; (ii) the possible binary oxides should not exhibit uniform crystal structure (iii) there should exist, at least, one binary oxide pair that does not exhibit complete solubility in the oxide binary phase diagram.[12,24] In the assessment of these, the following cations with comparable ionic were utilized as the metal precursor:[25] Ce^{3+}, Hf^{4+}, Zr^{4+}, Sn^{4+}, and Er^{3+}.

5.5 Materials

Cerium (III) chloride heptahydrate (99.9% $CeCl_3 \cdot 7H_2O$, Fischer chemicals, USA), hafnium (IV) chloride (99.0% $HfCl_4$, Alfa Aesar, USA), zirconium (IV) chloride (99.0% $ZrCl_4$, Sigma Aldrich, USA), tin (IV) chloride hydrate (98.0% $SnCl_4 \cdot xH_2O$, Alfa Aesar, USA), erbium (III) nitrate pentahydrate (99.9% $Er(NO_3)_3 \cdot 5H_2O$, Alfa Aesar, USA), sodium hydroxide (98.0% NaOH, Sigma Aldrich, USA), potassium tetrachloropalladate (II) (98.0% K_2PdCl_4, Fisher Chemicals, USA), and ethylene glycol (99.0% $HO\text{-}CH_2CH_2\text{-}OH$, Alfa Aesar, USA), were all used as received without further purification.

5.6 Material synthesis

$CeHfZrSnErO_x$

To synthesize $CeHfZrSnErO_x$, an aqueous solution of the metal precursors was prepared by dissolution of 1.0 mmol each of $CeCl_3 \cdot 7H_2O$, $HfCl_4$, $ZrCl_4$, $SnCl_4 \cdot xH_2O$, and $Er(NO_3)_3 \cdot 5H_2O$ in 10.0 mL deionized (DI) water. The precursors were added dropwise to a 30.0 mL of 5.0 M NaOH solution while simultaneously being exposed to ultrasound irradiation for 15 minutes via direct immersion of an ultrasonic titanic horn operating at 20 kHz at ambient conditions, as schematically shown in figure 5.1. The ultrasonic processor which has a maximum output of 750 watts was acquired from Sonics & Materials, INC. and equipped with a cylindrical probe of ¾ ″ diameter. The sonication was performed under the pulsed mode, and the amplitude was set at 50% amplitude. When the sonication time was reached, the solid was recovered via centrifugation, washed thoroughly with deionized (DI) water before being dried in an oven at 110 °C to obtain the final crystallites. $CeHfZrSnO_2$, $CeZrO_2$, $CeHfO_2$, $CeSnO_2$, and CeO_2 were also synthesized in a similar manner.

For the investigation of the entropic contribution to phase stability, the as-synthesized $CeHfZrSnErO_x$ was heated at different temperatures and rapidly air-quenched to preserve the crystal structure at the specific temperature.

$CeHfZrSnO_2$

To synthesize $CeHfZrSnO_2$, an aqueous solution of the metal precursors was prepared by dissolution of 1.25 mmol each of $CeCl_3 \cdot 7H_2O$, $HfCl_4$, $ZrCl_4$, and

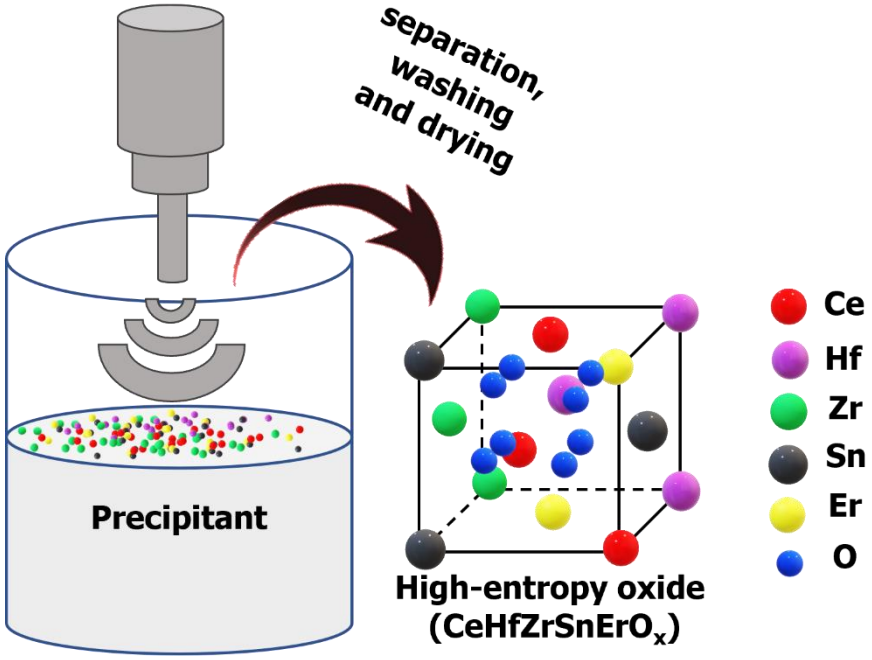

Figure 5.1. Schematic illustration of the synthesis of high-entropy oxide nanocatalysts via an ultrasound-mediated co-precipitation strategy.

$SnCl_4 \cdot xH_2O$ in 10.0 mL deionized (DI) water. The precursors were added dropwise to a solution of NaOH while simultaneously being exposed to ultrasound irradiation for 15 minutes via direct immersion of an ultrasonic titanic horn operating at 20 kHz at ambient conditions. When the sonication time was reached, the solid was recovered via centrifugation, washed thoroughly with DI water before being dried in an oven at 110 °C to obtain the final crystallites.

$CeHfO_2$

To synthesize $CeHfO_2$, an aqueous solution of the metal precursors was prepared by dissolution of 2.5 mmol each of $CeCl_3 \cdot 7H_2O$ and $HfCl_4$ in 10.0 mL deionized (DI) water. The precursors were added dropwise to a solution of NaOH while simultaneously being exposed to ultrasound irradiation for 15 minutes via direct immersion of an ultrasonic titanic horn operating at 20 kHz at ambient conditions. When the sonication time was reached, the solid was recovered via centrifugation, washed thoroughly with DI water before being dried in an oven at 110 °C to obtain the final crystallites.

$CeZrO_2$

To synthesize $CeZrO_2$, an aqueous solution of the metal precursors was prepared by dissolution of 2.5 mmol each of $CeCl_3 \cdot 7H_2O$ and $ZrCl_4$ in 10.0 mL deionized (DI) water. The precursors were added dropwise to a solution of NaOH while simultaneously being exposed to ultrasound irradiation for 15 minutes via direct immersion of an ultrasonic titanic horn operating at 20 kHz at ambient conditions. When the sonication time was reached, the solid was recovered via

centrifugation, washed thoroughly with DI water before being dried in an oven at 110 °C to obtain the final crystallites.

$CeSnO_2$

To synthesize $CeSnO_2$, an aqueous solution of the metal precursors was prepared by dissolution of 2.5 mmol each of $CeCl_3 \cdot 7H_2O$ and $SnCl_4 \cdot xH_2O$ in 10.0 mL deionized (DI) water. The precursors were added dropwise to a solution of NaOH while simultaneously being exposed to ultrasound irradiation for 15 minutes via direct immersion of an ultrasonic titanic horn operating at 20 kHz at ambient conditions. When the sonication time was reached, the solid was recovered via centrifugation, washed thoroughly with DI water before being dried in an oven at 110 °C to obtain the final crystallites.

CeO_2

To synthesize $CeSnO_2$, an aqueous solution of the metal precursors was prepared by dissolution of 5.0 mmol of $CeCl_3 \cdot 7H_2O$ in 10.0 mL deionized (DI) water. The precursors were added dropwise to a solution of NaOH while simultaneously being exposed to ultrasound irradiation for 15 minutes via direct immersion of an ultrasonic titanic horn operating at 20 kHz at ambient conditions. When the sonication time was reached, the solid was recovered via centrifugation, washed thoroughly with DI water before being dried in an oven at 110 °C to obtain the final crystallites.

Pd/CeHfZrSnErO$_x$

To synthesize Pd/CeHfZrSnErO$_x$, an alcoholic solution the Pd precursor was prepared by dissolution 0.025 mmol of K_2PdCl_4 in 5.0 mL ethylene glycol. This solution was combined with a calculated mass of the as-synthesized CeHfZrSnErO$_x$ pre-dispersed in 30.0 mL ethylene glycol for a final Pd mass loading of 0.5 or 1.0 wt.% (referred to as $Pd_{0.5}$/CeHfZrSnErO$_x$ and $Pd_{1.0}$/CeHfZrSnErO$_x$, respectively). This mixture was quickly exposed to ultrasound irradiation for 10 minutes via direct immersion of ultrasonic titanic horn operating at 20 kHz at ambient conditions. When the sonication time was reached, the solid was recovered via centrifugation, washed thoroughly with DI water and ethanol before being dried in an oven at 90 °C to obtain CeHfZrSnErO$_x$-stabilized palladium nanoclusters (Pd/CeHfZrSnErO$_x$) as the final crystallite. $Pd_{1.0}$/CeHfZrSnErO$_x$ was chosen as the representative sample for characterization purposes except otherwise indicated. Also, Pd/CeO_2 with 1.0 wt.% Pd was synthesized in a similar manner.

Pd/CeO_2

To synthesize Pd/CeO_2, an alcoholic solution the Pd precursor was prepared by dissolution 0.025 mmol of K_2PdCl_4 in 5.0 mL ethylene glycol. This solution was combined with a calculated mass of the as-synthesized CeO_2 support pre-dispersed in 30.0 mL ethylene glycol for a final Pd mass loading of 1.0 wt.%. This mixture was quickly exposed to ultrasound irradiation for 10 minutes via direct immersion of ultrasonic titanic horn operating at 20 kHz at ambient conditions. When the sonication time was reached, the solid was recovered via centrifugation,

washed thoroughly with DI water and ethanol before being dried in an oven at 90 °C to obtain CeO_2 as the final crystallite.

5.7 Characterization techniques

To determine the crystallographic structure of the materials, the X-ray diffraction (XRD) technique was employed. XRD patterns were acquired on a PANalytical Empyrean diffractometer with Cu Kα1 radiation (λ = 1.5406 Å), operated at 45 kV and 40 mA. The 2θ range angles were scanned between 20° to 90° at a step size of 0.05°. The crystallite size and microstrain contributions to peak broadening were assessed by Williamson–Hall (W–H) analysis.[26] The instrumental broadening effect was taken into account in the measurement of the full width at half maximum intensity (FWHM). A silicon standard sample was used to apply a correction for the instrumental broadening. The W-H analysis assumes that the crystallite size and microstrain contributions are mutually independent of each other and is given by equation 5.1:

$$\beta\cos\theta = \frac{K\lambda}{D} + 4\varepsilon\sin\theta \qquad eqn\ 5.1$$

where β is the FWHM in radians, θ is the scattered angle measured in degrees, k is the shape factor (0.9), λ is the wavelength of the X-ray (0.15406 nm), *D* and *ε* represent the crystallite size and microstrain, respectively. By plotting a graph of βcosθ against 4sinθ, the microstrain and average crystallite size were estimated by the slope of the line and y-intercept extrapolation, respectively. The interplanar spacings were determined by Bragg's law using MDI JADE 6.5 software. The

lattice parameter, a_0 was calculated from equation 5.2 after indexing the hkl values for each of the diffraction peaks.

$$d_{hkl} = \frac{a_o}{\sqrt{(h^2 + k^2 + l^2)}} \qquad eqn\ 5.2$$

The specific surface area of samples was determined by low-temperature (77 K) nitrogen adsorption performed on Gemini 2375 surface area analyzer. Prior to analysis, samples were degassed for 6 hours in a drying compartment under N_2 at 160 °C to eliminate any adsorbed species. Surface area analysis was performed by applying the Brunauer, Emmett, and Teller (BET) theory. Pore size distributions were calculated from the adsorption isotherm using Barrett–Joyner–Halenda (BJH) method.

High-resolution transmission electron microscopy (HRTEM) images and the energy-dispersive X-ray spectroscopy (EDS) mapping images were recorded on Hitachi H-7700 microscope with an acceleration voltage of 100 kV.

Diffuse reflectance infrared Fourier transform spectroscopy (DRIFTS) spectra were acquired on Thermo Nicolet Nexus 670 FTIR spectrometer equipped with a mercury cadmium telluride (MCT) detector and Pike Technologies diffuse reflectance cell. Each spectrum was recorded with 32 scans at a resolution of 4 cm^{-1}. In a typical run, the sample was loaded into a ceramic cup located in the DRIFTS cell and preheated at 400 °C for 30 minutes under a constant flow of 5% O_2/Ar gas (flow rate ≈ 30 mL/min). Next, Ar was passed through the sample and the temperature was taken down to 30 °C for background collection. Thereafter, CO was adsorbed for 10 minutes at 30 °C, followed by desorption for 10 minutes

at 30 °C. Spectra were collected during the adsorption-desorption process and transformed into Kubelka-Munk form.

X-ray photoelectron spectroscopy (XPS) spectra were recorded on Thermo Scientific Model K-Alpha S5 X-ray Photoelectron Spectrometer System using Al Kα (1486.6 eV photons) as the radiation source. The instrument uses a hemispherical electron energy analyzer equipped with a 128-channel electron detection system. Samples were prepared for analysis by dispersing the powder material onto a double-sided tape fixed to a clean glass slide. After inserting the sample into the analysis chamber through a vacuum-pumped load-lock, an initial wide energy range survey scan was acquired. Next, a set of narrow energy range core level spectra were acquired for the elements of interest. The C 1s peak (284.6 eV) was used for the calibration.

The relative metal concentrations were determined by inductively coupled plasma optical emission spectroscopy (ICP-OES) analysis performed on an Agilent 5110 ICP-OES spectrometer. Prior to analysis, samples were digested in aqua regia and diluted with 2.0% nitric acid.

The catalytic CO oxidation experiment was performed in a fixed-bed reactor at atmospheric pressure conditions according to previous reports.[16,27] The reactor is made of quartz tubing with an inner diameter of approximately 4 mm. The gas flow rate was controlled with a mass-flow controller. For the measurement of CO light-off curves showing CO conversion as a function of reaction temperature, 20 mg of the catalyst was charged into the reactor and supported with a ball of quartz wool. A feed gas of 1% CO balanced with dry air was passed through the catalysts

bed at a flow rate of 12.5 mL/min, corresponding to a gas hourly space velocity (GHSV) of 37,500 mL (h g_{cat})$^{-1}$. The concentrations of CO_2 and CO in the reactor effluent were analyzed using an on-line gas chromatograph (Buck Scientific 910) equipped with a dual molecular sieve/porous polymer column (Alltech CTR1) and a thermal conductivity detector (TCD). The conversion, $C_{CO}(\%)$ was calculated according to the following equation:

$$C_{CO}(\%) = \frac{[CO]_{inl} - [CO]_{out}}{[CO]_{inl}} \times 100 \qquad eqn\ 5.3$$

The steady-state experiment was performed in the same reactor when the CO conversion was below 15.0 % to ensure that the reaction was close to under kinetic control as possible. The rate constant, *K* was determined according to the following equation:

$$K = \frac{R_t \times C_{co}}{m_{cat}} \qquad eqn\ 5.4$$

where R_t (mL.s^{-1}) is the total gas flow rate, C_{CO} is the CO conversion (%) at temperature T(K), and m_{cat} is the mass (g) of the catalysts in the reactor. The apparent activation energy, (E_a) was estimated from the slope of the linear plot of $\ln(K)$ versus 1000/T according to the non-exponential Arrhenius equation given below:

$$\ln(K) = \ln(A) - \frac{E_a}{R}\left(\frac{1}{T}\right) \qquad eqn\ 5.5$$

where *K* (s^{-1}) and A (s^{-1}) represent the rate constant and pre-exponential factor, respectively; E_a (kJ mol^{-1}) is the apparent activation energy, R is the gas constant, 8.314 J mol^{-1} K^{-1}; and T(K) is the kelvin temperature.

5.8 Results and discussion

To sonochemically synthesize $CeHfZrSnErO_x$, an aqueous solution of the metal precursors was added to a precipitating agent and instantaneously exposed to ultrasound irradiation for 15 minutes. Following the separation and drying processes, $CeHfZrSnErO_x$ was obtained as a crystalline powder without calcination. $CeHfZrSnErO_x$-stabilized palladium nanoclusters ($Pd/CeHfZrSnErO_x$) was synthesized by adding an alcoholic solution of a palladium precursor to pre-synthesized $CeHfZrSnErO_x$ under ultrasound exposure for 10 minutes. XRD technique was employed for phase identification. Figure 5.2 (a) displays the XRD patterns of $CeHfZrSnErO_x$ and CeO_2. The diffraction peaks of $CeHfZrSnErO_x$ are centered at 29.87, 34.60, 49.62, 58.86, 61.75, and 72.57° and can be indexed to (111), (200), 220), (311), (222), and (400) planes, respectively of a cubic fluorite structure. Compared to the diffraction pattern of CeO_2, these characteristic reflections are located at slightly higher 2-theta angles (inset in figure 5.2 (a)), suggesting a unique set of lattice parameters smaller than that of CeO_2. This shrinkage in the lattice parameter, from 5.4111 Å to 5.1911 Å, is consistent with the diffusion of the smaller-sized cations (Hf^{4+}, Zr^{4+}, $Sn^{4+}$and Er^{3}) into the base CeO_2 crystal lattice to form $CeHfZrSnErO_x$ as a new single-phase HEO material.

Notably, the peaks are sufficiently broad which generally suggests small crystallite size, microstrain, sample inhomogeneity, or instrumental effects.[28] But since the sample is compositionally homogeneous (demonstrated later by the EDS mapping), the crystallite size and microstrain contributions to peak broadening

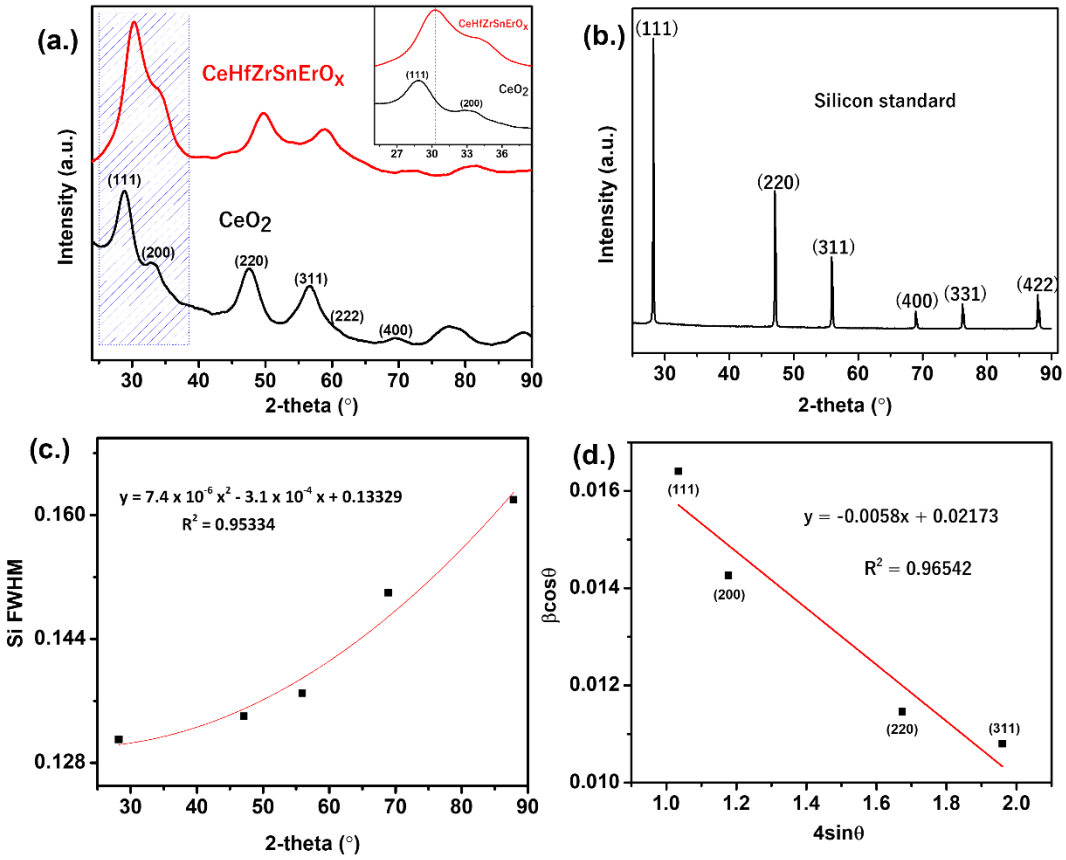

Figure 5.2. (a) XRD patterns $CeHfZrSnErO_x$ and CeO_2 (the shift in reflection positions of $CeHfZrSnErO_x$ relative to CeO_2 is denoted by the dotted lines in the inset); (b) XRD pattern of a silicon standard; (c) a plot of the Si FWHM versus the reflection angles; (d) W-H plot of βcosθ against 4sinθ after correcting for instrumental broadening.

were assessed by the W-H method after correcting for instrumental broadening (figure 5.2(b)). Figure 5.2 (c) displays the broadening in FWHM against 2-theta values obtained for the standard Si sample. A polynomial fitting of the experimentally observed values was made using the quadratic function in equation 5.6:

$$y = ax^2 + bx + c \qquad eqn\ 5.6$$

where y is the broadening (FWHM), x is the 2-theta angle (°), a, b, and c are constants determined as 7.4 x $^{-6}$, -3.1 x 10^{-4}, and 0.13329, respectively.

Figure 5.2 (d) displays the plot of βcosθ against 4sinθ. The negative slope of the fitted line in the W-H plot is indicative of compressional strain and is consistent with the contraction of the lattice parameter. The estimated slope and hence the value of the microstrain is -0.0058, while the determined crystallite size is 6.3 nm. On the basis of these analyses, we conclude that the peak broadness is mainly due to the small crystallite size.

HRTEM images were acquired to gain additional structural information. Figure 5.3 (a) displays the HRTEM image of the as-obtained $CeHfZrSnErO_x$ nanocrystal. The well-defined lattice fringes indicate high crystallinity. The interplanar spacings between lattice fringes were measured to be ~0.30 nm and 0.26 nm, corresponding to the (111) and (200) planes of a cubic fluorite lattice. The corresponding SAED pattern exhibits a continuous ring pattern, indicating its polycrystalline nature. The radial intensity line profile as a function of distance in the reciprocal lattice is shown in figure 5.3 (b). The interplanar spacings are

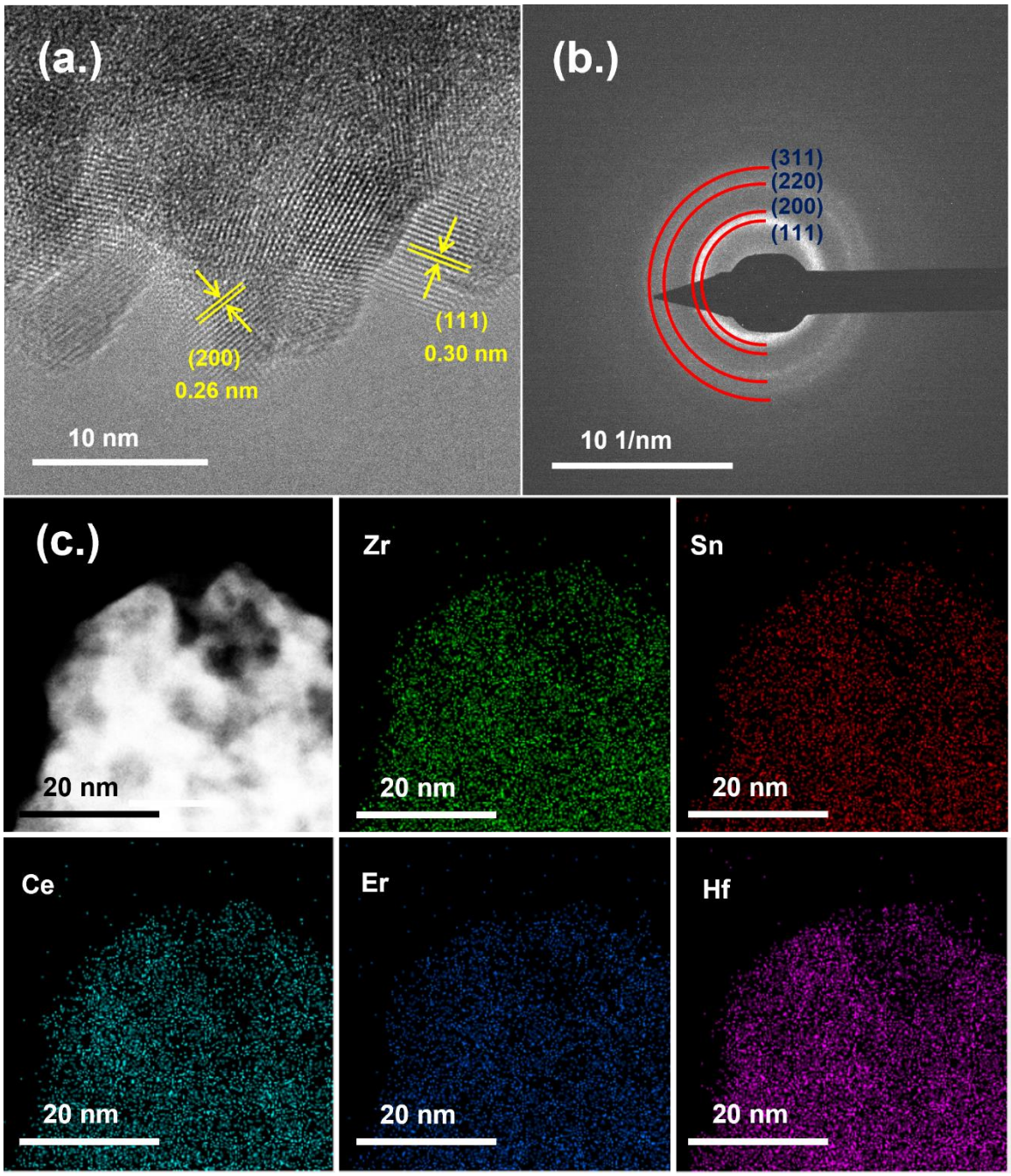

Figure 5.3. Structural characterization of CeHfZrSnErOx (a) HRTEM image (b) the corresponding SAED (c) EDX maps for $CeHfZrSnErO_x$ showing Zr, Sn, Ce, Er and Hf elements**.**

consistent with the values obtained from the XRD pattern and can be indexed to (111), (200), (220), and (311) planes of a cubic fluorite structure. Figure 5.3 (c) displays the EDS elemental map of $CeHfZrSnErO_x$. The uniform distribution Ce, Hf, Zr, Sn, Er, and O in the nanosphere validate the formation of a single-phase HEO solid-solid. To demonstrate uniformity, the EDS elemental map of a different area of the sample was examined. The result (Figure 5.4) indicates that $CeHfZrSnErO_x$ is both chemically and structurally uniform.

The relative concentrations of the cations were determined by ICP-OES analysis. The atomic percentages of Ce, Hf, Zr, Sn, and Er in the sample were determined to be 3.81, 3.73, 3.68, 3.72, and 3.71, respectively, which are consistent with the theoretical concentrations in the precursor solution. The slight deviation from equimolar stoichiometric ratios is probably due to the differences in the purity of the metal precursors.

The low-temperature N_2 adsorption isotherm and the corresponding pore size distribution of $CeHfZrSnErO_x$ are displayed in figure 5.5. $CeHfZrSnErO_x$ exhibits a relatively high surface area (87 m^2g^{-1}) and a narrow pore size (5 nm) distribution which makes it a suitable candidate for the dispersion of active metal catalysts.

To understand the surface chemistry, XPS technique was employed. Figure 5.6 displays the XPS survey spectrum of $CeHfZrSnErO_x$, showing photoemission signals for Ce, Hf, Zr, Sn, Er, and O as expected. To gain insight into their oxidation states, the core-level spectra of Ce 3d, Hf 4f, Zr 3p, Sn 3d, Er 4d, and O 1s (figure

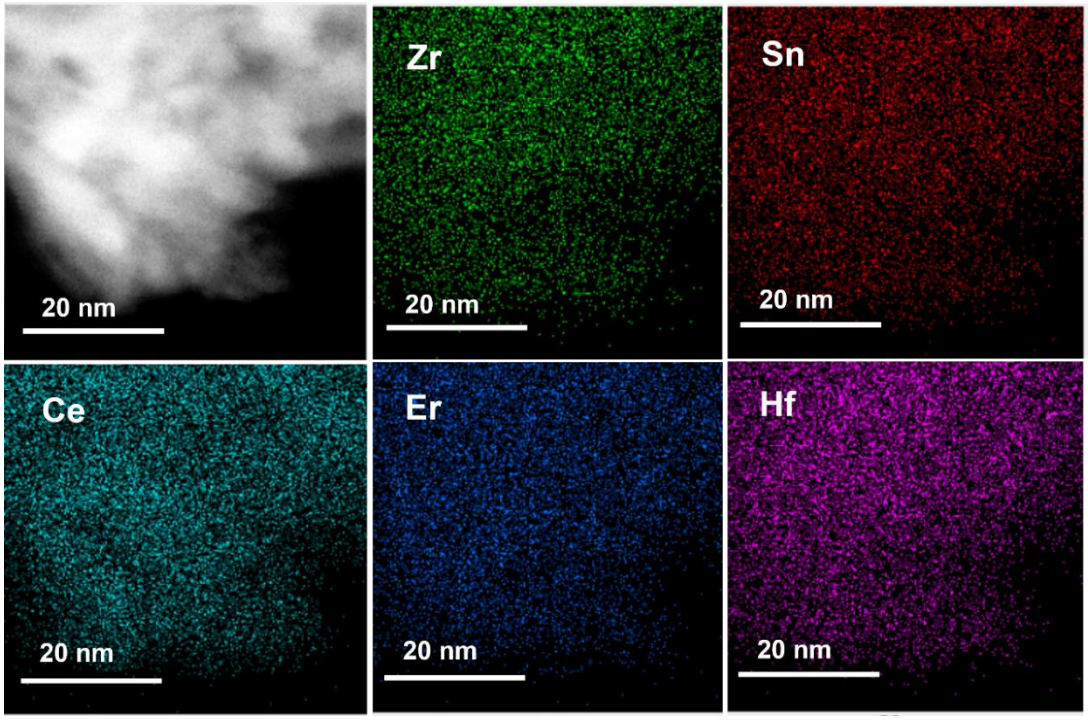

Figure 5.4. HAADF STEM image and EDX elemental maps of $CeHfZrSnErO_x$ showing Zr, Sn, Ce, Er, and Hf elements.

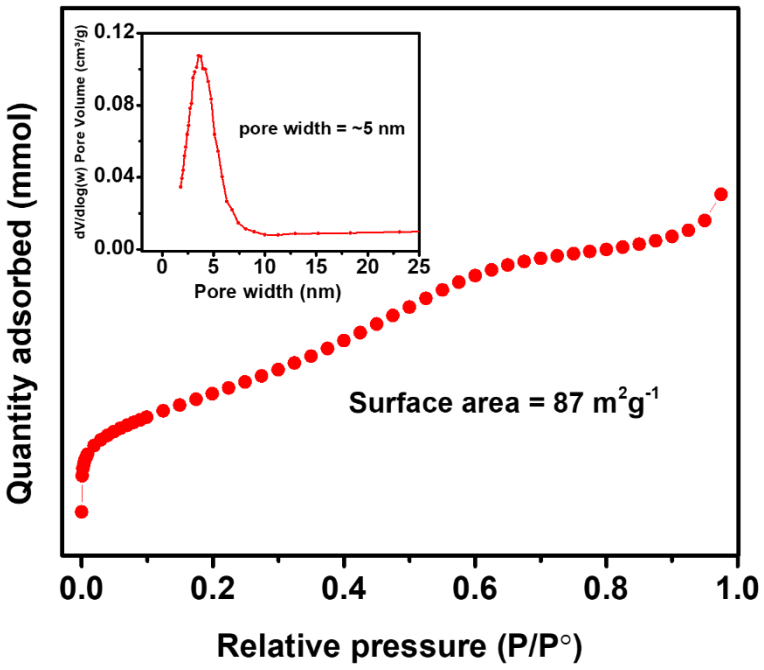

Figure 5.5. N_2 adsorption isotherm of CeHfZrSnErOx and the corresponding pore size distribution (inset).

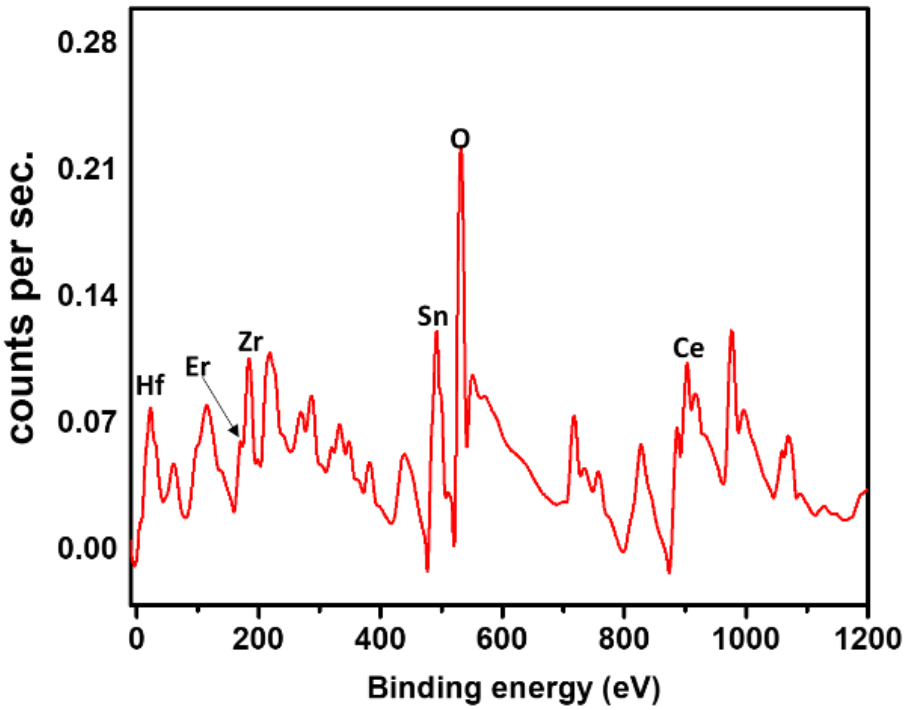

Figure 5.6. XPS survey spectrum of CeHfZrSnErOx, showing photoemission signals for Ce, Hf, Zr, Sn, Er, and O.

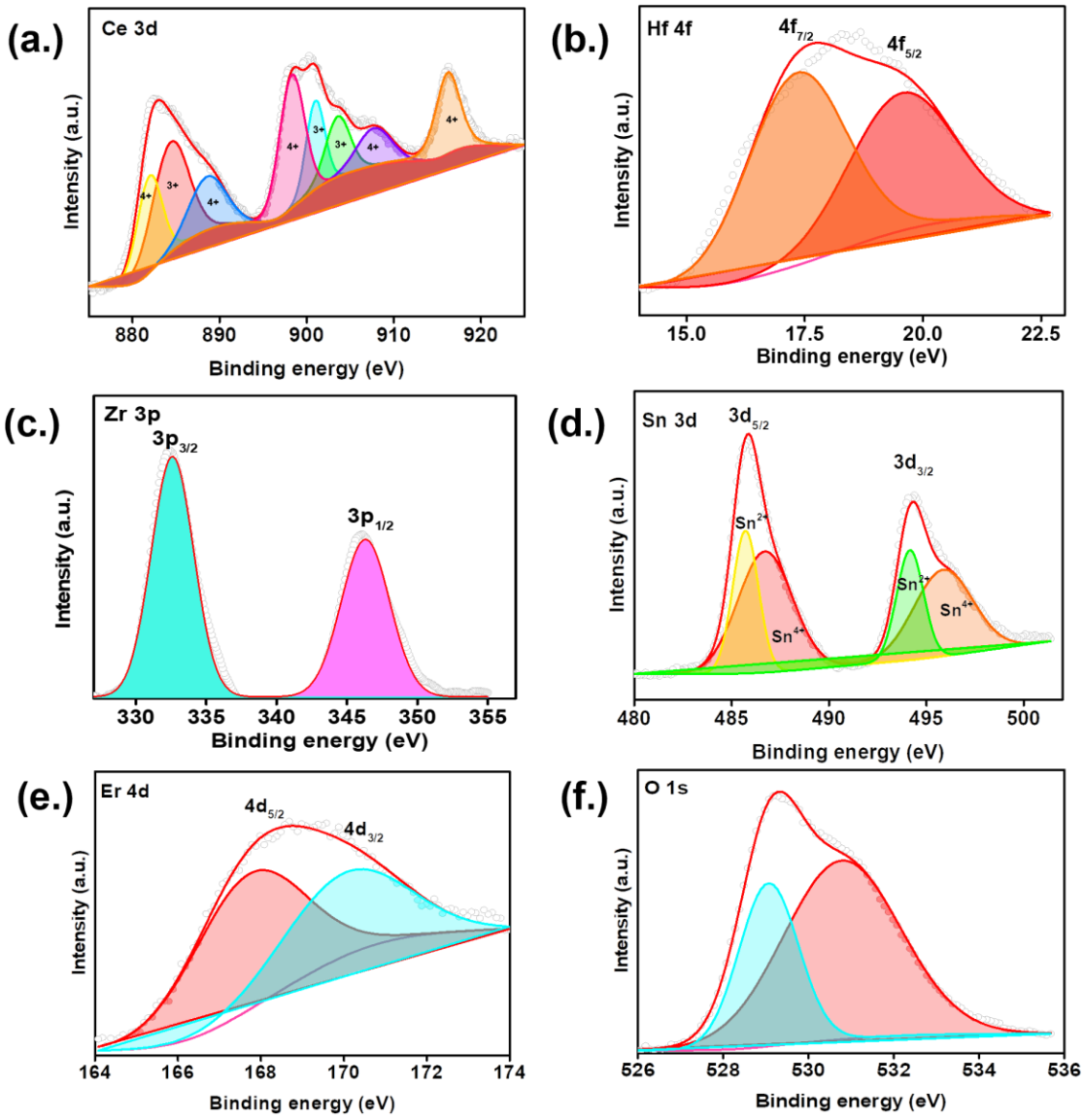

Figure 5.7. Core-level XPS spectra of: (a) Ce 3d, (b) Hf 4f, (c) Zr 3p, (d) Sn 3d, (e) Er 4d, and (f) O 1s.

5.7) were acquired. For the Ce 3d XPS spectrum, eight peaks resulting from the pairs of spin-orbit doublets were identified through deconvolution. The five peaks centered at approximately 883, 888, 898, 907, and 916 eV are assigned to Ce^{4+} species, while the three peaks around 885, 901, and 901 eV are assigned to Ce^{3+} species.[29,30]. The Hf 4f peak overlapped with a Ce 5p peak at ~19 eV. Peak fitting reveals that the Hf $4f_{7/2}$ is centered at 16.5 eV and is normally attributed with Hf in the +4 oxidation state.[31] The Zr 3p spectrum contains two peaks with binding energies around 332 and 346 eV, characteristic of Zr^{+4} species.[32,33] For the Sn 3d spectrum, four peaks were identified resulting from pairs of spin-orbit doublets. Two peaks centered at approximately 488 and 496 eV are assigned to Sn^{4+} species, while the ones around 486 and 494 eV are attributed to Sn^{2+}species.[34,35] The Er photoelectron signal indicates that Erbium is unquestionably present in the sample's surface. However, the Er 4d peak overlapped with the Zr 3d signal. The peak fitting process is quite ambiguously given that the Er 4d photoelectron region consists of a complex mixture of doublets and satellite peaks not reliably identified at this point. Nevertheless, the approximate position of the Er 4d peak is consistent with the position of Er_2O_3 reported by Swami et al.[36] The O 1s spectrum shows two peaks corresponding to two kinds of oxygen species. The strong peak at 529 eV is ascribed to the lattice oxygen, as in O-M (where M = Ce^{4+}, Ce^{3+} Hf^{4+}, Zr^{4+}, Sn^{4+}, and Er^{3+}); the other portion of the deconvoluted peak centered at 531 eV is attributed to oxygen vacancy.[37] Overall, the surface features of $CeHfZrSnErO_x$ are dominated by Ce^{4+}, Ce^{3+} Hf^{4+}, Zr^{4+}, Sn^{4+}, Sn^{2+}, $Er^{3+,}$ and $O^{\delta-}$ species. The existence of Ce^{3+}, Sn^{2+} and Er^{3+} suggests high surface oxygen vacancy

concentration, which benefits reactant activation and conversion is catalytic CO oxidation.[38]

As is well known, composition and temperature dependence of phase stability is both enthalpy- (H) and entropy (S)-driven, according to Gibb's free equation: $\Delta G = \Delta H - T\Delta S$. To investigate the entropic contribution to phase stability, we performed a four-stage heat-treatment process on the same sample, at various temperatures, followed by rapid air-quenching to preserve the crystalline phase at the specific temperature. Previous studies have demonstrated that phase reversibility is a requirement of entropy-driven stability.[12,21] We anticipate that $CeHfZrSnErO_x$ should reversibly transform between high-temperature single-phase to low-temperature multiphase if, indeed, entropy-stabilized.[12] Figure 5.8 displays the XRD patterns of the same sample heated at various temperatures: initial treatment at 900 °C, a second treatment at 700 °C, third treatment at 800 °C, and final return to 900 °C. It is evident from the XRD patterns that heat treatment at either temperature did not result in phase segregation which is in disagreement with phase-transition thresholds (850 – 900 °C) reported by Rost et al. for their rock-salt-structured HEO.[12] Phase segregation has been reported for fluorite-structured HEOs at 1100 °C and a complete reversal to single at temperatures above 1500 °C, highlighting their larger positive enthalpy of formation (relative to rock-salt-structured),[14, 21] and additionally, underscores the uniqueness of the high-energy environment under acoustic cavitation. Meanwhile, fluorite-structured multicomponent oxides, including $CeHfZrSnO_2$, $CeHfO_2$ $CeZrO_2$, and $CeSnO_2$, synthesized under similar reaction conditions as $CeHfZrSnErO_x$ behaved similarly

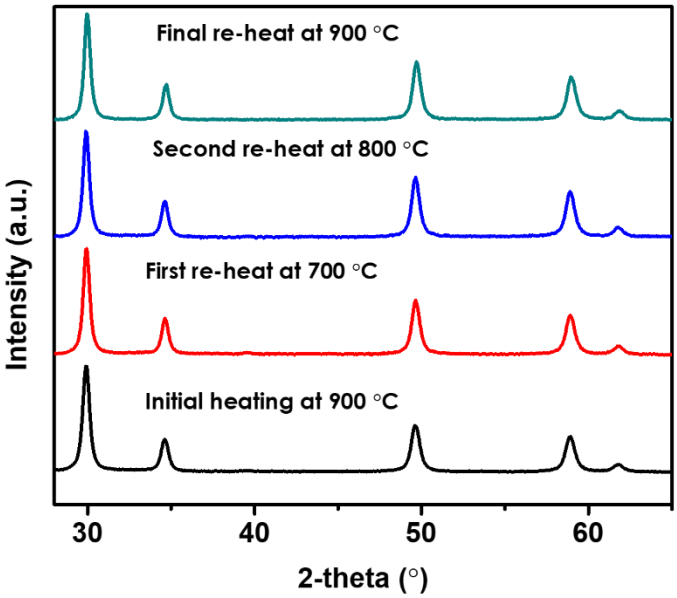

Figure 5.8. XRD patterns of the same sample ($CeHfZrSnErO_x$) heated at various temperatures: initial treatment at 900 °C, a second treatment at 700 °C, third treatment at 800 °C, and final return to 900 °C.

under the same treatment conditions, suggesting that configuration entropy is likely not the main contributing factor for phase stability in $CeHfZrSnErO_x$, for at least temperatures below 900 °C.

Upon introducing 0.5 – 1.0 wt % Pd to $CeHfZrSnErO_x$, the diffraction pattern of the resultant $CeHfZrSnErO_x$-stabilized palladium nanoclusters ($Pd/CeHfZrSnErO_x$), like $CeHfZrSnErO_x$, displayed only diffraction peaks indexed to the cubic fluorite structure with no additional peak attributed to Pd or PdO species. However, the characteristic reflections (see figure 5.9) progressively shifted towards the lower 2-theta angle with increasing Pd loading because of the substitution of a significant amount of Pd^{2+} for M^{n+} (M = Ce^{4+}, Hf^{4+}, Zr^{4+}, Sn^{4+}, or Er^{3+}) in $CeHfZrSnErO_x$ to form $PdCeHfZrSnErO_x$ as a new oxide phase with increased oxygen vacancy concentration and higher surface area relative to pristine $CeHfZrSnErO_x$ (see figure 5.9 (b)).

Scanning TEM was used to observe the microstructure of Pd in $Pd/CeHfZrSnErO_x$. Unfortunately, due to the lack of distinct contrast between Pd and the substrate, the highly dispersed/incorporated Pd species cannot be differentiated from the support. Notwithstanding, the EDS elemental map analysis (figure 5.10) reveals homogeneous distribution Pd, Ce, Hf, Zr, Sn, Er, and O with virtually no agglomeration of Pd species. The HRTEM image in figure 5.10 (a) shows well-defined lattice fringes with measured interplanar spacings of 0.30 nm and 0.26 nm, which correspond to the (111) and (200) planes, respectively of the cubic fluorite structure. Additional lattice fringes with a measured d-spacing of 0.22 nm are equally visible and consistent with the (111) plane of the fcc lattice of Pd in

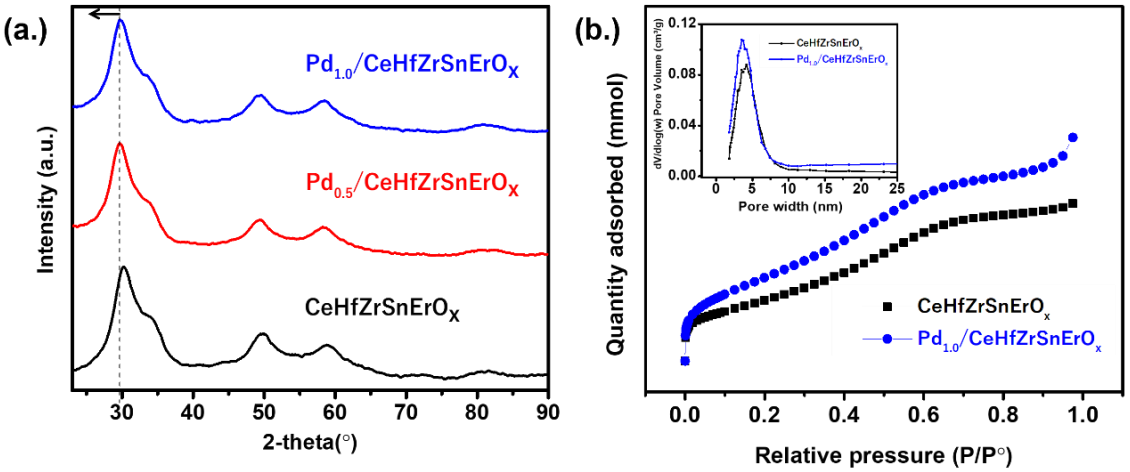

Figure 5.9. (a) XRD patterns of Pd/CeHfZrSnErO$_x$ and CeHfZrSnErO$_x$; the characteristic reflections progressively shifted towards the lower 2-theta angle with increasing Pd loading from 0.5 – 1.0 wt%. (b). N_2 adsorption isotherms of CeHfZrSnErO$_x$ and CeHfZrSnErO$_x$ and the corresponding pore size distribution (inset).

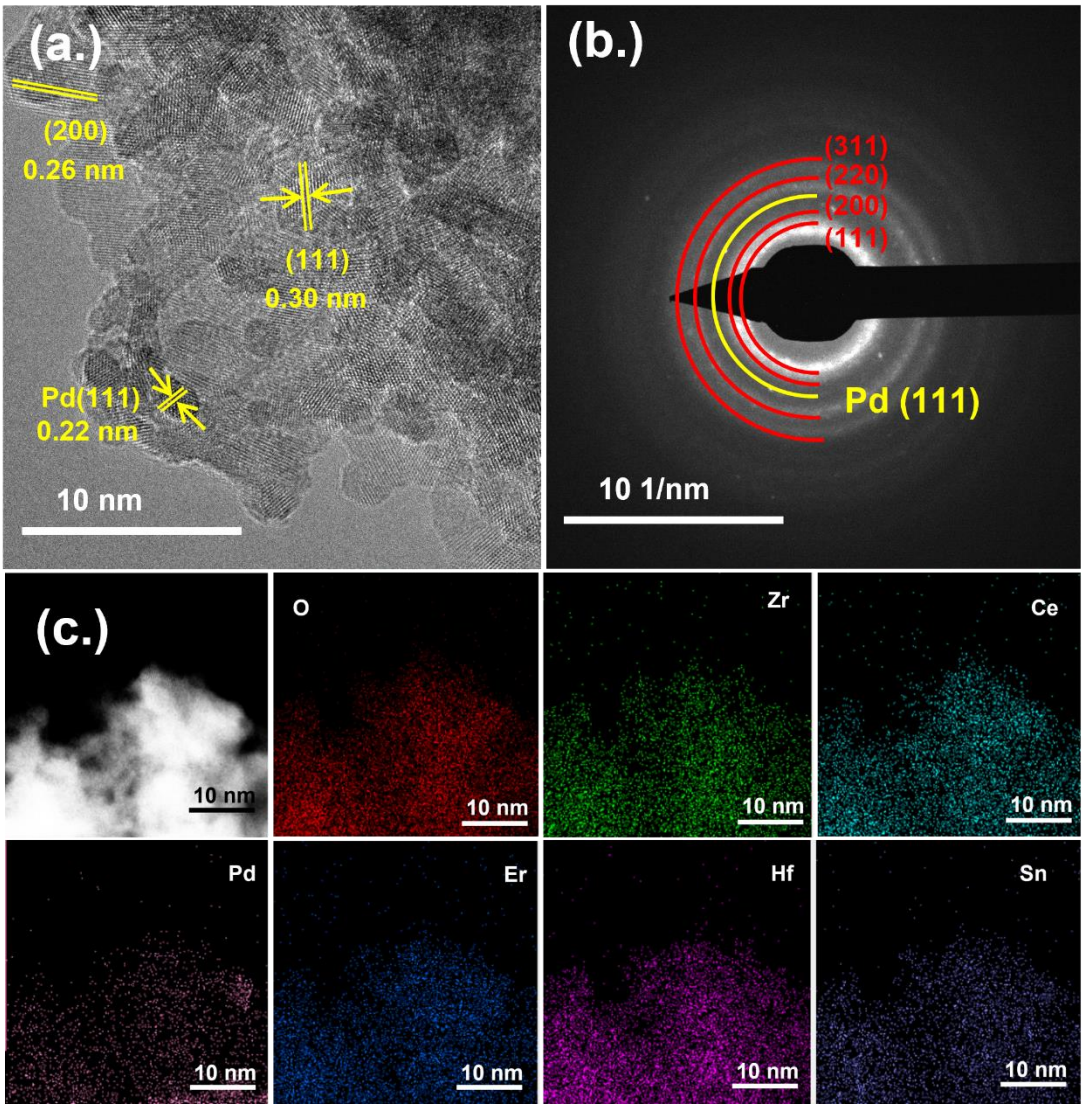

Figure 5.10. Structural characterization of Pd/CeHfZrSnErOx (a) HRTEM image. (b) the corresponding SAED. (c) EDX maps for Pd/CeHfZrSnErO_x showing O, Zr, Ce, Pd, Er, Hf, and Sn elements**.**

accordance with the literature.[39] Notably, these highly dispersed, low concentrated, ultrasmall-sized Pd nanocrystals were not detectable by XRD even after a slow scan of the Pd (111) region ($2\theta \approx 40$). Similarly, the SAED pattern in figure 5.10(b) shows a diffuse ring that can be indexed to (111), (200), (220), and (311) planes of a cubic fluorite structure as well as an additional ring that is ascribed to the Pd (111) planes. This observation is in agreement with the HRTEM results. The relative concentrations of Pd in $Pd_{1.0}$/CeHfZrSnErO$_x$ (1.05%) and $Pd_{0.5}$/CeHfZrSnErO$_x$ (0.49%) was determined by ICP-OES and agree with the theoretical values.

Figure 5.11 (a) displays the Pd 3d XPS spectrum of Pd/CeHfZrSnErO$_x$. The photoemission signals overlapped with the Zr 3p. Four peaks resulting from the pairs of spin-orbit doublets were identified for the Pd 3d XPS spectrum after deconvolution. Judging from the asymmetric peak shape and positions, it appears as though Pd exits as a combination of Pd^0 and Pd^{+2}. The peaks at 339.8 eV and 334.3 eV are attributed to $3d_{3/2}$ and $3d_{5/2}$ spin-orbits of metallic Pd^0 while those at 343.0 eV and 338.1 eV are ascribed to $3d_{3/2}$ and $3d_{5/2}$ spin-orbits of ionic Pd^{2+} in accordance with the literature.[40-44] This submission is collaborated by the Pd CO adsorption behavior in the DRIFTS spectra, displayed in figure 5.11 (b). The electron-deficient Pd^{2+} may have resulted from pairs of electron transfer from Pd to M through Pd-O-M bonds (M = Ce, Hf, Zr, Sn, and Er) in PdCeHfZrSnErO$_x$ solid solution as similarly reported elsewhere in the literature.[19] A more comprehensive analysis of the electronic structure and coordination state can be accomplished via X-ray absorption near-edge structure (XANES) and extended X-ray absorption fine

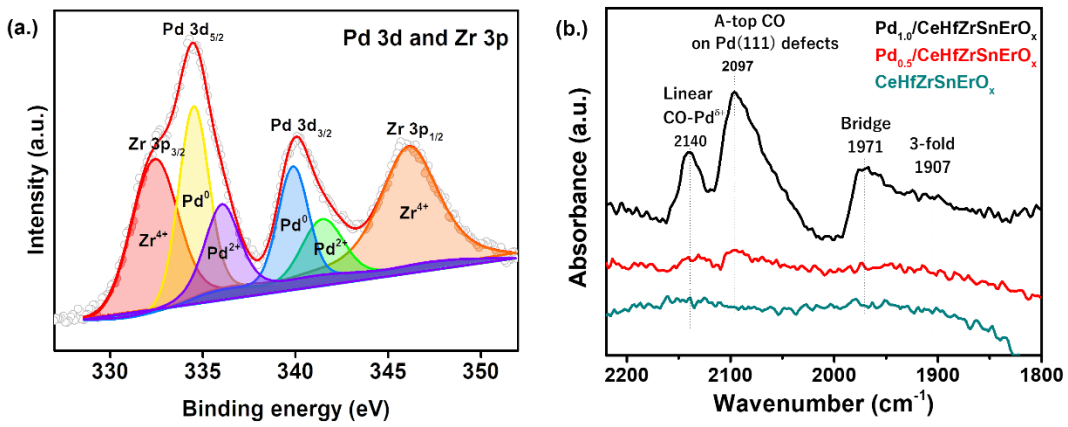

Figure 5.11. Surface chemistry characterization: (a) Pd 3d XPS spectrum of $Pd_{1.0}/CeHfZrSnErO_x$. (b) DRIFTS spectra of $Pd_{1.0}/CeHfZrSnErO_x$, $Pd_{0.5}/CeHfZrSnErO_x$ and $CeHfZrSnErO_x$ upon CO adsorption.

structure (EXAFS) measurement on Pd K-edge but unfortunately cannot be completed at this difficult time of COVID 19 pandemic.

To further understand the chemical structure of palladium, additional information was acquired by the DRIFTS technique upon CO adsorption. The IR spectra are displayed in figure 5.11 (b). To enhance the CO adsorption on the Pd sites, the samples were heated in the DRIFTS cell at 400 °C for 30 minutes under 5% O_2/Ar flow to remove surface-bound organic residues that may have originated from ethylene glycol employed as the reducing agent-cum-solvent-cum-stabilizer in the synthesis process. The DRIFTS spectra of CO collected at 30 °C show the existence of different active sites on the Pd-containing samples. For $Pd_{1.0}$/CeHfZrSnErO$_x$ with 1.0wt.% Pd, the IR bands at ~2097 cm^{-1} and ~2140 cm^{-1} are attributed to CO adsorbed onto A-top sites of Pd (111) atoms and linearly adsorbed CO on electron-deficient $Pd^{\delta+}$, respectively.[45-48] The less intense peak at ~1917 cm^{-1} is attributed to CO adsorbed on the bridge sites. The IR band signal for a 3-fold hollow site is virtually non-existent which indicates the absence of agglomerated Pd particles. The existence of both linear and bridge CO adsorption sites indicates the presence of single-sites and ensemble Pd sites, respectively.[49] That said, it appears that that adsorption site is predominantly single-sites, judging from the relative intensities of both peaks. The IR spectrum of $Pd_{0.5}$/CeHfZrSnErO$_x$ with lower Pd loading displays only IR bands that are assignable to linearly bonded CO on Pd^{2+} and Pd^0 (111) defects, with no evidence of bridge nor hollow-CO bands, indicating that Pd is atomically dispersed on CeHfZrSnErO$_x$ carrier for this sample. On the other hand, the IR spectrum of CeHfZrSnErO$_x$ in the same

wavenumber region, showed no characteristic IR band, suggesting its inability to adsorb CO molecules.

Catalytic CO oxidation is one of the most widely investigated reactions in heterogeneous catalysis because of its usefulness in both fundamental studies and pollution abatement.[50-52] Catalytic CO oxidation, particularly over Pd-based has attracted significant interest in the research community because of its high performance and the relative simplicity of the process.[50-52] Therefore, temperature-dependent CO oxidation was used as a model reaction to assess the activity of different catalytic materials synthesized in the present study. As seen in figure 5.12, the activity of the catalytic materials investigated in the present depends strongly on the Pd content and the support system and decreases in the following order: $Pd_{1.0}/CeHfZrSnErO_x \geq Pd_{0.5}/CeHfZrSnErO_x >> Pd_1/CeO_2 >> CeHfZrSnErO > CeO_x$. Their apparent activation energies were calculated and displayed in figure 5.13. The order of the determined apparent activation energies is consistent with the order of the activity of the five catalysts and is given as follow: CeO_2 (118.5 kJ/mol) > $CeHfZrSnErO_x$ (96.2 kJ/mol) >> Pd_1/CeO_2 (75.8 kJ/mol) ≥ $Pd_{0.5}/CeHfZrSnErO_x$ (29.5 kJ/mol) ≥ $Pd_{1.0}/CeHfZrSnErO_x$ (23.8 kJ/mol). Among the various $CeHfZrSnErO_x$-based catalysts investigated, pristine $CeHfZrSnErO_x$ exhibited the least activity for CO oxidation with a high onset temperature of 110 °C with no complete CO conversion below 300 °C as seen in figure 5.11. The introduction of 0.5 or 1.0 wt % Pd to pristine $CeHfZrSnErO_x$ dramatically improved its catalytic performance. The resultant $Pd_{0.5}/CeHfZrSnErO_x$ and $Pd_{1.0}/CeHfZrSnErO_x$ showed lower onset temperatures of ~50 °C and 70 °C

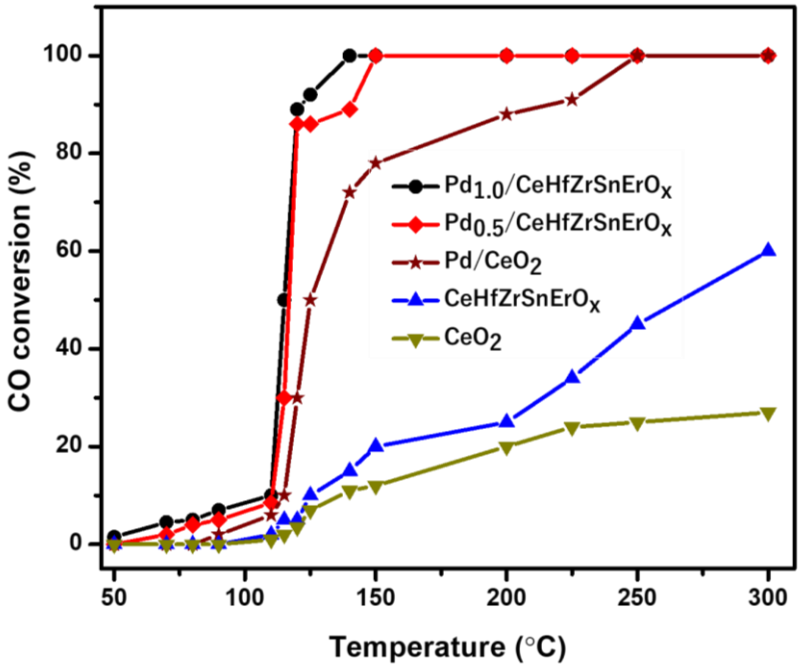

Figure 5.12. Light-off curves of CO conversion over $Pd_{1.0}/CeHfZrSnErO_x$, $Pd_{0.5}/CeHfZrSnErO_x$, Pd/CeO_2, $CeHfZrSnErO_x$ and CeO_2. Reaction condition: 20 mg catalysts loading, 1% CO balanced with dry air at a flow rate of 12.5 mL/min.

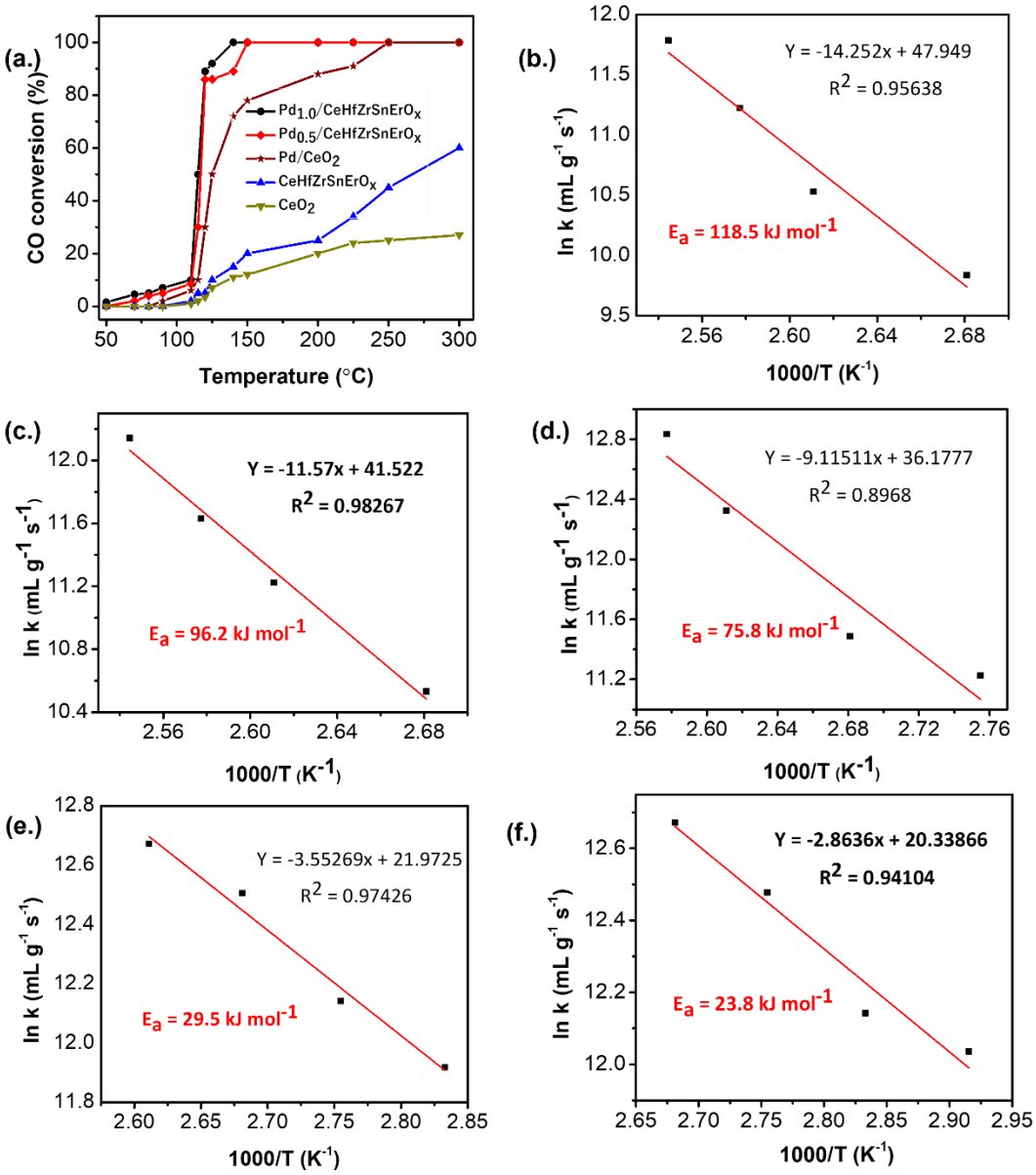

Figure 5.13. (a) Temperature-dependent CO conversion over different catalysts. Arrhenius plots of the variation of ln k with the 1/T over (b) CeO_2 (c) $CeHfZrSnErO_x$ (d) Pd/CeO_2, (e) $Pd_{0.5}/CeHfZrSnErO_x$ and (f) $Pd_{1.0}/CeHfZrSnErO_x$ catalysts.

respectively and a complete CO oxidation at 140 °C and 150 °C respectively, indicating the significant importance of the highly dispersed Pd species within the HEO system. The presence of Pd facilitates the CO and O_2 adsorption on the catalysts' surface, which in turn resulted in higher catalytic activity.[53]

Interestingly, the ceria-supported Pd catalyst - Pd/CeO_2 exhibited inferior performance relative to $Pd_{0.5}/CeHfZrSnErO_x$ and $Pd_{1.0}/CeHfZrSnErO_x$ but superior to pristine $CeHfZrSnErO_x$ under similar conditions. The onset and complete conversion temperatures, over Pd/CeO_2, are 90 °C and 250 °C, respectively. It should be noted that CO oxidation over reducible oxide-supported metal catalysts is generally believed to proceed via the Mars-Van-Krevelen reaction mechanism, where the adsorbed CO on the metals interacts with active lattice O from the reducible support to create oxygen vacancies;[54] hence, the reducibility of the surface lattice O from the support significantly impacts the catalytic CO oxidation.[19] Therefore, it is reasonable to posit that superior catalytic performance of $Pd_{0.5}/CeHfZrSnErO_x$ and $Pd_{1.0}/CeHfZrSnErO_x$ over Pd/CeO_2 is most likely due to enhanced reducibility of the surface lattice oxygen in the vicinity of the Pd in addition to the high oxygen vacancy concentration in the crystal lattice.[19] This submission is consistent with the experimental result reported elsewhere.[19] Also, a strong synergistic effect that goes beyond the simple additive result of combining five catalytically active metals in the cation sublattice may have also contributed to the superior activity. Similarly, the catalytic performance of pristine $CeHfZrSnErO_x$ is superior to that of pure ceria under identical test conditions, additionally

highlighting the inherent advantage of $CeHfZrSnErO_x$ as the carrier support. Furthermore, the stability test of $Pd_{1.0}/CeHfZrSnErO_x$ was studied via a continuous CO oxidation experiment conducted at 140 °C for 24 hours. $Pd_{1.0}/CeHfZrSnErO_x$ showed remarkable stability for CO oxidation, displaying no appreciable loss of activity for 24 hours as seen in figure 5.14 (inset). Additionally, the reusability was tested through consecutive CO oxidation experiments for five cycles. As seen in figure 5.14, $Pd_{1.0}/CeHfZrSnErO_x$ maintains its low-temperature CO oxidation and good reproducibility of results across all five use cycles.

5.9 Conclusion

In summary, we have developed an ultrasound-mediated co-precipitation strategy to fabricate nanostructured high-entropy fluorite oxide ($CeHfZrSnErO_x$) without any external heat treatment. The chemical effect and crystallization process are driven by the transient localized hotspot generated by the physical phenomenon of acoustic cavitation. The as-synthesized $CeHfZrSnErO_x$ carrier, given its high surface area and high oxygen vacancy concentration, was employed as an excellent carrier for the stabilization of highly dispersed and atomically dispersed palladium species. The $CeHfZrSnErO_x$-stabilized Pd catalysts ($Pd/CeHfZrSnErO_x$) outperformed a ceria-stabilized counterpart (Pd/CeO_2) towards catalytic CO oxidation, underscoring the inherent advantage of $CeHfZrSnErO_x$ as reducible carrier support. Such a technologically feasible, scalable, and facile synthetic strategy holds great promise towards the synthesis of HEO systems of other crystal structures and functionalities.

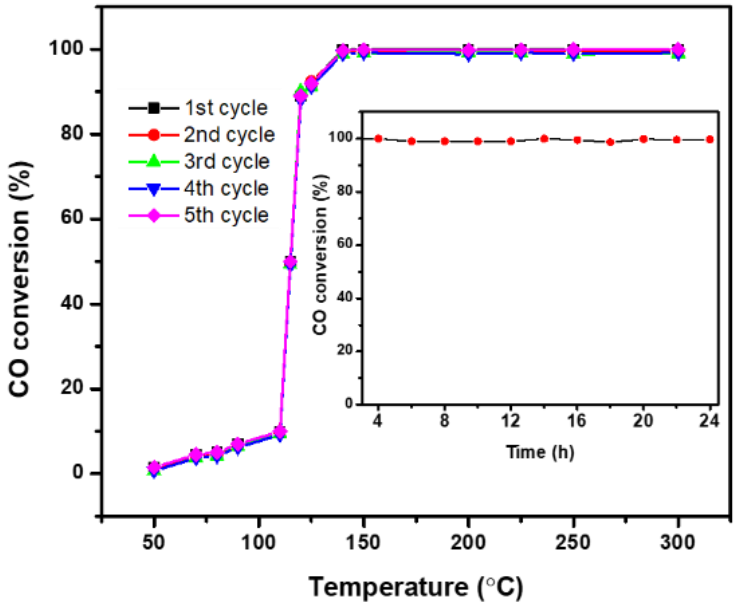

Figure 5.14. Cycled measurement of CO oxidation over $Pd_{1.0}/CeHfZrSnErO_x$ and its stability test result for a continuous CO oxidation experiment conducted at 140 °C for 24 hours (inset).

REFERENCES

[1] Sun, Y.; Dai, S., High-entropy materials for catalysis: A new frontier. *Science Advances* **2021,** *7* (20), eabg1600.

[2] Cantor, B.; Chang, I.; Knight, P.; Vincent, A. J. B., *Microstructural development in equiatomic multicomponent alloys*. 2004; Vol. 375-377, p 213-218.

[3] Yeh, J. W.; Chen, S. K.; Lin, S. J.; Gan, J. Y.; Chin, T. S.; Shun, T. T.; Tsau, C. H.; Chang, S. Y., Nanostructured High-Entropy Alloys with Multiple Principal Elements: Novel Alloy Design Concepts and Outcomes. *Adv. Eng. Mater.* **2004,** *6* (5), 299-303.

[4] Okejiri, F.; Yang, Z.; Chen, H.; Do-Thanh, C.-L.; Wang, T.; Yang, S.; Dai, S., Ultrasound-driven fabrication of high-entropy alloy nanocatalysts promoted by alcoholic ionic liquids. *Nano Research* **2021**.

[5] George, E. P.; Raabe, D.; Ritchie, R. O., High-entropy alloys. *Nature Reviews Materials* **2019,** *4* (8), 515-534.

[6] Liu, M.; Zhang, Z.; Okejiri, F.; Yang, S.; Zhou, S.; Dai, S., Entropy-Maximized Synthesis of Multimetallic Nanoparticle Catalysts via a Ultrasonication-Assisted Wet Chemistry Method under Ambient Conditions. *Advanced Materials Interfaces* **2019,** *6*, 1900015.

[7] Wang, T.; Chen, H.; Yang, Z.; Liang, J.; Dai, S., High-Entropy Perovskite Fluorides: A New Platform for Oxygen Evolution Catalysis. *J. Am. Chem. Soc.* **2020,** *142* (10), 4550-4554.

[8] Tsai, C.-W.; Lai, S.-W.; Cheng, K.-H.; Tsai, M.-H.; Davison, A.; Tsau, C.-

H.; Yeh, J.-W., Strong amorphization of high-entropy AlBCrSiTi nitride film. *Thin Solid Films* **2012,** *520* (7), 2613-2618.

[9] Gild, J.; Zhang, Y.; Harrington, T.; Jiang, S.; Hu, T.; Quinn, M. C.; Mellor, W. M.; Zhou, N.; Vecchio, K.; Luo, J., High-Entropy Metal Diborides: A New Class of High-Entropy Materials and a New Type of Ultrahigh Temperature Ceramics. *Scientific Reports* **2016,** *6*, 37946.

[10] Qin, Y.; Liu, J.-X.; Li, F.; Wei, X.; Wu, H.; Zhang, G.-J., A high entropy silicide by reactive spark plasma sintering. *Journal of Advanced Ceramics* **2019,** *8* (1), 148-152.

[11] Sarker, P.; Harrington, T.; Toher, C.; Oses, C.; Samiee, M.; Maria, J.-P.; Brenner, D. W.; Vecchio, K. S.; Curtarolo, S., High-entropy high-hardness metal carbides discovered by entropy descriptors. *Nature Communications* **2018,** *9* (1).

[12] Rost, C. M.; Sachet, E.; Borman, T.; Moballegh, A.; Dickey, E. C.; Hou, D.; Jones, J. L.; Curtarolo, S.; Maria, J.-P., Entropy-stabilized oxides. *Nature Communications* **2015,** *6*, 8485.

[13] Anandkumar, M.; Bhattacharya, S.; Deshpande, A. S., Low temperature synthesis and characterization of single phase multi-component fluorite oxide nanoparticle sols. *RSC Advances* **2019,** *9* (46), 26825-26830.

[14] Chen, K.; Pei, X.; Tang, L.; Cheng, H.; Li, Z.; Li, C.; Zhang, X.; An, L., A five-component entropy-stabilized fluorite oxide. *J. Eur. Ceram. Soc.* **2018,** *38* (11), 4161-4164.

[15] Gild, J.; Samiee, M.; Braun, J. L.; Harrington, T.; Vega, H.; Hopkins, P. E.; Vecchio, K.; Luo, J., High-entropy fluorite oxides. *J. Eur. Ceram. Soc.* **2018,**

38 (10), 3578-3584.

[16] Okejiri, F.; Zhang, Z.; Liu, J.; Liu, M.; Yang, S.; Dai, S., Room-Temperature Synthesis of High-Entropy Perovskite Oxide Nanoparticle Catalysts through Ultrasonication-Based Method. *ChemSusChem* **2020,** *13* (1), 111-115.

[17] Andrew; Wang, Q.; Hu, C.; Yeh, Y.-T.; Chen, R.; Luo, J., Single-Phase Duodenary High-Entropy Fluorite/Pyrochlore Oxides with an Order-Disorder Transition. *arXiv pre-print server* **2020**.

[18] Nguyen, T. X.; Patra, J.; Chang, J.-K.; Ting, J.-M., High entropy spinel oxide nanoparticles for superior lithiation–delithiation performance. *Journal of Materials Chemistry A* **2020,** *8* (36), 18963-18973.

[19] Xu, H.; Zhang, Z.; Liu, J.; Do-Thanh, C.-L.; Chen, H.; Xu, S.; Lin, Q.; Jiao, Y.; Wang, J.; Wang, Y.; Chen, Y.; Dai, S., Entropy-stabilized single-atom Pd catalysts via high-entropy fluorite oxide supports. *Nature Communications* **2020,** *11* (1).

[20] Sarkar, A.; Djenadic, R.; Usharani, N. J.; Sanghvi, K. P.; Chakravadhanula, V. S. K.; Gandhi, A. S.; Hahn, H.; Bhattacharya, S. S., Nanocrystalline multicomponent entropy stabilised transition metal oxides. *J. Eur. Ceram. Soc.* **2017,** *37* (2), 747-754.

[21] Spiridigliozzi, L.; Ferone, C.; Cioffi, R.; Accardo, G.; Frattini, D.; Dell'Agli, G., Entropy-Stabilized Oxides owning Fluorite Structure obtained by Hydrothermal Treatment. *Materials* **2020,** *13* (3), 558.

[22] Chellali, M. R.; Sarkar, A.; Nandam, S. H.; Bhattacharya, S. S.; Breitung, B.; Hahn, H.; Velasco, L., On the homogeneity of high entropy oxides: An

investigation at the atomic scale. *Scripta Mater.* **2019,** *166*, 58-63.

[23] Suslick, K. S.; Price, G. J., APPLICATIONS OF ULTRASOUND TO MATERIALS CHEMISTRY. *Annu. Rev. Mater. Sci.* **1999,** *29* (1), 295-326.

[24] Djenadic, R.; Sarkar, A.; Clemens, O.; Loho, C.; Botros, M.; Chakravadhanula, V. S. K.; Kübel, C.; Bhattacharya, S. S.; Gandhi, A. S.; Hahn, H., Multicomponent equiatomic rare earth oxides. *Materials Research Letters* **2017,** *5* (2), 102-109.

[25] Shannon, R., Revised Effective Ionic Radii and Systematic Study of Inter Atomic Distances in Halides and Chalcogenides. *Acta Crystallographica Section A* **1976,** *32*, 751-767.

[26] Williamson, G. K.; Hall, W. H., X-ray line broadening from filed aluminium and wolfram. *Acta Metall.* **1953,** *1* (1), 22-31.

[27] Zhang, Z.; Yang, S.; Hu, X.; Xu, H.; Peng, H.; Liu, M.; Thapaliya, B. P.; Jie, K.; Zhao, J.; Liu, J.; Chen, H.; Leng, Y.; Lu, X.; Fu, J.; Zhang, P.; Dai, S., Mechanochemical Nonhydrolytic Sol–Gel-Strategy for the Production of Mesoporous Multimetallic Oxides. *Chem. Mater.* **2019,** *31* (15), 5529-5536.

[28] Zamkovskaya, A.; Maksimova, E.; Nauhatsky, I., Size–strain line-broadening analysis of the calcite-type borates ABO3 (A=Fe, In, Ga). *Journal of Physics: Conference Series* **2018,** *1135*, 012020.

[29] Han, J.; Meeprasert, J.; Maitarad, P.; Nammuangruk, S.; Shi, L.; Zhang, D., Investigation of the Facet-Dependent Catalytic Performance of Fe2O3/CeO2 for the Selective Catalytic Reduction of NO with NH3. *The Journal of Physical Chemistry C* **2016,** *120* (3), 1523-1533.

[30] He, L.; Ren, Y.; Fu, Y.; Yue, B.; Tsang, S.; He, H., Morphology-Dependent Catalytic Activity of Ru/CeO2 in Dry Reforming of Methane. *Molecules* **2019,** *24* (3), 526.

[31] Morgan, K. A.; Huang, R.; Potter, K.; Shaw, C.; Redman-White, W.; De Groot, C. H., Total Dose Hardness of TiN/HfOx/TiN Resistive Random Access Memory. *IEEE Transactions on Nuclear Science* **2014,** *61* (6), 2991-2996.

[32] Yang, H.; Zhang, J.; Li, J.; Shen, Q.; Zhang, L., In Situ Preparation and Corrosion Resistance of a ZrO2 Film on a ZrB2 Ceramic. *Coatings* **2019,** *9* (7), 455.

[33] Huang, C.; Tang, Z.; Zhang, Z., Differences between Zirconium Hydroxide (Zr(OH)4·nH2O) and Hydrous Zirconia (ZrO2·nH2O). *J. Am. Ceram. Soc.* **2001,** *84* (7), 1637-1638.

[34] Su, S. C.; Zhang, H. Y.; Zhao, L. Z.; He, M.; Ling, C. C., Band alignment of n-SnO2/p-GaN hetero-junction studied by x-ray photoelectron spectroscopy. *J. Phys. D: Appl. Phys.* **2014,** *47* (21), 215102.

[35] Xia, W.; Wang, H.; Zeng, X.; Han, J.; Zhu, J.; Zhou, M.; Wu, S., High-efficiency photocatalytic activity of type II SnO/Sn3O4 heterostructures via interfacial charge transfer. *CrystEngComm* **2014,** *16* (30), 6841-6847.

[36] Swami, G. T. K.; Stageberg, F. E.; Goldman, A. M., XPS characterization of erbium sesquioxide and erbium hydroxide. *Journal of Vacuum Science & Technology A* **1984,** *2* (2), 767-770.

[37] Huang, H.; Dai, Q.; Wang, X., Morphology effect of Ru/CeO2 catalysts for the catalytic combustion of chlorobenzene. *Applied Catalysis B: Environmental*

2014, *158-159*, 96-105.

[38] Gunawan, C.; Lord, M. S.; Lovell, E.; Wong, R. J.; Jung, M. S.; Oscar, D.; Mann, R.; Amal, R., Oxygen-Vacancy Engineering of Cerium-Oxide Nanoparticles for Antioxidant Activity. *ACS Omega* **2019,** *4* (5), 9473-9479.

[39] Slavinskaya, E. M.; Kardash, T. Y.; Stonkus, O. A.; Gulyaev, R. V.; Lapin, I. N.; Svetlichnyi, V. A.; Boronin, A. I., Metal–support interaction in Pd/CeO2 model catalysts for CO oxidation: from pulsed laser-ablated nanoparticles to highly active state of the catalyst. *Catalysis Science & Technology* **2016,** *6* (17), 6650-6666.

[40] Mandapaka, R. K.; Madras, G., Microkinetic Modeling of CO Oxidation on Ionic Palladium-Substituted Ceria. *Ind. Eng. Chem. Res.* **2016,** *55* (8), 2309-2318.

[41] Gao, J.; Ren, C.; Huo, X.; Ji, R.; Wen, X.; Guo, J.; Liu, J., Supported Palladium Catalysts: A Facile Preparation Method and Implications to Reductive Catalysis Technology for Water Treatment. *ACS ES&T Engineering* **2021,** *1* (3), 562-570.

[42] Ren, C.; Yang, P.; Gao, J.; Huo, X.; Min, X.; Bi, E. Y.; Liu, Y.; Wang, Y.; Zhu, M.; Liu, J., Catalytic Reduction of Aqueous Chlorate With MoOx Immobilized on Pd/C. *ACS Catal.* **2020,** *10* (15), 8201-8211.

[43] Priolkar, K. R.; Bera, P.; Sarode, P. R.; Hegde, M. S.; Emura, S.; Kumashiro, R.; Lalla, N. P., Formation of Ce1-xPdxO2-δ Solid Solution in Combustion-Synthesized Pd/CeO2 Catalyst: XRD, XPS, and EXAFS Investigation. *Chem. Mater.* **2002,** *14* (5), 2120-2128.

[44] Pillo, T.; Zimmermann, R.; Steiner, P.; Hüfner, S., The electronic structure of PdO found by photoemission (UPS and XPS) and inverse photoemission (BIS).

J. Phys.: Condens. Matter **1997,** *9* (19), 3987-3999.

[45] Tiznado, H.; Fuentes, S.; Zaera, F., Infrared Study of CO Adsorbed on Pd/Al2O3−ZrO2. Effect of Zirconia Added by Impregnation. *Langmuir* **2004,** *20* (24), 10490-10497.

[46] Zaera, F., Infrared and molecular beam studies of chemical reactions on solid surfaces. *Int. Rev. Phys. Chem.* **2002,** *21* (3), 433-471.

[47] Bertarione, S.; Prestipino, C.; Groppo, E.; Scarano, D.; Spoto, G.; Zecchina, A.; Pellegrini, R.; Leofanti, G.; Lamberti, C., Direct IR observation of vibrational properties of carbonyl species formed on Pd nanoparticles supported on amorphous carbon: comparison with Pd/SiO2–Al2O3. *Phys. Chem. Chem. Phys.* **2006,** *8* (31), 3676-3681.

[48] Szanyi, J.; Kuhn, W.; Goodman, D., CO adsorption on Pd(111) and Pd(100): Low and high-pressure correlations. *Journal of Vacuum Science & Technology A: Vacuum, Surfaces, and Films* **1993,** *11*, 1969-1974.

[49] Zeinalipour-Yazdi, C. D.; Willock, D. J.; Thomas, L.; Wilson, K.; Lee, A. F., CO adsorption over Pd nanoparticles: A general framework for IR simulations on nanoparticles. *Surf. Sci.* **2016,** *646*, 210-220.

[50] Chen, H.; Fu, J.; Zhang, P.; Peng, H.; Abney, C. W.; Jie, K.; Liu, X.; Chi, M.; Dai, S., Entropy-stabilized metal oxide solid solutions as CO oxidation catalysts with high-temperature stability. *Journal of Materials Chemistry A* **2018,** *6* (24), 11129-11133.

[51] Chen, H.; Jie, K.; Jafta, C. J.; Yang, Z.; Yao, S.; Liu, M.; Zhang, Z.; Liu, J.; Chi, M.; Fu, J.; Dai, S., An ultrastable heterostructured oxide catalyst based

on high-entropy materials: A new strategy toward catalyst stabilization via synergistic interfacial interaction. *Applied Catalysis B: Environmental* **2020,** *276*, 119155.

[52] Zhou, Y.; Wang, Z.; Liu, C., Perspective on CO oxidation over Pd-based catalysts. *Catalysis Science & Technology* **2015,** *5* (1), 69-81.

[53] Kunkalekar, R. K.; Salker, A. V., Activity of Pd doped and supported Mn2O3 nanomaterials for CO oxidation. *Reaction Kinetics, Mechanisms and Catalysis* **2012,** *106* (2), 395-405.

[54] Peterson, E. J.; Delariva, A. T.; Lin, S.; Johnson, R. S.; Guo, H.; Miller, J. T.; Hun Kwak, J.; Peden, C. H. F.; Kiefer, B.; Allard, L. F.; Ribeiro, F. H.; Datye, A. K., Low-temperature carbon monoxide oxidation catalysed by regenerable atomically dispersed palladium on alumina. *Nature Communications* **2014,** *5* (1), 4885.

CHAPTER 6: CONCLUSION AND FUTURE WORK

6.1 Conclusions

The preparation of nanostructured multicomponent heterogeneous catalysts constitutes a major synthetic challenge in catalysis science. This dissertation described unconventional synthetic methodologies driven by the physical process of acoustic cavitation for the realization of nanostructured HEMs for different catalytic investigations. Taking advantage of the acoustic cavitation phenomenon, nanostructured particles of various subclasses of HEMs, including high-entropy perovskite oxides (HEPO), high-entropy alloys (HEAs), and high-entropy fluorite oxide (HEFO) were fabricated at seemingly room temperature conditions without any external heat-treatment process.

The synthesis of the HEPO was realized via an ultrasound-mediated coprecipitation strategy at seemingly room temperature conditions. The HEPOs were obtained as monodispersed, spherically-shaped nanoparticles. The average crystallite size was determined to be approximately 5.9 nm. A variety of spectroscopic and microscopic techniques were utilized to characterize the crystalline nature, chemical composition, surface chemistry, and textural features To the best of our knowledge, this is the first study that successfully prepared perovskites-structured high-entropy oxide nanocrystals without external heat treatment. The EDS elemental map results showed excellent dispersion of the representative elements. Notably, the entropically-driven stability of

Ru/BaSrBi(ZrHfTiFe)O_3 with excellent dispersion of Ru in the perovskite phase bestowed the nanoparticles with good catalytic activity for CO oxidation.

The synthesis of the HEA nanocatalysts was realized via an ultrasound-driven wet chemistry method promoted by alcoholic ionic liquids (AILs). Because of the intrinsic reducing ability of the hydroxyl group, AIL was fabricated as the multifunctional reaction media capable of reducing metal species under ultrasound irradiation while simultaneously stabilizing the as-afforded nanocrystals. Under high-intensity ultrasound irradiation, $Au^{3+,}$ $Pd^{2+,}$ $Pt^{2+,}$ Rh^{3+}, and Ru^{3+} ions were co-reduced by the AIL and transformed into single-phase HEA (AuPdPtRhRu) nanocrystals, effectively eliminating the need for any external heat-treatment process. The hydroxyl functionality played a significant role in the formation of single-phase nanocrystals in one synthetic step. Characterization results confirmed that as-obtained nanocrystals are composed of elements of Au, Pd, Pt, Rh, and Ru as expected. This quinary AuPdPtRhRu nanocatalyst outperformed the binary, ternary, and quaternary counterparts towards selective hydrogenation of phenol to cyclohexanone. The synthetic strategy provides an improved and facile methodology for the sustainable synthesis of multicomponent alloys in one step under mild conditions.

As is with HEPOs, the synthesis of the nanostructured HEFOs ($CeHfZrSnErO_x$) was equally accomplished by an ultrasound-assisted coprecipitation strategy at ambient conditions. Unlike the HEPO synthesis where the choice of the metal composition was based on the tolerance factor, a set of selection guidelines were used for the choice of the metal components that favor

the formation of single-phase crystals in HEFO. The crystalline structure, chemical composition, surface chemistry, and textural properties of the synthesized CeHfZrSnErO were studied by various characterization techniques. Characterization results reveal ultrasmall nanocrystals with high surface area and high-oxygen vacancy concentration which makes $CeHfZrSnErO_x$ an excellent carrier for stabilization of active metal catalyst. After introducing palladium to $CeHfZrSnErO_x$, the resultant $Pd/CeHfZrSnErO_x$ shows high dispersion of Pd nanoclusters and atomically dispersed palladium species. The catalytic activity of $Pd/CeHfZrSnErO_x$ was compared to Pd/CeO_2 of similar Pd loading towards CO oxidation and $Pd/CeHfZrSnErO_x$ exhibited superior performance which underscored the inherent advantage of $CeHfZrSnErO_x$ carrier support.

6.2 Future work

While the synthetic protocols demonstrated for this work were optimized for the synthesis of HEAs, HEFOs, and HEPOs, ultrasound-mediated synthesis is not limited to only these three subclasses of HEMs. Thus, it would be pertinent to investigate the synthesis of HEMs with different crystal structures and functional features including high-entropy carbides, high-entropy nitrides, high-entropy silicides, high-entropy borides, etc., before generalizing this synthetic method.

In addition, the catalytic investigation can as well be expanded beyond CO oxidation and/or selective phenol hydrogenation to include other catalytic processes such as photocatalytic and electrocatalytic reactions.

6.3 Probing the origin of the catalytic performances

In chapter five, we posited that the superior catalytic performance of Pd/CeHfZrSnErO_x over Pd/CeO_2 towards CO oxidation is likely due to the better reducibility of surface lattice oxygen in the vicinity of the Pd. To confirm this submission, assessment of the reducibility of Pd/CeHfZrSnErO_x and Pd/CeO_2 is recommended through, gas chemisorption experiment, specifically CO temperature-programmed reduction (CO-TPR). Gas chemisorption is a widely used strategy to determine the active sites of heterogeneous catalysts via exposure to probe molecules like CO, NH_3, or CO_2, where they bind to the surface of the atoms, contrary to physisorption where the probe molecules interact weakly on the surface of the catalysts via dispersive forces. Conducting a CO-TRP experiment can be used to determine the number of reduced Pd sites which can come very handy in the determination of the turn-over frequency (TOF), an important parameter that can be used to compare/assess the catalytic efficiency of the materials. Also, a more comprehensive analysis of the Pd microenvironment – electronic structure and coordination state – is recommended via X-ray absorption near-edge structure (XANES) and extended X-ray absorption fine structure (EXAFS) techniques on Pd K-edge to collaborate the XPS and DRIFTS analysis results that ambiguously revealed the valence states of 0 and +2 for Pd.

VITA

Francis Okejiri was born in Abia State, Nigeria in 1990 and graduated from Assumption Model Secondary Technical School, Uturu in 2007 after passing his West African Senior School Certificate Examination. He began attendance at Nnamdi Azikiwe University in 2007 and after four years graduated with a Bachelor of Science degree in Pure and Industrial Chemistry.

After working a few years in the industry, Francis returned to academia to pursue a Master's degree in Analytical Chemistry from Middle Tennessee State University under the supervision of Dr. Ngee Sing-Chong and graduate in the summer of 2017.

In fall 2017, he joined the chemistry department at the University of Tennessee at Knoxville and soon after began his doctoral research under the advisement of Dr. Sheng Dai. He completed his dissertation in November 2021, focused on the ultrasound-mediated synthesis and characterization of high-entropy materials for heterogeneous catalysis.